Optically stimulated luminescence dating using quartz

Andrew Murray, Lee Arnold, Jan-Pieter Buylaert, Guillaume Guérin, Jintang Qin, Ashok Singhvi, Rachel Smedley, Kristina Thomsen

Optically Stimulated Luminescence Dating

Andrew Murray[1†], Lee J. Arnold[2], Jan-Pieter Buylaert[3], Guillaume Guérin[4,5], Jintang Qin[6,7], Ashok K. Singhvi[8], Rachel Smedley[9], Kristina J. Thomsen[10]

[1]Department of Geoscience, Aarhus University, Høegh-Guldbergs Gade 2, DK-8000 Aarhus C, Denmark

[2]School of Physical Sciences, Environment Institute, Institute for Photonics and Advanced Sensing (IPAS), University of Adelaide, North Terrace Campus, Adelaide, SA 5005, Australia

[3]Department of Physics, Technical University of Denmark, DTU Risø Campus, DK-4000, Roskilde, Denmark

[4]IRAMAT-CRP2A, UMR 5060 CNRS - Université Bordeaux Montaigne, Maison de l'archéologie, Esplanade des Antilles, 33607 Pessac cedex, France, and Univ Rennes, CNRS, Géosciences Rennes, UMR 6118, 35000 Rennes, France

[5]Univ Rennes, CNRS, Géosciences Rennes, UMR 6118, 35000 Rennes, France

[6]State Key Laboratory of Earthquake Dynamics, Institute of Geology, China Earthquake Administration, Beijing 100029, China

[7]Xinjiang Pamir Intracontinental Subduction National Field Observation and Research Station, Beijing 100029, China

[8]AMOPH Division, Physical Research Laboratory, Navarangpura, Ahmedabad 380009, India

[9]Department of Geography and Planning, University of Liverpool, L69 7ZT, UK

[10]Department of Physics, Technical University of Denmark, DTU Risø Campus, DK-4000, Roskilde, Denmark

[†]Corresponding email: anmu@dtu.dk

Author contributions

Introduction (A.M., L.J.A., J-P.B., G.G., J.Q., A.K.S., R.S., K.T.); Experimentation (A.M., L.J.A., J-P.B., G.G., J.Q., A.K.S., R.S., K.T.); Results (A.M., L.J.A., J-P.B., G.G., J.Q., A.K.S., R.S., K.T.); Applications (A.M., L.J.A., J-P.B., G.G., J.Q., A.K.S., R.S., K.T.); Reproducibility & data deposition (A.M., L.J.A., J-P.B., G.G., J.Q., A.K.S., R.S., K.T.);

Limitations and optimisations (A.M., L.J.A., J-P.B., G.G., J.Q., A.K.S., R.S., K.T.); Outlook (A.M., L.J.A., J-P.B., G.G., J.Q., A.K.S., R.S., K.T.); A.M. overlooked the Primer.

Acknowledgements

The authors thank three unknown referees for their useful suggestions, which certainly improved the manuscript. Stacey-Lynn Pavia steered us through the writing and editing process, and we are very grateful for her support and guidance. AKS acknowledges the Science and Engineering Research Board (DST), India, for a YoS Chair Professorship. Jan-Pieter Buylaert received funding from the European Research Council (ERC) under the European Union's Horizon 2020 research and innovation programme (ERC-2014-StG 639904 – RELOS). Guillaume Guérin received funding from the European Research Council (ERC) under the European Union's Horizon 2020 research and innovation programme (ERC Grant agreement No. 851793 – QuinaWorld). Jintang Qin is funded by National Natural Science Foundation of China (NSFC41671008).

Competing Interests

K.T. and J-P. B. declare a competing interest. They are both employees of the Technical University of Denmark, a commercial producer of luminescence dating instrumentation. The remaining authors declare no competing interest

Abstract

Optically Stimulated Luminescence (OSL) signals from quartz can be used to determine the timing of deposition of sedimentary archives. OSL dating uses the accumulation of energy stored in a crystal structure to measure time. This stored energy is absorbed from ionising radiation, and is released (reset) by heat or daylight. The total energy (dose) absorbed since last resetting is measured using OSL, and divided by the rate of storage (dose rate) to give the time elapsed from the last heating or daylight exposure. In this Primer, we introduce the quartz OSL method and outline the signal resetting processes. We describe the origins and quantification of the dose rate and describe the daylight-sensitive OSL signal most appropriate to dose estimation. The most widely used dose measurement method is then introduced, together with quality-control procedures. A broad set of geological and archaeological studies are used to illustrate the wide range of potential applications, and we describe the challenges arising from different deposition environments and summarize evidence for the precision and accuracy of published ages. Uncertainties and minimum reporting are discussed together with methodological limitations, particularly when applied to young and old sediments. Finally, we highlight the anticipated future developments in the field.

[H1] Introduction

The surface of our planet preserves extensive sediment archives recording the history of our species and its environment, but interpreting these archives depends on knowing when the sediments were deposited. Luminescence dating is one of the main methods used to estimate the depositional age of sediments over the last ~0.5 million years. This Primer is targeted at users of luminescence ages who seek greater understanding of how ages are derived and how to interpret their reliability, and at students and academics intending to implement the method in their work.

There are many methods for determining the deposition age of sediments and associated deposits[1], but radiocarbon, cosmogenic radionuclide and luminescence dating are the most widely applicable to the recent geological past. Other methods, such as U-series and Ar-Ar, are site and sample specific and can only occasionally be employed. Radiocarbon dating was developed first, and it still dominates studies in the Neolithic and more recent archaeology. In other time periods (especially beyond ~45 ka) and in many geological applications, luminescence dating has proved to be the most useful. This method dates the last time quartz (and feldspar) was heated or exposed to daylight. It can be applied to nearly all sediments on the Earth's surface, and used to date material over a wide age range, from almost the last decade to ~500 ka ago.

Luminescence is light resulting from the release of energy stored in a crystal structure. This signal can be used for dating because the amount of stored energy increases with continuing exposure to natural ionising radiation (and therefore increases with time), and because luminescence can be reset by heat or daylight. As a result of its known sensitivity to heat, luminescence was first applied to the dating of pottery and other ceramics, but its full potential only became apparent when it was realised that the signal was also reset by daylight exposure[2]. Initial studies employed thermoluminescence (TL), but optically stimulated luminescence (OSL) rapidly took over following the first measurements on quartz in 1985[3]. OSL can be more readily reset by daylight exposure; TL bleaches much more slowly, and is never completely reset. Daylight exposure of sediment grains is ubiquitous during sediment erosion, transport and deposition, and so OSL has the potential to date almost any surficial deposit. This direct dating of the deposition of mineral grains also removes any ambiguity of association, such as occurs with the radiocarbon dating of sediments using organic matter.

In nature, luminescence from quartz (and feldspar**)** arises from the dose absorbed from ionising radiation through time. This radiation is emitted (**Fig. 1a**) primarily during the radioactive decay of ^{40}K, and the ^{238}U and ^{232}Th decay series; it creates free electrons in the quartz crystal lattice, some of which are then trapped for long periods in defects in the lattice structure (**Fig. 1b**). Stimulation with light or heat (**Fig. 1c**) releases these trapped electrons, some of which give up their stored energy as photons; this is luminescence **Fig. 2** illustrates how this luminescence depends on prior bleaching (here, natural

exposure to daylight), and on the dose rate . After sample collection and preparation, the dose rate is derived from analyses of radionuclide concentrations, and the dose from OSL. In the laboratory, the natural luminescence signal is first measured by illuminating a sub-sample with light (**Fig. 2a**), and this signal is calibrated in terms of dose. The age in years is then calculated from:

$$Age\ [a] = \frac{Dose\ [Gy]}{Dose\ rate\ [Gy.a^{-1}]} \qquad .....(1)$$

This Primer focuses on OSL dating of sand-sized (63-300 µm) quartz grains, using blue (~470 nm) or green (~530 nm) light stimulation and signal detection in the UV band (~340 nm). This choice is based on the relative simplicity of this technique, the signal stability and the ubiquity of the mineral. Other luminescence dating approaches use silt-sized quartz[4, 5], silt- and sand-sized feldspar[6], and/or OSL signals stimulated with violet[7], or infra-red[8] light. We outline the principles and the experimental procedures most commonly used in deriving a quartz luminescence age, summarise methodological challenges, and indicate how these are overcome in practice. We then discuss reproducibility and accuracy, limitations, and finally our expectations for future developments.

[H1] Experimentation

Before a luminescence age is measured, various practical steps must be undertaken. First, the sample must be collected without exposure to daylight – for example, from a wind-blown or fluvial sediment, a deep-sea marine core, an archaeological pottery sherd or an anthropogenic cave deposit. In the laboratory, the quartz grains are separated for measurement in darkroom conditions, because the signal is sensitive to light. Any illumination used must be of a wavelength and intensity that minimises the effect on the potential luminescence signal[9]. The measurement equipment includes a stimulation light source, a source of ionising radiation, a heating system and a photon detector to count the photons emitted by the luminescence process. All of these experimental issues are discussed below.

[H2] Sampling

The quartz-containing material - usually sediment - must be collected while avoiding daylight exposure because OSL dates the last exposure of sand grains to daylight. In the field, the surface of the sediment, or of the sedimentary sequence of interest, is first cleaned by scraping back[10], which helps avoid the light-exposed first few mm/cm of material. This also provides a clear view of the stratigraphy, so that locations can be avoided that may have been affected by post-depositional disturbances, such as ice wedges, animal burrows, roots, etc. At least the first few cm must be removed; if possible, it is better to cut a section back by >1 m to avoid air-exposed material. This makes it more likely that the oxidation/reduction conditions and moisture content of the sample are representative of the long-term burial. These operations can be undertaken in full daylight, allowing photographs to be taken of the

sampling site and of samples before removal, thus providing a record of sampling locations and their relationship to the general stratigraphy.

There are then two approaches to collecting a sediment sample from a cleaned terrestrial deposit. The easiest is to hammer tubes (3-5 cm diameter of metal or plastic, depending on the degree of consolidation of the deposit) into the section. This method is only suitable when the unit to be sampled is of sufficient thickness that the tube will not cross sedimentological boundaries**.** If possible, the tube should be at least 15 cm from any boundary, so that the γ dose rate gradient across the tube is small. A crushed paper/plastic plug can be placed in the tube to support the sediment during insertion, reducing the risk of collapse and the mixing of exposed and unexposed material. The tube must be filled completely, either with sample or by packing with plastic, to ensure that the material cannot move and mix during transport. In the laboratory, the outer ~2-3 cm of each end of the tube that have potentially been light-exposed are set aside for radionuclide concentration measurements (to estimate the dose rate) and for other sedimentological analyses (for example grain size, mineralogy, geochemistry, ancient DNA, tephrochronology, etc.). The inner part of the tube is used for OSL measurements to estimate the dose (see equation 1), and possibly for water content measurements (Box 1).

If the unit is too thin to be sampled with a tube, the second approach is to operate in the dark – either under an opaque covering such as a tarpaulin or at night (moonlight has very low intensity and will not significantly affect the OSL during the short sampling exposure[11]). In both cases, a controlled light source, such as a red LED or a headlamp emitting dim orange light, can be used. It is usual to collect two parts for each sample: one for OSL analysis, used to estimate the dose, and the other for radiochemical analysis - to calculate the dose rate. First, the previously cleaned surface is scraped back again (~1 cm) as it is likely to have been exposed to daylight after the initial cleaning of the section; the sediment removed during cleaning can be retained for radioelement concentrations measurements and for any other complementary measurements. The second part of the sample, taken from further into the section, must be protected from light exposure. Although a few hundred grams is usually sufficient for later processing, the actual sample size depends on the concentration and the size distribution of quartz grains. For instance, a carbonate-rich sandstone generally contains a smaller proportion of quartz grains than a desert dune sand, and a marine/lake core usually yields fewer sand-sized grains... If a narrow-grain-size fraction is to be targeted for single-grain OSL measurements, the amount of sediment required may be greater than usual to ensure sufficient grains of the desired grain-size range are recovered. This is in contrast to multi-grain aliquots, which can use a different and broader size range, chosen to suit the sample.

Marine and lacustrine deposits are often sampled by coring. Although it is desirable to use opaque core barrels, this is not always possible, and successful sampling has been undertaken on poorly-archived light-exposed core material[12]. Whenever possible, cores should be split under controlled lighting. However, undessicated material can often be successfully sampled, even if the core was initially

processed in full daylight, by scrapping off a few mm of the light-exposed surficial material (this should be retained for the dose rate measurement)[13, 14]. It is important to recognise that the depth range that can be treated as a single sample varies with core depth. For a given sedimentation rate, the depth interval representing a period of time that is small compared to the age uncertainty increases with core depth. For instance, consider an age uncertainty of 10%, and a sedimentation rate of 10 mm/ka. For sediment that is 10 ka old (100 mm depth), 10 mm of sample depth is equivalent to the age uncertainty of 10%. But at 100 ka (1000 mm), 10 mm of sample only represents 1% of the age; to achieve the same age sampling resolution as at 10ka, a 100 ka old sample can be 100mm thick. This is important because sample size is often a limiting factor in working with core material. For the same reason, vertical mixing of the outer layer of the core by the core-barrel may be important in shallow material, but can often be ignored in deeper, older material without impacting the age uncertainty.

If the target is ceramic material such as pottery, bricks, and tiles, or heated or unheated stones and cobbles, all sampling can be undertaken in daylight, although direct sunlight should be avoided. This is because, in the case of ceramics and heated stones, the potentially light-exposed surface of the sample is discarded in the laboratory, while in the case of cobbles, light is attenuated so rapidly with depth that a few minutes of daylight does not affect the average luminescence signal in the outer 1 mm[15]. Nevertheless, some rocks (e.g quartzite) are more translucent than others, and more sensitive to light exposure during sampling; it may be prudent to take extra care with such samples.

The presence of water reduces the dose rate and increases the calculated age. It is therefore important to estimate the average water content of the deposit over the burial period. During sampling one should consider the water content history of the site and collect samples on which to measure the present day water content. A subsample of the OSL sample from inside the tube or from the radioelement sample (see above) can be used for this, and for determining the saturated water contents. In order to measure a reliable present-day water content, sealable bags should be used and the ends of the tubes made airtight by sealing with plastic.

Finally, sampling is the occasion to collect information to measure or estimate the long-term average overburden of a sample. This includes the nature of the overburden, such as a cave roof, sediment, etc., and the density and the thickness of the material covering the sample. The elevation of the site above sea level and geographical coordinates (latitude, longitude) should also be recorded. These field observations are used collectively to calculate the cosmic ray dose rate[16], which typically contributes ~10% to the total for shallow (<3 m) burial).. Furthermore, in cases where the sediment is heterogeneous on a scale of 10-50 cm, for example because of the presence of rocks, sediment unconformity, boundary between sediment and air or sediment and bedrock, etc., it may be necessary to measure in situ γ dose rates (see below). It is also often appropriate to collect two or more separate dose rate samples, one from sediment to be dated and one from the adjacent rock/sediment causing heterogeneity, in order to

measure the radionuclide concentrations in both components and model the γ dose rate (see Appendix H in[17]).

[H2] Sample preparation

In the laboratory, the part of the sample intended for dose rate measurements is homogenised by grinding, so that even the small samples required for radiochemical analyses (typically a few 100 mg) are representative of the whole. Supplementary Table 1 lists typical methods for dose rate determination, and the typical sample size required. Given the usually considerable resource investment in sample collection, it is good practice to keep back a portion of the non-light-exposed material as a substitute in case something goes wrong (mis-labelling, light exposure etc.) during sample preparation. The remaining part of the sample intended for OSL measurements undergoes several treatment steps to extract quartz grains (see **Fig. 3a**). The unexposed inner part of ceramics and heated stones is gently crushed and either it or the sediment is wet sieved to obtain a specific grain-size range. Grain size is important not only because of measurement practicalities, but also because both laboratory and environmental dose rates are, to some degree, grain-size dependent[17]. The selection of a grain-size range is driven by the abundance of that size range in the samples, and the practicality of chemically etching the outer surface of the grains to remove the α-irradiated component. Typically, grains must not be smaller than fine sand (> 63 µm) or there is a risk that chemical etching completely dissolves the sample Generally, some choice is made within the range of 63-300 µm (for example 90-125 µm, 150-180 µm or 180-250 µm); the 180-250 µm fraction is the most suitable for measurements using single-grain discs with 300 µm diameter holes.

In all the steps outlined below, the sample should remain at or close to room temperature to avoid the risk of thermal loss of the OSL signal, especially during the HF digestions steps. HF is a particularly dangerous substance that can be lethal if used incorrectly. Because of this, the operator should carefully familiarise themselves with all local safety procedures and regulations before using HF.

The selected size fraction is first treated with 10% HCl (aqueous, as are all solutions below) for at least 30 minutes, or until gas evolution ceases completely. This removes carbonates, which may impede the reaction with HF. The sample is then treated with 30% H_2O_2 for up to a few days to remove finely disseminated organics. To more easily disaggregate grains in fine-grained, clayey-silty sediment or carbonate-rich sandstones, the bulk sediment can be soaked in water and treated with HCl and H_2O_2 before wet-sieving. After treating with HCl and H_2O_2 and sieving, a few gram(s) of sample should be left - mainly a mixture of quartz, feldspar and sometimes heavy-mineral grains, all in the chosen grain-size range. If only quartz is desired, the sample may then be placed directly in concentrated HF (40%). Usually ~1 hour is sufficient to remove feldspar and etch the surface of the quartz grains (see below). If the feldspar grains are also required, then prior mineral separation is necessary, usually via density separation. K-feldspars, for example, are commonly used in other approaches to luminescence dating[6,

[18]. To improve recovery when density separating quartz from feldspar, surface coatings and attached clay grains can be removed using dilute HF (10%**)**. The density separation step normally uses an aqueous heavy liquid such as lithium heteropolytungstate. This is much safer to use than the more traditional organic liquids, and it is also much more convenient, because it can be readily diluted/evaporated to any density between 1 and ~3 $g.cm^{-3}$. A density of 2.70 $g.cm^{-3}$ allows any heavy minerals to sink; 2.62 $g.cm^{-3}$ allows a quartz-rich fraction to sink; 2.58 $g.cm^{-3}$ allows a Na-rich feldspar fraction to sink and leaves a K-rich feldspar fraction floating. Some laboratories use only a single 2.58 $g.cm^{-3}$ step and rely on the later HF step to remove any denser feldspars that remain in the quartz-rich fraction. Any heavy minerals that persist after the HF treatment rarely, if ever, make a significant contribution to the quartz luminescence signal. Magnetic separation is also used to separate quartz and feldspar grains, instead of density separation[19].

Finally, treating the quartz extract with concentrated HF (40%) for 1 hour removes any remaining feldspar. This treatment also etches ~10 µm from the outer surface of the quartz grains, thus removing most of the quartz layer exposed to α particles from the surrounding sedimentary matrix during burial (see **Fig. 1**). The internal α activity of quartz is very small and this etching step significantly simplifies the dosimetry calculations. Some laboratories then soak the sample in 10% HCl for several hours to remove any fluorides that might have precipitated on the grain surfaces. Although there is no evidence that such amorphous precipitates are a significant source of contamination in quartz OSL, some fluoride residues can be of sufficient thickness to significantly attenuate the OSL signal. After a final wash, it may then be desirable to re-sieve the samples to define the minimum grain size during β-irradiation and, for single grain measurements, to minimise the risk of multiple grains in each hole in the sample holder. For the measurement of multi-grain aliquots, a few mg of quartz may be placed loose in cups, or adhered as a monolayer to stainless steel discs using silicone oil. The quartz is then tested for signal purity using infrared stimulation (see Box 3). If it fails this test, the HF etching stage can be repeated, although the extra mass loss has a small additional effect on the average natural β dose to the grains.

[H2] Dose rate fundamentals

The dose rate term in equation 1 is derived from the flux of ionising radiation originating with both natural radioactivity and cosmic rays. For sand-sized quartz grains, the dose rate is dominated by ^{40}K, which emits β particles and γ rays[20], and members of the ^{238}U and ^{232}Th decay series (α,β,γ[17]; Supplementary Figures 2 and 3). The abundance of these radionuclides in sediments depends on the source rock and on differential transport processes related to weathering, erosion, transport and deposition. Some of these processes are physical, such as sorting by size and/or density, while others separate nuclides as a result of their geochemical properties[21]. The dose rate contribution from cosmic rays is usually small, and depends on latitude, altitude and burial depth[16] (Supplementary Figure 1).

Direct measurement of the dose rate is complex, particularly because the various radiations penetrate matter differently; in sediments, α particles travel distances of up to ~20 μm, β particles up to ~3 mm and γ rays up to ~50 cm (**Fig. 1a**). Fortunately, in many cases the key dosimetric concept of an infinite matrix can be used to circumvent this difficulty[17, 22]; in an infinite matrix all the energy emitted in the medium must also be absorbed in the medium, provided that the medium is homogeneous over dimensions significantly larger than the distance travelled by the relevant radiation. Thus, one only needs to know the energy emission rate to know the dose rate. The infinite matrix has different dimensions depending on the radiation: for γ rays it is a body of sediment >0.75 m in diameter, and for β particles it is only about 5 mm in diameter.

The rate of energy emission in an infinite matrix is calculated from the concentrations of all the relevant radionuclides. The activity per unit mass [$Bq.kg^{-1}$] of a certain nuclide can be estimated directly, by for example alpha counting or γ spectrometry (see Supplementary Table 1), but very often only the mass concentrations of K and the series parents U and Th are measured using, for example, inductively coupled plasma mass spectrometry. In order to deduce the activity concentrations of other radionuclides in the U and Th decay series, the condition known as secular equilibrium is often assumed. In some cases this assumption is invalid, because members of the decay series have been separated by their differential geochemistries[21, 23], and a more detailed knowledge of the state of equilibrium is required. The latter may or may not be time-dependent, depending on whether the system is open or closed to radionuclide migration.

The lifetime-averaged water content of the sediment is also important (see Box 1). Water absorbs energy but since it does not usually contain significant radioactivity, it does not emit energy. The net effect is to reduce the dose rate.

[H3] In situ γ dose rate measurements

In cases where sediment is heterogeneous on the scale of the penetration distance of γ rays (~30-50 cm, see Figure 1a) the infinite matrix γ dose rate may not be representative of the γ dose rate to which the sample was exposed during burial. These cases include poorly sorted sediment, sediment including pebble and cobbles, or sediment adjacent to a rock wall. As an alternative, the γ dose rate may be measured in situ at the sample location using, for instance, luminescent aluminium oxide (Al_2O_3:C) pellets. Aluminium oxide is very similar to quartz in terms of dose absorption characteristics, and doping with carbon gives this material a very sensitive luminescence response to dose[24]. In practice, pellets are left buried in an aluminium tube for 6-12 months, after which the absorbed dose is sufficient to induce a measurable OSL signal[25,26]. The aluminium tube has a ~2-3 mm wall thickness to prevent beta particles from reaching the pellets. This directly-measured dose rate is the sum of γ and cosmic dose rates, as affected by escape of ^{222}Rn and the water content of the sediment over the period of measurement. Escape of the noble gas ^{222}Rn can be important because the decay of this radionuclide

gives rise to about 60% of the beat dose rate from the ^{238}U series, and 98% of the gamma dose rate (see Table S2b). In contrast to dose rates derived from radionuclide concentrations, correcting in situ dose rates for past variations in ^{222}Rn escape or water content requires some independent knowledge of the effect on the calibration of the dosimeter of such variations, and this information is not usually available.

The other common way of determining in situ γ dose rates involves the use of a field γ spectrometer, typically with a NaI(Tl) or LaBr probe. Calibration involves measurements in infinite media of known radionuclide concentrations[27]. Data analysis may consist of estimating effective K, U and Th concentrations using the 'windows technique' (see Appendix L in[17]), and then converting these concentrations into effective infinite matrix dose rates. The concentration of K is based on the emission rate of the γ ray peak at 1461 keV, of U on the 1764 keV peak and of Th on the 2615 keV[28]. Alternatively, the proportionality between total γ dose rate and the count rate above a certain energy is used in the 'threshold' technique[29,30]. The advantage of this approach lies in the inclusion of a greater portion of the recorded spectrum to estimate the γ dose rate, thereby reducing the uncertainties for a given counting time (typically several minutes), but this approach does not give any nuclide-specific information. It is also difficult to correct such threshold data for past variations in ^{222}Rn escape or water content without independent knowledge of the U, Th and K contributions to the total.

[H2] Measuring the Equivalent dose (D_e)

The instrumentation for determining the dose absorbed during burial and its equivalent in terms of producing luminescence includes a luminescence detector, a stimulation light source, a source of ionising radiation and a heating system. **Fig. 3b** summarises the relationship of these four components with respect to the quartz grains to be measured.

The main challenge in designing such a system is instrument sensitivity. The precise measurement of an absorbed dose depends both on the sensitivity of the sample - equivalent to the number of photons emitted per unit mass and per unit absorbed dose [$kg^{-1}.Gy^{-1}$], and on the detection efficiency - the fraction of the emitted photons that are actually detected by the instrument. The relationship of the resulting signal to the instrument background noise must also be considered. Detection efficiency depends on the light path, the quantum efficiency **of** the photon detector, and the wavelength and intensity of the stimulation light source. The latter are important because the more rapidly the charge is released or detrapped (Figure 1c), the stronger the initial luminescence signal compared to background noise. For a given detection wavelength, the electron detrapping rate depends on the wavelength-dependent photoionization cross-section[31] and the power density of the stimulation light at the sample.

The luminescence detector consists of a photon detector and detection filter(s). To precisely measure weak luminescence signals, a highly sensitive light detector with a low background count rate, such as a photomultiplier, and good light collection are essential. The latter requires that the solid angle

subtended by the detector surface at the sample be as large as possible – this is usually achieved by minimising the distance between sample and detector or by focussing through lenses. In OSL, the luminescence signal is emitted as a consequence of optical stimulation, which is ~10^{15} times more intense than the OSL signal itself[32]. Thus appropriate detection filters are necessary, both to separate the luminescence from the stimulation light and to define the spectral detection window.

[H3] Photon detector

Quartz has a relatively broad OSL emission peaking at ~360 nm, with a full width half maximum (FWHM) of ~80 nm (see Supplementary Figure 6). Photomultiplier tubes (PMT) operating in photon counting mode and sensitive in the blue/UV range are most commonly used for detecting quartz OSL, because of their high sensitivity, large dynamic range and low dark count rate. A large signal-to-noise ratio is particularly important when measuring insensitive samples and/or samples having absorbed small radiation doses, such as young samples. The quantum efficiency of the PMT is typically up to ~30 % depending on the wavelength of the luminescence. However, PMTs do not provide information on the spatial variation of the emitted luminescence. In applications where such spatial information is of importance, such as rock surface luminescence dating, electron-multiplier charge-coupled devices (EMCCD) can be used but they are generally less sensitive than PMTs (see examples in[33-35]).

[H3] Detection filters

The use of detection filters is important to define the wavelength window of interest and to separate the emitted luminescence from scattered stimulation light. In quartz OSL dating, the emission is usually detected through a filter with a peak transmission at 340 nm and a FWHM of 80 nm (Supplementary Figure 7)**.** The main emission from quartz is centred on 365 nm and, in principle, a significant improvement in light detection is available by choosing a longer wavelength detection filter closer to the main emission of quartz. However, moving the detection window closer to the typical stimulation wavelength of 470 nm also gives an increase in background signal resulting from breakthrough of the stimulation light, and hence does not necessarily improve the signal-to-noise ratio[36].

[H3] Stimulation light source

The electron detrapping rate depends both on the intensity and the wavelength of the optical stimulation light[37, 38] (see Supplementary Figure 8); the more intense and shorter the wavelength, the stronger the OSL signal per unit time. For most applications, optical stimulation is at a constant light intensity (continuous wave mode), but modulating the intensity of the stimulation light, for example in linear modulated OSL[39], can be used to visually separate the signals from the different traps involved in OSL production. In pulsed OSL [POSL], pulsing the stimulation light and only detecting in between short

~50 µs bursts of stimulation light can help to separate quartz and feldspar OSL signals instrumentally[40]. POSL is also used to gain insight into luminescence recombination processes[41].

Optical stimulation of quartz can be achieved using any visible light source such as filtered halogen lamp systems[36] , lasers[34, 42, 43], light emitting diodes (LEDs)[32] and laser diodes[34, 44]. In most quartz multi-grain OSL dating applications, blue (450-470 nm) or green (~525 nm) LEDs are used, with power densities at the sample position ranging between ~40 and 100 mW/cm^2. These result in the decay of the fast OSL component within a few seconds (see below). As LEDs have a broad emission at FWHM ~30 nm, it is often necessary to stimulate the luminescence through cut-off filters to ensure an effective separation of stimulation light and detection windows[45] (see Supplementary Figure 7). Shorter wavelength light sources such as 405 nm laser diodes[7] can be used to access deeper traps insensitive to blue light. In single-grain applications, stimulation by a green 532 nm solid state laser providing a power density of ~50 W/cm^2 is common[46].

[H3] Source of ionising radiation

The measured natural OSL signal must be calibrated in terms of absorbed dose. As different sub-samples/aliquots of quartz can have very different luminescence sensitivities, it is necessary to calibrate aliquots individually. This calibration is performed by comparing the natural OSL signal with that arising from a known laboratory dose given to each aliquot (see below and Figure 4). For convenience, a β source containing the artificial radionuclide ^{90}Sr with a half-life of 28.8 years and its short-lived progeny ^{90}Y is usually used to deliver the laboratory dose{Aitken, 1985 #359}{Andersen, 2003 #434}. This combination of emitters has a maximum β energy of 2.27 MeV and a mean energy of ~600 keV, which makes it relatively easy to shield sufficiently for it to be safe to use.

The laboratory dose rate to a quartz sample depends on the activity of the source, the source/sample distance, sample grain size, and the substrate material on which the grains sit. Because of this, the source must be calibrated for each irradiation geometry, particularly for different substrates and grain-size ranges. The calibration is usually based on a portion of quartz grains that has been given a known dose using a calibrated γ source. An appropriate measurement protocol is used to determine the duration of β irradiation that provides a sensitivity-normalised luminescence intensity equal to that induced by the reference γ dose[47] (see below). Some laboratories provide sensitive quartz that has already absorbed a well-known γ dose[47], which allows those without access to a calibrated γ source to calibrate their own β source as required.

[H3] Heating system

Finally, to obtain an accurate D_e, it is important to perform reproducible thermal pre-treatments and to control the temperature of the aliquot during optical stimulation. OSL dating systems usually heat up to 700 °C, controlled by user-defined linear heating rates typically ranging between 0.01 and 10 °C/s. This heating capacity allows for flexibility in application, particularly when measuring TL. In routine quartz

OSL measurements, temperatures above 280 °C are rarely used and heating rates in the range of 2 to 5 °C/s are typical.

[H3] Instrument reproducibility

Very little has been published on formally testing the stability and reproducibility of the various components of an OSL measurement system, but there has been some examination of the overall reproducibility of the measurement of an OSL signal. After allowing for systematic changes in sensitivity in one automated system, repeated cycles of dosing, preheating and OSL measurement using multi-grain aliquots gave a standard deviation of ~1% in the resulting OSL signals [48].

[H1] Results

[H2] Deriving the dose rate

Radionuclide concentrations vary considerably from one location to another[49] (Supplementary Figure 4 a-e) because of changes in grain size and mineralogy, with the result that sample-specific dose rates are required. Because well-sorted sands tend to be lower in radioactivity than clays or silts, the effective age range of the technique can often be extended by targeting sandy sediments - the lower the dose rate, the greater the dating range. Radionuclide concentrations within quartz grains are very low[50], and the dose rate to such grains is usually derived almost entirely from their surrounding environment. Sand-sized quartz grains (usually 63 - 300 μm) are etched in concentrated HF during sample preparation to remove the outer 10-20 μm layer[17, 19], which reduces the external alpha dose rate contribution to negligible proportions. The effective total dose rate to well-sorted sands is typically ~1-2 $Gy.ka^{-1}$ (Supplementary Table 3), although this value can vary considerably[49]. In dry sediment, typically ~60% of the dose rate is from β particles and ~30% is from γ rays; the remaining ~5-10% contribution is from cosmic radiation. The contribution from ^{40}K alone may be ~40-50% of the total (Supplementary Figure 3), although this is variable (Supplementary Figure 4e,f) because of the considerable range of relative activity concentrations in natural sediments.

Depending on how the concentrations of radionuclides have been derived, they may be expressed as activity concentration A [$Bq \cdot kg^{-1}$] or mass concentration C_0 [$g \cdot kg^{-1}$]. The first step in deriving the infinite matrix dose rate is to convert mass concentrations into activity concentrations. Then the atom concentration per unit mass of sediment N [kg^{-1}] for a particular nuclide is calculated using

$$N = (C_0/m_a) \cdot N_A \qquad (2)$$

where m_a is the atomic mass (for our purposes with units [$g \cdot mol^{-1}$]) and N_A is Avogadro's number [mol^{-1}]. Then the activity concentration is given by

$$A = N \cdot \lambda \qquad (3)$$

where λ is the relevant decay constant [s^{-1}]. Measured concentrations may be reported by external analysts in ppm [$\mu g \cdot g^{-1}$] for U and Th, and percentage [%, 10 $mg \cdot g^{-1}$] for K; these must first be converted to [$g \cdot kg^{-1}$]. In the case of K, the mass concentration of ^{40}K is then derived using the isotopic abundance (0.0117%) before using equations (2) and (3).

Finally, for each nuclide and type of emission (α,β,γ), the infinite matrix dose rate is given by the product $A \cdot \overline{E}$, where $\overline{E}$ is the average energy emitted per disintegration usually given in MeV (1 MeV=1.6×10^{-13} J , see The National Nuclear Data Center). Once the infinite dose rate for each nuclide and each radiation type has been derived, they are summed over all radionuclides to give the infinite matrix dose rates for each type of radiation, as in the example given in Supplementary Table 3. Relevant conversion factors ($Gy \cdot ka^{-1}$)/($Bq \cdot kg^{-1}$) are summarised in Supplementary Table 2, and are regularly compiled and updated[51].

The example spreadsheet (Supplementary Data) attached to this primer allows the reader to work through the calculation of dose rates using the infinite matrix assumption starting from concentrations of K, U and Th. Such calculations provide estimates of the total amount of energy emitted (and thus absorbed) in the sediment per unit time, regardless of the heterogeneity in the radionuclide concentrations, and thus in the radiation field around each grain. They thus give the arithmetic average dose rate to the grains of interest. Such heterogeneity in dose rate is to be expected in almost all sandy deposits (ref Mayya et al., 2006, RM, Guérin et al., 2015, QG). In these circumstances it can be shown mathematically that an accurate age can only be obtained by using the average absorbed dose in equation 1 (ref Guérin et al., 2017, QG). This problem of the most appropriate dose estimation model to use in the age equation is considered further below.

When dose rates vary in time and/or space, the infinite matrix assumption is not met[52]. A heterogeneous medium results in a heterogeneous radiation field and thus leads to different doses absorbed by different quartz grains. Small-scale heterogeneity on the μm-mm scale affects radiation travelling only short distances, such as α and β particles. For example, K-rich feldspar grains in a quartz-dominated sand provide localized high concentrations of ^{40}K and different β dose rates to different quartz grains (Supplementary Figure 5b[53, 54]). Larger scale heterogeneity on the cm scale also affects γ dose rates; if limestone blocks, low in ^{40}K, ^{238}U and ^{232}Th, are embedded in a higher activity sediment, the γ dose rates to sand grains within a few tens of cm of the blocks will be lower than those to grains distant from the blocks (see Supplementary Figure 5a). The radiation field may also vary with time, for example as radioactive material is liberated and exported by reducing groundwater or the hydrolysis of feldspar, or as non-radioactive material is imported into the deposit with infiltrating rainwater or groundwater, leading to, for instance, the precipitation of carbonates or silicates[55].

[H2] Deriving the equivalent dose D_e

Estimation of the dose absorbed during burial (termed the natural-, burial- or palaeo-dose) lies at the heart of any luminescence age, and reliable dose estimation depends on the OSL signal used. The luminescence signal from quartz is complex, but with some exceptions[56] there is evidence that the part of the signal known as the fast-component derives from a single type of trap, which appears to empty according to first-order kinetics, if held at an appropriate temperature[57]. As a result, this fast component is largely independent of the other components[58], and because it follows first-order kinetics, the fast-component consistently shows a sample- and dose-independent exponential decay shape with stimulation time (Fig.4c inset)[58, 59]. Importantly, only the luminescence characteristics of the fast-component (particularly stability and light sensitivity) are sufficiently well-known to be used in a reliable estimation of natural dose. The fast-component signal is stable (over ~10^8 years)[60] and is also most readily reset by daylight, making it most likely to be sufficiently reset in nature. It can also reset by heating[60]. Heating prior to burial increases the sensitivity of the fast-component to dose[59, 61-63], allowing the measurement of much smaller doses. In particular, ceramics only a few years/decades old can often be dated, and this can also apply to naturally heated sediments such as a lava flow. Although the fast-component OSL signal increases with laboratory dose often up to many hundreds of Gy, natural doses tend to be underestimated above ~150-250 Gy. This effective dose limit is often well below the largest dose that can be measured under laboratory conditions, and the reason for this discrepancy is not well understood[64-66]. When considered together with the value of the dose rate, it is this upper limit to the usable dose that defines the maximum age of the method. This maximum is typically ~150 ka, although ages of >1 Ma have been reported in unusually low dose rate environments[67-69]. In unusually high dose rate environments, the upper age limit will be correspondingly lower. The simplest way to confirm the presence of the fast-component is to compare the initial rate of signal loss during stimulation with that of a standard sample known to be fast-component dominated (**Fig. 4c** inset using quartz from[47]) or to use the ratio of the initial intensity during stimulation to the intensity remaining later in the stimulation period[70, 71].

Experimentally, it is important to ensure that the fast-component dominates the numerical estimates of OSL used in dose calculations to avoid contributions from slower components with different bleaching and thermal stability characteristics, and to avoid possible contamination by feldspar OSL. Such signal separation can be achieved by component fitting[37, 72] using a sum of exponential decay terms. In addition, separation can also be improved by stimulating with green light instead of blue because the difference between optical cross-sections for release of charge from the fast and slower components is greater for longer wavelengths[73]. Nevertheless, slower components can also be represented by independent decaying exponential curves, and there is an order of magnitude difference in decay rate between the fast and slower components when stimulating with blue light[59]. For most multi-grain applications where the stimulation power is the same from aliquot to aliquot, this difference in decay

rates allows the use of simple summation, called early background subtraction[74, 75], to discriminate against the slower components. In early background subtraction, a signal proportional to the intensity of the fast-component is calculated by subtracting the luminescence observed in the period after the beginning of stimulation from the initial luminescence observed at the beginning of the stimulation period. The signal difference is effectively zero in the absence of any fast-component, because the medium and slower components do not decay significantly in the time between the two summation periods.

Natural quartz has very heterogeneous luminescence and only a few % of grains give a significant fast-component signal[76]. Thus there are considerable advantages in measuring aliquots containing hundreds to thousands of grains. This approach is only recommended if it is unlikely that useful information is contained in the distribution of doses recorded by different grains, such as that resulting from incomplete resetting or post depositional mixing (this reservation does not apply to dose rate heterogeneity[77]). Luminescence is averaged over many grains when working with such multi-grain aliquots, and the Central Limits theorem suggests that these average OSL signals will be normally distributed.

[H3] Dose estimation using the Single Aliquot Regenerative (SAR) dose procedure

In regeneration methods, the dose absorbed by an aliquot of quartz grains is estimated by first measuring the natural luminescence resulting from the natural dose. Luminescence signals are then regenerated in the same aliquot by various known laboratory doses given after laboratory resetting. These regenerated signals are then used to construct a curve of luminescence response to dose. Finally, the natural luminescence signal is interpolated onto the laboratory dose response to obtain an estimate of the natural dose. However, sensitivity changes from measurement to measurement have been observed for any regeneration of the signal in the laboratory , rendering interpolation inaccurate. Although such changes can arise from several sources, all are expressed as changes in the sample response to dose.

The Single Aliquot Regenerative (SAR) dose procedure [78] (see **Box 2** and **Fig. 4**) successfully overcomes this problem by using the luminescence response to a fixed test dose to correct for sensitivity changes. SAR is now the most widely used dose estimation method in retrospective dosimetry including dating. It is particularly useful because all the measurements needed for a single dose estimate are made on one aliquot, which can be as small as an individual grain. SAR is thus one of only two procedures that have been used to determine distributions of dose in quartz grains within a sample (the other procedure being the Single Aliquot Added Dose – SAAD – [79]). This sensitivity-change correction, and the assumptions implicit in its use, are discussed using the simple model given in **Box 2**. The most important outcome of this model is that the sensitivity-corrected luminescence signal is independent of the measurement cycle, which is confirmed experimentally (**Fig. 5a**, data obtained using the measurement sequence of **Fig. 5b**)[78].

The model in **Box 2** suggests that the luminescence response is unlikely to follow simple exponential saturation. Nevertheless, it is common practice for interpolation to fit the response of L_i/T_i to dose with an expression of the form:

$$\frac{L_i}{T_i} = \frac{L_S}{T_S}.(1 - e^{-\frac{D}{D_C}}) \ldots\ldots (6)$$

where the constant $\frac{L_S}{T_S}$ is the sensitivity-corrected light level at saturation, and the constant D_c is commonly described as the characteristic saturation dose. $D_c$may be referred to as D_0 in the literature, but here we reserve this for the natural dose in a SAR sequence (see **Box 2**). D_c is only truly constant (and equal to 1/b in b) if $\chi(D)$ in **Box 2** is constant, which is unusual. Fortunately, interpolation of the natural signal onto a curve built from the regenerated signals ensures that the resulting dose is almost independent of models of luminescence response to dose, in marked contrast to a result obtained by extrapolation.

The signals resulting from the use of the typical SAR measurement sequence (**Fig. 5b**) with a single multi-grain aliquot of quartz extracted from a heated brick are shown in **Fig. 4a-c**, and with quartz from an unheated sediment in Figure 4d-f. The values for L_i and T_i were derived by summing the signals observed in the first 0.32 s (~25 mJ) of stimulation and subtracting the next 0.32 s as background. These measurements are discussed below.

In the first SAR cycle (i=0), D_0 was absorbed during burial and the natural signal is measured. This natural OSL signal (L_0) from the brick quartz is shown as a dashed horizontal line in **Fig. 4b**, together with the following test dose response (T_0) in **Fig. 4a** (solid blue symbol plotted at 0 Gy). At the end of the cycle, the aliquot is bleached to ensure it does not contain any residual signal (step 7 in **Fig. 5b**), before returning to Step 1 for the second cycle (i=1, D_1=0.5 Gy); and the second cycle signals (L_1 and T_1) are then measured. Repeating the measurement cycle continues with values of D_i increasing by 0.5 Gy steps until D_{11}=10.5 Gy. In the following cycle, D_{12} = 0 Gy to give L_{12} (downwards open triangle in **Fig. 4b**) and T_{12} in **Fig. 4a**. The 2.5 Gy point is then repeated (L_{13} - open square in **Fig. 4b**, T_{13}), and finally a repeat measurement (L_{14} – also open square – and T_{14}) of the response to a 10.5 Gy regenerative dose. **Fig. 4c** shows the resulting sensitivity-corrected dose response curve obtained by dividing each value of L_i by the corresponding T_i. The intercept of the natural signal, L_0/T_0, on the smooth curve passing through the regenerated L_i/T_i data is 3.8 Gy. Without the sensitivity correction, an incorrect value of 1.8Gy would have been obtained (**Fig. 4b**).

The same process was repeated for the sedimentary quartz aliquot (**Fig. 4d-f**), but with different values of D_i, and additional repeated dose points. In this case, the corrected dose estimate is 25 Gy in contrast to a value of 14 Gy without sensitivity correction.

It is important to note that the SAR procedure determines the laboratory β dose (as delivered by a relatively simple unscattered β spectrum) that produces the same luminescence response as the natural dose (delivered by complex heavily-scattered α, β, γ and cosmic ray spectra). This matching laboratory dose may not be identical to the natural dose and is therefore termed the equivalent dose D_e owing to the different luminescence efficiencies of different radiations, especially alpha, cosmic rays and low energy scattered electrons and photons [17, 77, 80].

[H3] Testing the applicability of a SAR protocol

SAR is an empirical procedure supported by modelling[81]. Reliability can never be assumed a priori and, as far as possible, its applicability should be tested on each sample. In routine application, measurements of the recycling ratio and recuperation are usually built into any individual SAR dose measurement.

A recycling ratio is derived from a repeated measurement of at least one dose point (see open symbols in Figure 4, $D \neq 0$ Gy), to test the accuracy of the sensitivity correction. The recycling ratio is the ratio of the second regenerated value of L/T to the first (L_2/T_2:L_1/T_1) and should be close to unity.

Recuperation is measured by determining L/T for D = 0 Gy (see open symbols in Figure 4 for regeneration dose of 0 Gy)**.** This measurement determines the carry-over of any residual signal from the previous measurement cycle, and it should be small compared to (L_n/T_n). In some samples, recuperation may be significant (>5%), and a further optional step added[82] to the original SAR procedure (step 7 in Figure 5b) can reduce it. In very young samples, seemingly significant recuperation (>>5%) is often ignored without apparently compromising the accuracy of the ages[83].

Measuring the recycling ratio and recuperation tests the reproducibility of the sensitivity-corrected luminescence response to doses given in the laboratory. In addition, evaluating the importance of thermal pretreatment, thermal transfer and test dose size, and the dose recovery ratio all contribute to the evaluation of the applicability of a SAR protocol.

Thermal pretreatment or preheating before luminescence measurement is required[84] for accurate estimation of the D_e. The thermal dependence of D_e arises largely because of changes in the probability of luminescent recombination[85], and because of the presence of less-light-sensitive, thermally-shallow unstable traps, which give TL peaks at 110, 180 and 220°C. Charges released from these traps may be recaptured by the deeper fast-component trap and identified with a thermoluminescence peak at 325 °C[57, 86]. Alternatively, charge released during stimulation from the fast-component trap may be retained by these shallow traps in a process known as optical transfer. Optical transfer processes are of different significance in measurement following burial compared to measurement after laboratory dosing. For instance, the shallow trap at 110 °C is unstable at environmental temperatures and so remains essentially empty during burial, whereas deeper traps will retain some charge. In contrast, all traps fill during

irradiation on a laboratory timescale. Both optical transfer processes affect the intensity of the fast-component signal; after irradiation in the laboratory, the shallow trap at 110 °C must be emptied by preheating or else the intensity of the regenerated fast-component signals will be affected and result in a significant error in D_e[87]. To this end, preheating is mandatory (step 2 in **Box 2**) because it helps isolate the fast-component by emptying other less-light-sensitive traps that deplete more slowly but contribute to the OSL signal. Preheating also speeds up the transfer of charge after laboratory irradiation, simulating the effect of storage time: it both empties shallow traps and transfers some charge to the fast-component trap, as similarly happens during burial. Optical transfer from the 110 °C trap is also why stimulation is usually carried out at a temperature sufficient to prevent the accumulation of charge in the 110 °C trap. In practice, this stimulation temperature is usually 125 °C[57].

However, thermal pretreatment also has undesirable effects: the S and/or χ (see Equation 4 in **Box 2**) appropriate to the natural dose may respond differently to preheating compared with the S and/or χ appropriate to a laboratory dose. In a process known as thermal transfer, preheating may also induce a fast-component signal in an otherwise well-bleached modern sample through charge transfer from light-insensitive shallow traps into a previously empty OSL trap. One way of testing for the significance of all the above-mentioned effects is to look for a plateau in D_e estimates following preheating to various temperatures. This analysis enables determining the range over which the estimated dose is independent of preheat temperature (**Fig. 6a**). The sample should also be preheated immediately before measurement of T_i because the test-dose response can help track the sensitivity of the fast-component. This second preheat step (Step 5, 'cut heat' in **Fig. 5b**) must be above 130 °C to empty the 110 °C trap, and is usually at least 20 °C below the regeneration preheat temperature in practice.

Thermal transfer of charge to the fast-component trap from low-temperature light-insensitive traps can make a well-bleached sample, with negligible charge in the fast-component trap at the time of burial, appear to be incompletely bleached. These low-temperature traps are sufficiently stable in nature to retain a significant trapped charge population, and because they are light-insensitive they are therefore difficult to empty before burial. As a result, they act as charge reservoirs. Thermal transfer can move sufficient charge from these reservoirs into the fast-component trap to result in an overestimation of D_e. In general, this phenomenon is unlikely to be of significance in older samples, but in young samples, where there is only a small amount of trapped charge in the OSL trap from the most recent burial period, it can be of considerable importance. The potential significance can best be examined by bleaching a set of aliquots in the laboratory either by artificial or daylight stimulation, followed by a preheat plateau test as described above. The apparent dose at low preheat temperatures such as 160°C should be negligible (**Fig. 6b**). However, the apparent dose increases as the preheat temperature is increased and charge is increasingly transferred to the OSL trap. The choice of maximum acceptable preheat temperature is then made by comparison with the D_e[88, 89].

Any dependence of D_e on test dose size can be similarly examined to find a test dose range over which the D_e is constant. The OSL from a small test dose can be affected by thermal transfer, especially if the preceding regeneration dose was large, and too large a test dose may lead to dose underestimation[78]. In general, it seems that a test dose of ~30% of the natural dose is a good compromise. However, a value equal to or larger than the D_e may be necessary for young or insensitive samples to ensure a measurable test dose signal.

Although all the tests described above are important to a greater or lesser degree, the dose recovery ratio[90] provides the single most complete test of SAR performance for any given sample. It can be used to assess whether a specific SAR protocol can accurately determine a known dose administered when the sample is in a condition as close as possible to that when it was initially reset before burial. To achieve this, any natural trapped charge population in an aliquot is first removed by artificial or daylight exposure without any thermal treatment before the aliquot is given a known laboratory dose. While the given laboratory dose is typically similar to the D_e, young samples may necessitate a larger dose for the precision required. The given dose is then measured using the chosen SAR protocol. The dose recovery ratio is the ratio of the measured dose to the given dose and should have a value close to unity (**Fig. 6c,d**). The given dose must be administered before any pretreatment (especially before any preheating) other than light exposureto distinguish the dose recovery ratio from the recycling ratio.

Although usually reported as a dose recovery ratio, it is important to realise that the measured quantity is sensitivity-corrected luminescence (L/T), not dose. At low doses, in the more linear part of the dose response curve, dose behaves similarly to sensitivity-corrected OSL (**Fig. 7**, black OSL distribution at 20% of saturation). In contrast, at high doses where the response curve becomes significantly sub-linear, even small uncertainties in *L/T* are magnified by interpolation and dose uncertainties can become unbounded. For a normal OSL distribution with a relative standard deviation (RSD) of 5% centred on 86% of saturation ($2xD_c$, **Fig. 7**, blue data), almost all signals can be interpolated onto the growth curve. However, the resulting dose distribution is significantly asymmetrical and the RSD is ~20% of the mean dose or 4 times the measurement uncertainty on L/T. In contrast, for an OSL signal with 5% RSD centred on 95% of saturation ($3xD_c$), ~15% of aliquots cannot be interpolated onto the dose response curve and the RSD of the apparent dose distribution is ~30% of the mean (**Fig. 7**, green data).

Alternatively in a dose recovery measurement, if the regenerative dose D_1 is chosen equal to the given dose D_0 then the recovery ratio is more usefully expressed as the luminescence ratio $(L_0/T_0)/(L_1/T_1)$. This OSL ratio is a more sensitive measure for the reliability of a chosen protocol because the dispersions in the OSL distributions will always be ≤ those in the dose distributions. The OSL ratio also avoids the incorrect rejection of values when measuring close to saturation. In true saturation, the average luminescence ratio should be unity, with 50% of observations (for a normal distribution) lying above unity[91] (**Fig. 7**, red data). However, luminescence ratios above unity cannot be interpolated to

give doses, and so must be ignored if a dose ratio is reported. This incorrectly biases dose estimates to low values (**Fig. 7**), and produces an inaccurate dose distribution with pronounced asymmetry and a standard deviation of ~30%. As a result, any dose recovery measurement close to saturation is biased and accompanied by a risk of incorrectly accepting/rejecting a sample as suitable for dating.

The dose recovery ratio or luminescence recovery ratio is an average sample descriptor, which cannot be applied to the individual aliquots used for dose measurement. The reason for this is that the given dose must be administered before any preheating, but samples must be preheated before measurement of the natural signal. The dose recovery ratio describes the suitability of the chosen SAR protocol to measure a known laboratory dose given to a particular sample prior to any thermal treatment, but it does not establish whether the chosen SAR protocol will measure a dose equivalent to the natural dose accurately; this remains an assumption. To this end, Guérin et al.[92] were unable to establish a correlation between dose recovery ratios and the ratio of OSL ages to independent ages. In the final analysis, the accuracy of OSL ages can only be tested by dating material of known age.

[H3] Aliquot specific rejection criteria

Once a suitable SAR protocol has been identified, it is used to measure the D_e in many aliquots. Not all measurements may be of equal value, and criteria based on recycling ratios, recuperation, absence of effect of prior infra-red stimulation on OSL (known as OSL-IR depletion ratios, see **Box 3**[93]) have all been suggested to identify less reliable values[78]. However, the use of any such criteria should be justified. By normalising doses from each individual aliquot to the sample mean, the correlation between recycling ratio, recuperation and OSL-IR depletion ratio, and D_e can be examined across a set of samples, each with a different average D_e[91, 94]. This correlation is done for 54 loess samples in **Fig. 8a,b**, and for these samples at least, there is no justification for aliquot-specific rejection based on either poor recycling ratios or significant OSL-IR depletion ratios. Perhaps surprisingly, this is not unusual [95-99]. To this end, data should only be considered for rejection if there is evidence to suppoer that doing so improves the average dose estimate. However, identifying appropriate rejection thresholds to identify and reject individual aliquots from a single sample may not always be possible. Experimentally, the aliquot-to-aliquot over-dispersion in these measurables can be considerable, such that in comparison the individual estimates of uncertainty on each aliquot are often small.

Quartz dose response curves vary in curvature even within a sample, and some aliquots saturate at lower doses than others[100-104]; this is particularly true for individual grains. For older samples with larger natural doses or when larger given doses are used in dose recovery tests, some aliquots cannot be used to measure the dose of interest because D_c in Equation 6 is too small. In the worst case, said aliquots that cannot be used will not give estimates of D_e. In practice, this leads to unbounded estimates of D_e and/or uncertainty for a number of aliquots, and discarding these values leads to bias.

To avoid this biasing of the D_e distribution towards low dose estimates, aliquots can be sorted by their ability to record large doses or by increasing D_c values (**Fig. 8c**), with aliquots only with increasingly larger D_c values selected[91, 94, 105-107]. As D_c increases, the fraction of aliquots in saturation becomes negligible and the estimate of the central tendency of the equivalent dose or given dose distribution becomes stable.

[H1] Applications

This primer is not intended as a comprehensive review of the OSL application literature, as several such reviews are already available[108-114]. Here, we present illustrative examples of actual and potential applications. Many of these applications were pioneered using thermoluminescence and **IRSL** on both quartz and feldspar, and include the dating of pottery[115], loess[116], colluvium[117, 118], archaeological sediments[119], periglacial features[120], fluvial, marine and aeolian systems[121-123], direct dating of tectonic faults[124], soils[125] and glacier ice[126].

[H2] Quartz OSL in archaeo- and geochronology

Quartz grains must give a measurable fast-component OSL signal in response to ionising radiation for reliable dating. Unfortunately, not all sources of quartz have these characteristics. Igneous rocks are the main source of quartz grains in sedimentary deposits, but grains extracted directly from primary rock do not usually show significant luminescence sensitivity[63, 127]. Consequently, sediments in mountain catchments dominated by primary rocks rarely give a measureable fast-component signal[63]. Sensitivity seems to develop during repeated cycles of erosion, transport and deposition[128] and laboratory studies support this inference[63, 129, 130]. Thus repeatedly reworked quartz grains, such as those in large-scale low-gradient river systems or in deserts, almost always have a strong luminescence response to dose. Once sensitivity has been confirmed, any dating application must also consider: the reliability of the chosen SAR protocol; the degree of resetting by daylight or heat before burial; and the dose rate during burial. Below we review some illustrative dating applications in this context, and **Table 1** summarises different events that can be constrained in time using quartz OSL.

In fired or naturally-heated samples, the luminescence signal follows **Arrhenius** kinetics, where exponential depletion depends on both time and temperature[17]. Typically, heating for one hour at 250 °C or one minute at 300 ºC removes 99% of the fast-component OSL[57]. Such heating conditions are commonly exceeded in the firing of pottery, ceramic bricks and tiles[131, 132], in heated stones[133, 134] and lithics[135], in sediment heated under archaeological hearths[136], and in contact with lava flows[137].

Local temperatures can also be raised a few hundred degrees by frictional heating associated with formation of fault gouges during tectonic movement, or dike injection due to earthquakes, completely

resetting OSL[138-140]. Lightning strikes can cause localised melting in dry sand, creating fulgurites and resetting nearby grains[141].

Since daylight exposure is ubiquitous (Figure 1), most sedimentary settings can be dated using OSL (Figure 9). The bleaching rate depends on both the daylight flux and spectrum[31, 142]. Under water, the depth and suspended particle load reduce photon flux, especially at shorter wavelengths, and turbulence carries particles into and out of the illuminated zone; all these processes reduce the bleaching rate. Sub-aerial transport is thus more effective at resetting OSL than sub-aqueous. Nevertheless, dating is often possible in completely dark sub-glacial, cave, deep lake[143] and deep ocean environments[5, 144] because the sediments were sufficiently exposed to daylight before last entrainment.

[H2] Landscape evolution and past environments

The rapidity of daylight bleaching implies that usually only the most recent transport and deposition event is dated using OSL. Applications in landscape evolution and palaeo-environmental studies are numerous (**Table 1**) and have resulted in major advances in understanding a variety of geomorphic processes, including thresholds, leads and lags[**145-148**]. OSL dating of a wide range of terrestrial sequences has also demonstrated the interrupted nature of terrestrial records[95, 149]. Many deposits record only short and sub-millennial periods of time, often when the climate is changing rapidly from one relatively stable state to another[150-153]. These results have raised questions about the validity of past land-sea and land-ice correlations that were usually based on the assumption of continuous deposition in the absence of numerical chronologies[154-156]. OSL dating has changed our view of the Weichselian ice limits in northern Eurasia (QUEEN project[157, 158]) and the retreat of the British-Irish ice sheet (BRITICE-CHRONO project[159, 160]). It has also provided one of the foundations of the INQUA Dunes Atlas, a global chronological database on periods of inland or continental sand dune accumulation and stabilization[161, 162]. Dating of frost wedges has demonstrated landscape stability over an entire glacial cycle[163] and constrained palaeotemperatures. In addition, OSL dating of sediment covering faults has enabled the constraining of the timing of past earthquakes[164-167].

OSL is also reset by daylight exposure during the vertical reworking of grains by bioturbation (including the formation of biogenic structures such as termite mounds, **Fig. 9e**), pedoturbation and cryoturbation [168-173]. These additional reset mechanisms have led to new research possibilities of relevance to the Anthropocene (Table 1), particularly in understanding critical zone processes and rates of sediment turnover[174, 175]. In a palaeosol developed in a sediment, turbation continually reset grains during soil development and ceased when the surface was buried. Thus grains in the subsoil below the mixing zone are expected to record the time the sediment was deposited, and the now buried topsoil records the time soil formation stopped[172].

All of these processes are climate-driven, or at least climate-dependent. Establishing the absolute timing and rates of change of such landscape development is thus key to identifying periods of climate change, and to establishing the correlations between these local changes and the global climate record[95, 176, 177]. Luminescence is particularly useful among the techniques that can be used to establish such chronologies because it targets the silt and sand grains, which are present in all landscapes.

[H2] Archaeology and migration studies

Quartz OSL dating has made significant contributions to Holocene archaeology, including dating of Neolithic settlements[178, 179], Archaic mound complexes in the Americas[180], Bronze and Iron Age middens [181], rock art[182, 183], medieval bricks[184], mortar [185] and stone surfaces[186-188]. On longer time scales, the diverse sedimentary environments dated using OSL also served as habitats for past human and faunal populations. As a result, quartz OSL is the preferred dating tool in many anthropological and palaeontological applications (**Table 1**). This preference holds despite the greater precision of other techniques such as argon-argon or U series dating. In contrast to OSL dating, argon-argon or U series dating are very restricted in application (for example, argon-argon dating targets infrequent volcanic **ejecta**), and even if applicable, usually only give a small number of ages in a section.

OSL dating has made major contributions to debates on the timing of human evolution and migration and on changes in palaeoecology, especially for events beyond the limit of radiocarbon dating (~45 ka). Important results include timelines for Out-of-Africa dispersals of *Homo sapiens*[189-194], the earliest known human settlement of Australia[195-198] and possibly of the Americas[199, 200], occupation dynamics of Neanderthals and Denisovans[201, 202], key evolutionary, behavioural and cultural turning points across different human species[203-206], and the late Pleistocene megafaunal extinctions in Australia and the Americas[207-210].

[H1] Reproducibility and data deposition

Complexities in OSL dating arise from four main factors: limited net daylight flux causing some grains to not completely reset at deposition; different OSL signals from different grains in response to the same radiation, heating and optical stimulation; different radiation fluxes to different grains because of heterogeneity in mineralogy, grain size and burial matrix; and open system deposits leading to time-dependent radiation fluxes because of post-depositional mixing, geochemical and diagenetic processes, and variable water contents.

Limited net daylight flux leads to heterogeneity in the apparent D_e. Different OSL signals from different grains lead to heterogeneity in the apparent D_e, and both different radiation fluxes to different grains and open system deposits lead to heterogeneity in dose rate and thus in natural dose. All of these factors affect the ease with which OSL dating can be applied in different settings (summarised in **Fig. 10**).

[H2] Heterogeneity in D_e

The major factors affecting the complexity of determining D_e are discussed below. Their relative significance is summarised in **Fig. 10a** shows that, for example, aeolian sediments are likely to show low complexity (furthest from the centre), because they tend to be well bleached (red band) and have good luminescence characteristics (dark blue band), both with low variability (width of the band). In contrast, glacial sediments are likely to show high complexity (close to origin), because they tend to be poorly bleached and have poor luminescence characteristics with considerable variability (width of red and dark blue bands). Bleaching becomes progressively less important and contributes less to variability as the burial age increases. The complexity arising from bleaching therefore decreases with age, whereas complexity from luminescence characteristics is at a maximum for oldest sediments, mainly because of dose saturation effects, and a minimum for medium age material, where signals are strong and the saturation effects are small.

The nature of grain transport by wind or water implies that every grain is exposed to a different daylight flux and spectrum. Thus, for short transport duration under attenuated daylight, the latent OSL signals from different grains are reset to different degrees, and only when the exposure is of sufficient duration will all grains be fully reset. Field environment and age are the major factors affecting the completeness of bleaching, and they dictate the position and width of the red band in **Fig. 10a**. In general, given the wavelength-specific attenuation in a water column, and the wavelength dependence of bleaching, the grain-to-grain variability of bleaching in water-lain sediments is greater than in aeolian sediments. Nevertheless, some flood deposits are surprisingly well-bleached[211, 212] suggesting that significant bleaching occurred before fluvial entrainment or sub-aerially during low flow.

If all grains are fully bleached and the dose rate is homogeneous, the D_e distribution of a sample should be centred on a single value with dispersion accounted for by random measurement uncertainties[48, 213, 214]. Unfortunately, this is rarely, if ever, the case. Additional dispersion in D_e originates from differences in the behaviour of OSL signals from different grains, and this compromises both the accuracy and precision of the chosen SAR protocol (see the dark blue band in Figure 10a, which represents intrinsic sources of dispersion). These difficulties arise because the luminescence from different grains responds differently to radiation, heating and optical stimulation [91, 104, 106, 215, 216] or because of different charge transfer properties and different OSL signal compositions[59, 217-219]. In addition, the process of interpolation onto the dose response curve (**Fig. 7**) will give rise to an asymmetric dose distribution with an increased dose-dependent dispersion compared to that of the OSL distribution. At the limit, a fully saturated sample gives an incorrect, apparently bounded, dose distribution (**Fig. 7**), with the potential to be misinterpreted as a poorly bleached distribution or as mixture of a finite dose with a saturated sample.

In addition to complications arising from these intrinsic factors, D_e dispersion also arises from extrinsic sources such as variations in bleaching, mixing, and dose rate. When dispersion in D_e is significant, complex statistical analysis may be necessary[77, 213, 220-225] to extract the dose component of interest. It is not straightforward to differentiate between intrinsic and extrinsic sources of dispersion because we do not have a way of independently measuring the extrinsic component. As a result, any dispersion greater than that determined in laboratory experiments is simply assumed to be extrinsic[53]. However, there are cases where this assumption is incorrect[94].

Although the size of the apparent residual dose remaining after bleaching is independent of the subsequent burial time, this burial timing affects the residual dose by affecting 'bleaching' (see red band in Burial age in **Fig. 10a**). There are three approaches to investigating whether a sample is likely to have been sufficiently bleached at deposition: first, modern analogue samples[226] provide site-specific evaluations of bleaching conditions[111, 227, 228], which assume that the net effects of transport and deposition on bleaching have not changed through time. In general, modern analogues have not completed their transport at the time of collection and because most recently deposited sediment is held in ephemeral storage such as point bars, it is likely to be reworked again before final deposition in long-term storage. Thus modern analogues will tend to underestimate the degree of bleaching available in the environment[226]. The second approach involves examining the self-consistency of OSL dating through measurement of different minerals with different luminescence signals. For example, paired dating comparisons of quartz OSL and K-rich feldspar IRSL or post-IR IRSL, where the two feldspar signals are optically reset at different rates, can be used to confirm that all quartz grains in a sample were completely bleached prior to deposition[229-231]. Finally, the third method uses single-grain OSL dating to examine heterogeneity in D_e in sediments from environments with likely limited daylight exposure or post-depositional alteration[114, 232]. In such cases, heterogeneity in radiation dose rate at the individual grain level must also be considered (see below).

Unfortunately, analytical models based on the widely-used Central Age Model (Gablbraith et al., 1999; such as the Minimum Age Model (Ref. Galbaraith et al. 1999) and Finite Mixture Model (Roberts et al., 2000)) do not take this dose rate heterogeneity into account and so risk producing biased estimates of De (Guérin et al., 2017, QG).

This can be illustrated by considering a hypothetical sample in which the distribution of dose-rates dominates the natural dispersion. Suppose this to be a well-bleached, well-behaved sample in which the uncertainty on the measurement of dose is negligibly small (e.g. 1%). All grains must by definition record the same age. Suppose this sample is 10 ka old, and that the environmental dose rate is made up of two equal but spatially separated (at the grain scale) contributions, one of 1Gy.ka^{-1}, and one of 10 Gy.ka^{-1}; we would measure an average dose rate of 5.5 Gy.ka^{-1}. Now consider the dose - on average, 50% of the grains absorb a burial dose of 10 Gy, and 50% a dose of 100 Gy. If these two doses could be measured individually, each with some similar overall uncertainty, then the unweighted average dose would be 55 Gy, the geometric mean 31.6 Gy and the weighted average 10.9 Gy. Only the average dose

gives the correct age of 55/5.5 = 10 ka; the geometric mean age is 31.6/5.5=5.7 ka, and the weighted data give 10.9/5.5=2.0 ka.

Of course such simple bi-modal distributions do not exist in nature, but the point remains – when only an average dose rate is known, and the dose rate is a major factor in dispersion, the dose must also be an average, or the age estimate is likely to be biased. This is particularly true of large aliquots, where the dose is in any case averaged as a result of the large number of grains giving light in each aliquot, and analytical uncertainties on dose estimates from each aliquot are very much smaller than the data dispersion. This point is made in Guerin el al. (2017), where the implications for the analysis of dose distributions are discussed in detail.

Site stratigraphy and grain sorting are of considerable importance to reliable OSL dating (**Fig. 10a**). Sediments affected by significant post-depositional mixing via, for example, bioturbation, freeze/thaw cycles, tectonic activity, or cultivation should be avoided as these processes can lead to significant dispersion in D_e values, but sampling potentially-mixed sediments may be unavoidable at times. In some cases this mixing is obvious but not always, and the presence of distinguishable components in small-aliquot or single-grain dose distributions has been used to infer mixing[233, 234]. These dose populations can be modelled as a mixture of discrete components using the Finite Mixture Model[235], and typically the dominant component is chosen to provide the deposition age[234, 236-239]. However, such analyses can imply unrealistic degrees of physical mixing between non-adjacent layers even in deposits where mixing can safely be ruled out[94], suggesting that the distributions identified by dose mixing models may not necessarily arise from physical mixing[240]. Together with the inability to derive component-specific dose rates for mixed sediments (see below), this calls into question the application of dose mixing models for dating purposes

[H2] Heterogeneity in dose rate

The major factors affecting dose rate complexity are discussed below, and their relative importance is summarised in **Fig. 10b**.

Dose rate evaluations become demanding when the infinite matrix assumption is no longer applicable [52] (red end of the 'Dimension of deposit' bar in **Fig. 10b**). Sand-sized quartz grains have a scattered β spectrum range comparable to that in sediments; the larger the grain, the higher the attenuation of the external β dose rate (Supplementary Table 4). In addition, the distribution of radionuclides at the grain scale in sediments is spatially heterogeneous with variations in both internal and surface-bound radioactivity. Thus 'hotspots' of higher radioactivity, such as K-feldspar and zircons, or 'cold spots' of lower radioactivity, such as carbonate nodules, result in significant variations in the β dose rate to individual grains. This spatial variability can be observed[135, 241, 242], modelled and, on average, accounted for[53, 54, 243], but the association of spatially-varying β doses with individual grains from which a D_e has

been estimated is currently not possible. Such variability is usually lower in a well-sorted deposit (green end of 'Sorting' in **Fig. 10b**).

Heterogeneities on a scale of tens of cm affect the γ ray dose rate, which may result from the proximity of a sample to a large rock fragment of a different mineralogy, or from interfaces between different stratigraphic units (see Appendix H in[17]). While in many cases these heterogeneities can be avoided, the choice of sampling location is often restricted in archaeological sites. In that case, the γ dose rate to samples collected close to stratigraphic interfaces may require modelling[244] or in situ γ dose rate measurement using luminescence dosimeters or field γ spectrometers[25-28, 30, 245, 246].

Water content is particularly important (see **Box 1**) as it reduces the dose rate compared to a dry matrix[17, 247], and a 1% change in water mass fraction typically results in a 1% change in apparent OSL age. Thus, a low value for 'Saturated water content' (**Fig.10b**) reduces the possible range of water contents during burial, and therefore reduces the dependence on assumptions concerning 'Fraction of saturation' of water content (**Fig. 10b**). Whatever the saturated water content, if it is likely that for the entire burial period the sample has either been dry, for example desert sand, or fully saturated, for example below the water table, then uncertainties arising from assumptions are much reduced. The least desirable condition is a sample in a temperate climate vadose zone, where the average fraction of saturation throughout the burial period is poorly defined (see red centre of band in **Fig. 10b**). In such cases, there may be no alternative to assuming 50% of saturation with some appropriately large uncertainty on that value.

The dose rate is also affected by temporal changes[55, 248]. For instance, post-depositional changes in burial depth can be important for shallow burial (see red end of 'Overburden thickness' in **Fig. 10b**). Changes due to erosion or deposition increase complexity by affecting both γ and cosmic ray dose rates[16], but are likely to be less important for deep burial (see green end of band in **Fig. 10b**). Density changes due to porosity alone do not change dose rates because the density of air is too low to absorb significant amounts of energy. However, density changes arising from time-dependent carbonate infilling/leaching of pore space, or oxidation of organic material, change the effective dose rates and the saturated water content (**Fig. 10b**)[249, 250], which directly and indirectly increases complexity (see Supplementary Tables 5-6 for correction factors).

The dose rate may also change because radionuclides are imported/exported from a volume of sediment. Radionuclide concentrations are affected by water movement, which may import specific radionuclides into secondary minerals or leach them by reduction and/or hydrolysis with time, particularly ^{40}K, ^{238}U, and ^{226}Ra (a shorter-lived member of the ^{238}U decay series[21, 23]). This import/export leads to disequilibrium in the ^{238}U decay series and possibly time-dependent dose rates[251]. In addition, the 3.8 day half-life of the noble gas ^{222}Rn (^{238}U series) allows migration through sediment pores before decay.

Diffusion dominates for partial pore-filling by water, but bulk transport can occur if water moves through a deposit[252], with losses of 50% at 5 m depth in sand having been reported[253]. Although the post-^{222}Rn part of the ^{238}U decay series contributes the majority (>75 %) of the β and γ dose rate from the ^{238}U series (Supplementary Figure 3), for a typical sandy sediment containing 20 Bq.kg^{-1} ^{238}U and ^{232}Th and 300 Bq.kg^{-1} ^{40}K (1.5 and 5 ppm, and 1% respectively), the contribution to the total dose rate is <20%. A combination of thermal ionisation mass spectrometry and high-resolution γ spectrometry can be used to describe the state of equilibrium of, for example, the ^{238}U decay series, but in most cases, disequilibria have rather small effects on the OSL age.

Finally, any significant 'post depositional mixing' (see red end of bar in **Fig. 10b**) increases the challenge of determining a time averaged dose rate. In a mixed deposit, grains will have absorbed dose in potentially different dose rate environments before mixing, but only the mixed dose rate is measurable today. Without knowledge of the dose rates in the source deposits contributing to the mixture and of the timing of the mixing, reconstruction of an average dose rate is uncertain.

In summary, dose rates at the grain level are likely to be variable during burial. This variability must be taken into account when using the age equation, and accurate ages should be calculated using a model which delivers average estimates of the absorbed doses during burial (Guérin et al., 2017, QG).

[H2] Checking reproducibility

One way to reduce the impact of the various methodological issues discussed above is through internal and external checks on reproducibility. These may, for example, involve collecting a suite of OSL samples targeting different types of sediments preserved in clear stratigraphic relationships, or by collecting replicate samples from the same horizons[95, 99, 198]. Although resource-intensive, multiple-technique and multiple-sample OSL dating strategies are recommended in all dating applications[95-97, 105, 135, 198, 201, 231].

Statistical uncertainties associated with individual laboratory measurements -conventionally given at 68% confidence intervals in luminescence dating- are typically 2-3%, both on natural dose measurements involving OSL and on dose rates (as determined from γ spectrometry). These random uncertainties can be reduced by increasing the number of measurements, but this requires a considerable increase in instrument time per sample and is often impractical. Studies involving high-density sampling from large stratigraphic sections frequently report over-dispersed ages, where the ages are more variable than expected from analytical uncertainties alone (see **Fig. 11a**[95]). This suggests that reductions in measurement uncertainty would be of limited benefit. Note that Figure 11a does not include the systematic uncertainties common to all the ages in the section, and that the error bars represent random uncertainties only.

The stated uncertainties on calibration standards are also ~2-3%, both for the γ-irradiated quartz [47] used to calibrate laboratory β sources and for the geochemical standards used for the calibration of equipment used in dose rate determination[254]. Together, these contributions result in typical total calculated uncertainties (random and systematic) on an OSL age ranging 5-10% (Supplementary Table 7). Currently, 5% is considered a minimum uncertainty for a sample in an ideal setting and >10% for unfavourable cases involving, for instance, low luminescence sensitivity or saturation of OSL with dose.

Perhaps because OSL dating is a relatively young method, with the present methodologies dating back to the 2000s and most laboratories small with fully committed instrumentation, the community has yet to develop a routine of inter-laboratory comparisons. The only exception is an exercise in which 26 different laboratories dated a beach-ridge sand selected for its good OSL behaviour[255]. The dispersion in the 26 ages (~18%) significantly exceeded the uncertainties on individual ages as estimated by the various participants. Some of the dispersion arose from different assumptions: for example, the use of a 'typical' internal dose rate to quartz by some, while others ignored this possible contribution. In this study, it is clear that the community, as a whole, underestimated the uncertainties they assigned to individual age estimates.

In addition, laboratories make use of either their own age calculation software or one of the more widely available packages, such as DRAC[256], RLuminescence[257] or numOSL[258]. These software all include underlying, often dissimilar, default assumptions, and a rigorous comparison of these packages is highly desirable but not yet established.

Until recently most articles containing luminescence ages presented new data with a variable degree of detail. However, publications addressing larger scale questions and requiring meta-analyses of published datasets are becoming more frequent. It is thus increasingly important that all published OSL ages are accompanied by underlying data of sufficient detail to allow the reader to reproduce the age calculations and reliably compare ages from different laboratories. An example of the minimum sample specific information necessary for such calculations is given in **Table 2**. There should also be text describing the experimental parameters and the results of any additional performance tests, especially dose recovery experiments. We hope that all journals, even those without specific interests in the technicalities of dating, will encourage authors to publish such information.

[H1] Limitations and optimizations

The problems encountered in quartz OSL dating often depend on the age of the sample. The ability to date young samples with small doses depends on the sensitivity of the luminescence signal to radiation. For less sensitive quartz, it can be difficult to detect a measurable fast-component signal above the instrument's background and slower decaying OSL signals. Thus dating young desert dunes is much

more likely than dating young mountain-valley slope deposits (see **Fig. 10a**). Also, thermal transfer can usually be avoided by a low temperature preheat (**Fig. 6b**).

For older sediments, it may take weeks of instrument time to collect the data required for a single age, which is a major restriction for laboratories with limited instrumentation. Standardised dose-response curves are sometimes suggested to reduce this measurement time[100]. For large suites of samples with similar properties such as, for example, a loess section, the average responses of multi-grain aliquots of quartz follow a common dose-response curve as demonstrated by examining a sub-set of the suite [259]. In such cases, individual L_n/T_n values can be interpolated on to this common dose-response curve to determine individual D_e. This approach is potentially useful for younger, homogeneous samples within the linear part of the dose-response curve[100, 260, 261]. However, there can be significant reproducibility issues with less homogeneous material, and particularly as the dose-response curve approaches saturation.

More generally, the apparent behaviour as the laboratory dose response curve approaches saturation may be misleading. The controls on luminescence saturation with dose are poorly understood. The luminescence from individual grains and sometimes from multi-grain aliquots can saturate at very different doses, continue to grow without apparent saturation, or even decrease at high doses[101, 262]. However, quartz often underestimates the true age at large doses (150-250 Gy) [64, 66, 263] and it seems likely that at these large doses the laboratory dose response curve does not reflect the natural dose curve [65, 264, 265]. One way to address this very important question is to investigate natural dose response curves using homogeneous material from sections with a well-known age model, such as some well-studied loess sections[65, 266]. New measurement strategies and statistical tools have also been proposed with the aim of increasing the range of single-grain OSL[267, 268].

[H2] Overall accuracy

The overall performance of sand-sized quartz OSL to date samples from a variety of deposition environments, each with independent age control, has been evaluated by others[89, 108, 269]. These data sets are combined in **Fig. 11b**, for 249 ages there is now a considerable body of data suggesting that OSL dating is accurate over a time span of more than four orders of magnitude (**Fig. 11b**), and that the precision and accuracy are largely in the range originally predicted.

[H1] Outlook

Over the last twenty years, dating based on the quartz fast-component OSL signal has become an important tool in the geochronology of the past 500 ka. The method is still undergoing rapid development and improvement and exciting new areas of application are waiting to be explored.

The origins of intrinsic over-dispersion in D_e, both at the multi- and single-grain level[48, 232], begs further investigation. An improved understanding and quantification of these intrinsic sources would, in turn, enable more reliable quantification and interpretation[242] of the contribution to dispersion from extrinsic sources, such as incomplete bleaching and mixing. Limits on the upper dose range of the OSL signal are also poorly understood. Laboratory dose response curves often increase to large doses (hundreds of Gy), but natural doses either do not increase above ~200 Gy, or if they do, they often appear to be an underestimate[66, 263, 270]. An improved understanding of the fast-component dose response curve at high doses would increase confidence in older ages and help to extend the datable range. Other quartz signals such as Violet Stimulated Luminescence[7, 271] and Thermally Transferred OSL[272-274] also have the potential to date older material, but both require further research.

Accurate calibration of laboratory radiation sources is an active research area[47, 275] and a regular programme of radiation source comparisons is desirable.

Addressing these issues should help improve luminescence age accuracy to the probable minimum of ~5%. As the demand for OSL dating continues to grow, the demonstrated benefits of a high stratigraphic age density to site interpretation[148, 198, 276-278] will only increase this demand further.

Single grain dating has demonstrated its potential for dating incompletely bleached deposits [213, 225, 279, 280] but inherent dosimetry uncertainties likely prevent the accurate dating of deposits subject to significant post-depositional mixing[77]. For unmixed deposits, the ability to determine dose rates specific to the individual grains giving a D_e would likely produce a step change in interpretation and application.

Field measurements of OSL have been demonstrated[281-283] and the ability to determine approximate ages ‘on site’ would be valuable. Although there is no technical impediment, calibrating the signal in terms of dose requires a portable ionising radiation source, which has regulatory barriers to overcome.

Direct dating of buried rock surfaces is rapidly growing[127, 284], although quartz applications are limited to sandstones and quartzite clasts because of sensitivity. One advantage of direct dating is that a rock surface records its history of daylight exposure, which eliminates the uncertainty in whether it was sufficiently bleached[187, 188, 285, 286]. The potential applications in both geology for cobble fans, moraines, scree/talus, and rock falls, and in archaeology for megaliths, field boundaries, buildings, and lithics, are considerable. Interest in the inverse problem of dating the length of daylight exposure of a rock surface is just beginning[127, 287] and currently requires a known-age calibration surface[15, 287]. However, the potential of this method is considerable, especially in archaeology.

Finally there is considerable opportunity to use the signal remaining after daylight exposure to investigate geomorphological processes, such as the relative importance of supra/sub-glacial transport[288] or fluvial residence time[289].

OSL dating of quartz continues to expand its fields of application beyond those mentioned in this Primer. The method continues to develop, and will undoubtedly contribute further to our understanding of Earth surface processes.

Glossary

(Some definitions are specific to the context of this Primer. Where appropriate, units are given in square brackets, e.g. [s^{-1}])

The **Arrhenius** equation states that, for an electron to escape a trap, it must first acquire a minimum amount of energy, called the activation energy E_a. Then the rate of thermal eviction of trapped electrons is given by $Ae^{-\frac{E_a}{k_B T}}$. The 'frequency factor' A can be seen as the number of attempts to escape made by the trapped electron, and $e^{-\frac{E_a}{k_B T}}$ as the probability that any given attempt will result in an escape at a particular absolute temperature T. k_B is Boltzmann's constant.

α particles: ionising radiation in the form of energetic helium nuclei produced by nuclear decay.

Anthropocene: a proposed geological epoch covering the period of significant impact on Earth's geology and ecosystems by humans.

Ar-Ar (or K-Ar) dating: a dating technique based on the decay of ^{40}K to ^{40}Ar.

β particles: ionising radiation in the form of energetic electrons produced by nuclear decay.

bioturbation: after initial deposition, the reworking of sediment by biota (plants, animals, etc).

Bq: Becquerel, a nuclear disintegration per second. [s^{-1}]

cal BP: calibrated ^{14}C years before present (referred to AD1950). Only used for ^{14}C ages, after conversion to calendar years by calibration. [a]

Central Limits theorem: states that the sum of independent random variables tends toward a normal distribution, even when the original variables themselves are not normally distributed

cosmogenic radionuclide dating: any one of several methods to date length of exposure of minerals at the surface (or sometimes length of burial) using the build-up or decay of radioactivity induced by cosmic rays.

coversand: a continuous layer of sand deposited by wind, often in a coastal environment.

crotovina: An animal burrow that has been filled with material from overlying sediments.

cryoturbation: the reworking of sediment after initial deposition by the freeze/thaw cycle.

dark count rate: the count rate from a photon detector completely obscured from light. [s^{-1}]

dose: total amount of energy absorbed per unit mass from ionising radiation. [Gy]

dose rate: the rate of energy absorption from ionising radiation during burial

D_c (or D_o (letter o)): a constant used to describe the curvature of the luminescence response to dose, usually in an expression of the form $Y=A(1-\exp(-D/D_c))$. [Gy]

D_e: equivalent dose, the laboratory dose that induces the same luminescence response as the natural dose. [Gy]

ejecta: material thrown out by volcanic eruption.

fast-component: the part of the signal that decays most rapidly during stimulation

feldspar: a group of K-, Na- and Ca-rich aluminosilicate minerals, makes up ~40% of the Earth's crust.

frost wedges: cracks formed in frozen ground, often filled with sand; this preserves them in the sedimentary record.

FWHM: Full **W**idth at **H**alf **M**aximum, a numerical description of the width of a peak in data or response.

γ rays: ionising radiation in the form of energetic photons produced by nuclear decay.

Gy: Gray, energy absorbed per unit mass from ionising radiation. 1 Gy = 1 Joule/kg [$J.kg^{-1}$].

igneous rock: formed by the solidification (crystallisation) of magma or lava.

IRSL: Infra-red stimulated luminescence

ka: thousands of years. [a]

λ: lambda, the nuclide-specific probability of a nuclear decay. [s^{-1}]

leads and lags: in climate science, the difference in timing between changes in two correlated climate phenomena (e.g. build-up of global ice and changes in regional dust deposition).

loess: wind-blown dust (predominantly silt-sized (4-63 μm) grains)

luminescence signal: the luminescence response, L_i, to any dose, divided by the response, T_i, to a subsequent fixed test-dose, i.e. L_i/T_i

midden: in archaeology, a refuse pile of domestic waste.

Neolithic: the most recent division of the Stone Age (last ~12 ka), and associated with the development of farming.

optically stimulated luminescence – OSL: the luminescence signal observed when stored charge is stimulated (evicted from traps) by visible or near-visible light.

overburden: the material covering some geological feature of interest.

palaeosol: a fossil soil (i.e. one no longer forming); usually found buried within a sequence of sedimentary units.

pedoturbation: the reworking of sediment after initial deposition by the geochemical and biological processes of soil formation.

primary rock: any rock that formed by solidification (crystallisation) from the melt.

Quantum efficiency: how many photons are required to give a detected event, and the effectiveness of photon to electron conversion

quartz: the most common natural form of the compound SiO_2, makes up about 20% of the Earth's crust.

radiocarbon dating (or ^{14}C dating): a dating technique based on the decay of ^{14}C. Can only be applied to material of organic origin.

Reset: in the case of luminescence, set to zero or 'bleached'

secular equilibrium: where the production and decay rates of each nuclide in a decay chain are almost identical.

sedimentological boundaries: strictly, distinct breaks (unconformities) between bodies of sediment. Often used more informally to describe gradational boundaries.

SAAD - Single Aliquot Added Dose: a single aliquot procedure for determining D_e, by adding doses to the natural dose and measuring the growth of the resulting luminescence signal.

SAR - Single Aliquot Regenerative dose: a single aliquot procedure for determining D_e, based on resetting the luminescence signal to zero between each measurement of luminescence, whether resulting from natural or laboratory doses

$\tau_{½}$ - half life: The period of time taken for 50% of a particular radionuclide to undergo radioactive decay and change into another element. [s]

thermoluminescence: the thermally stimulated luminescence signal observed when a sample is heated to evict stored charge from traps.

threshold: In climate science, the point at which a small change in a physical or chemical parameter (e.g. global temperature) can lead to a tipping point in outcome and a shift to a new equilibrium state of range of average conditions (e.g. massive loss of global ice mass)

vadose zone: in a porous body (e.g. of sediment), that part lying between the ground surface and the water table.

Figures captions

Figure 1: The origins of the luminescence dating signal in quartz. (a) energy is absorbed (dose) as α and β particles and γ rays emitted during the decay of naturally occurring radionuclides (especially ^{238}U and ^{232}Th series, ^{40}K) penetrate quartz grains. The different ranges of the various emissions are indicated, relative to typical grain dimensions. Cosmic rays also contribute to the dose. (Redrawn from[290]) (b) Energy from ionising radiation is absorbed by an electron (e^-, filled blue circle), which migrates through the grain until it is trapped at a defect in the lattice structure (electron trap). The corresponding 'hole' (h^+, literally the place where an electron should be, unfilled orange circle) also migrates until it is trapped in a different kind of defect (hole trap). This process stores energy. (c) Shining blue light on the crystal gives the trapped electron sufficient energy to escape the trap (optical stimulation). When it then recombines with the hole, it releases the trapped energy as a more energetic UV photon (optically stimulated luminescence).

Figure 2: The relationship of the erosion, transport and sedimentation cycle to the acquisition and loss of a luminescence dating signal (a) any existing energy stored in the quartz crystal structure is released by daylight exposure (i,iii,v) during different erosion and transport events, by wind, water, ice, gravity or turbation (see (b)). These periods of resetting are interspersed with periods of burial (ii,iv,vi), during which dose is absorbed from natural radiation (Figure 1). Sufficient net daylight exposure completely removes the previously stored energy (e.g. during i and v), otherwise it is only partially reset (iii). This energy builds up again during the most recent burial (vi), until the quartz sand grains are sampled (vii) and taken to the laboratory. After cleaning, they are then exposed to blue light, and the luminescence signal acquired during last burial is measured. (b) illustrates the various transport agencies that can lead to daylight exposure of mineral grains before final burial (gravity acts as an independent transport agency only on high gradients).

Figure 3: Sample preparation and instrumentation for OSL measurement. (a) The laboratory steps used to extract quartz grains from a tube of sediment. Note the alternative processing routes, depending on whether feldspar is also required. All these steps should be performed under subdued lighting conditions, using a wavelength and intensity that avoids significant effect on the trapped charge population[9]. Q: quartz, H: heavy minerals, F: feldspar, NF: sodium-rich feldspar, KF: potassium-rich feldspar. The combined water drops [] and fan symbol [] indicate thorough washing and drying. (b) The main components in an OSL measurement system. After irradiation in nature or in the laboratory, the quartz is heated to the desired temperature, and the stimulation light turned on. The photons making up the optically stimulated luminescence pass through the detection filter to the photon detector, to give the time dependent signal shown at the top.

Figure 4: Using SAR to determine the equivalent dose, D_e. (a) T_i and (b) L_i plotted against dose for an aliquot of heated brick quartz; some T_i are labelled to indicate measurement order. (c) Sensitivity-corrected (L_i/T_i) growth curve obtained by dividing data from (b) by data from (a); inset, stimulation curves for natural signal and calibration quartz[47]. (d) - (f) same as (a)-(c) but for quartz extracted from sediment. (Heated brick - 173701; monastery floor, Sweden. Sediment - 175405; Kalahari Desert, Namibia.) Open triangles show the response to D=0 Gy. Other open symbols indicate repeated dose measurements. Note that without sensitivity correction the repeated values of L (in b,e) are inconsistent with earlier measurements at the same dose; correcting for sensitivity change by diving by T_i corrects this (in c,f). The interpolated doses ('D_e' in b,e and D_e in c,f) and dose response curve shapes are also significantly different between the uncorrected and sensitivity-corrected data.

Figure 5: Correcting for sensitivity changes using the luminescence response to a test dose. (a) The proportional relationship between L_i and T_i for a large aliquot (containing hundreds of grains) of 180-250 µm quartz extracted from a fired brick (filled red circles, 19 cycles) and a quartz aliquot from a desert sediment (filled blue circles, 42 cycles), determined using the SAR sequence in (b). The natural signals (L_0/T_0) are shown as open circles. Same samples as in Figure 4; sediment: D_i=44.4 Gy, D_T=5.9 Gy; fired brick: D_i=3.6 Gy, D_T= 1.0 Gy. Both datasets are consistent with straight lines (dashed) going through the origin, indicating that the ratio L_i/T_i is constant for each sample. This is despite the considerable sensitivity change recorded by T_i (also shown inset as a function of measurement cycle, normalized to first test dose measurement). As is common, the heated quartz displays a greater sensitivity change during SAR measurements than the quartz extracted from sediment. (b) Typical SAR measurement sequence. In the first cycle, i=0 and D_0 is the natural dose, or the given dose in a dose recovery experiment. After completing a cycle (step 6 or 7), the sequence returns to step 1 as required.

Figure 6: Dependence of D_e and dose recovery ratio on thermal pretreatment (see text for details). (a) Preheat plateaus for sand-sized quartz extracted from loess (D38141[95], coversand (OS-B[96]) and heated sediment from a charcoal kiln (GLL-184301[291]). For all three samples the D_e is independent of preheat temperature over a wide temperature interval (dashed line). (b) Thermal transfer plateaus for sand-sized quartz extracted from a fluvial sand (GLL-160301[292]) and a beach ridge (OSL43[293]). Quartz aliquots were bleached at room temperature twice using blue light stimulation to remove the natural OSL signal before measurement of the thermally transferred dose. The effect of thermal transfer becomes visible for preheats ≥200°C. (c) Dose recovery plateau for sand-sized quartz extracted from Chinese loess. The measured to given dose ratio is insensitive to preheat temperature over a wide temperature range. (d) Histogram of dose recovery results measured with a preheat temperature of 260°C. Adapted from[99].

Figure 7: Effect of sublinear dose response on apparent dose distributions (based on[294]). Monte-Carlo-modelled normalised OSL distributions shown on vertical axis, centred on 20% (black), 86%

(blue), 95% (green) and 100% (red) of saturation, each assumed normal with a relative standard deviation of 5%. The resulting interpolations onto a dose response curve (D_c=45 Gy, solid pink) are given on the dose axis, with medians connected using intersecting lines. Each dose median is also shown in Gy, followed by the ratio of the median to the expected dose and the % of results giving a non-finite dose in parentheses; the arithmetic means and geometric means are all within 3% of these medians. Note that the dose median shown for 100% is the apparent value, ignoring non-intersecting OSL signals. The true median lies at infinity.

Figure 8: Testing aliquot rejection criteria. The relationship between D_e and recycling ratio (a) or OSL IR depletion ratio (b) for large aliquots (containing many hundreds of grains) of 90-180 µm quartz extracted from Chinese loess. Upper figures show the individual aliquot D_e values (normalized to the average D_e of each sample) as a function of recycling ratio and OSL IR depletion ratio. Lower figures show the recycling and OSL IR depletion ratios as histograms with mean ratios plotted as blue and red dashed lines, respectively. From the upper figures it can be seen that there is no relationship between the measured D_e and the recycling or OSL IR depletion ratio; rejection of aliquots based on recycling or OSL IR depletion ratios is not justified. Figure adapted from[95]. (c) Effect of D_c filtering on grains with different D_c. The dose recovery data (red data, given dose 170 Gy) shows the effect on the dose recovery ratio of only accepting results from aliquots with increasingly larger D_c values. These data suggest that only those grains with D_C > 125 Gy give accurate results (red data). Even with this minimum D_c, ~3% of the accepted grains still give measured doses in saturation (black data). Sample from Covalejos cave (Northern Spain)[295]

Figure 9: Opportunities for bleaching of the OSL signal in different environments. (a) Aeolian transport during dust storms (Pavliha-istockphoto.com). (b) fluvial transport (Marek Uliasz race.fit2paddle.com). (c) gravity-driven debris fans (unknown) (d) sediment transported by ice (Michael Hambrey - Glaciers online). (e) bioturbation - termite mounds (ourterritory.com).

Figure 10: Sources of complexity in estimations of dose and dose rate. (a) The likely complexities in D_e determination arising from luminescence characteristics (dark blue band) and bleaching (red band), expressed qualitatively in terms of field observables and expected age (see [H1] "Reproducibility and data deposition" for details). These observables and estimates are shown on the 10 radial axes, grouped according to Depositional environment and implied transport mechanism (very light blue), Sedimentology (light blue) and the expected Burial age of the samples (medium blue). "Young" refers to quartz grains with expected D_e values of less than ~10 Gy, "Old" to quartz grains with D_e values of larger than ~130 Gy. Each axis is scaled from most complex (centre of the figure) to least complex (outer edge of figure). The likely variability of each feature is shown by the band width on a particular

axis. There is no reason to expect a correlation between luminescence characteristics and sorting/stratification, and so there is no dark blue band in that portion of the figure. (b) Bar chart showing qualitatively the relative influences of different sedimentary characteristics on dose rate complexity. Each bar depicts an observable sedimentary characteristic (y-axis) that can be evaluated at the time of OSL sample collection or during sample preparation (white labels – present at the time of deposition; black labels – post-depositional alteration). Each sedimentary characteristic varies from low to high (x-axis), and the gradational colouring indicates the degree of beta, γ and cosmic dose rate complexity (in both space and time) expected for a given category value.

Figure 11: Accuracy and precision in quartz OSL dating. (a) Large aliquot 63-90 um quartz OSL ages plotted as a function of depth for a section of Chinese loess encompassing last glacial loess and Holocene soil. Uncertainties are random only. A Bayesian model (with 1σ error band) is also shown illustrating how higher precision can be achieved. Ages excluded from modelling are from samples deliberately taken within **crotovina**. Figure modified from SI in[95]. (b) Comparison of OSL ages determined using quartz from well-bleached samples with independent age control (n = number of samples, followed by the % of samples within ± 2σ of the line of unit slope)[89, 108, 269].

Boxes

[bH1] Box 1: Water content estimation

Constraining the average water content of a deposit is important to the accuracy of a luminescence age, because a 1% increase/decrease in lifetime average water content typically leads to a 1% increase/decrease in derived age[a]. Well-sorted sands have a small variation in porosity, from fully (~38%) to loosely (46%) compacted[296], and because the grain surfaces are in physical contact (in contrast to for example, clay-rich deposits) it is very difficult to over-compress sand by increased overburden pressure. When fully saturated with water, 42% porosity corresponds to 21% by weight water content. A saturation water content can be readily estimated using for example, the syringe method[b] because this packing density is reproducible, in a sandy deposit. If the sediment was below the ground-water table throughout the burial period, this is the lifetime average water content. Otherwise, the fraction of saturation during the burial period must be estimated from an understanding of the local hydrology (drainage, precipitation, etc.) and sediment characteristics[297]. The observed water content, such as the water content in a field sample measured by drying a known weight of wet material, can often be taken as a lower limit to lifetime water content because typical sampling sites (cleaned sections, gully walls, river or road cuts etc.) are usually significantly drier than corresponding material a few metres deeper into the section. In the worst case, where no further constraints can be placed on water content history, the mid-point between field and saturated water content can be chosen, and an estimate of uncertainty adopted, equal to 25% of the range. Then all possible values are covered by ±2 times the uncertainty. For example, a measured water content of, say, 9% (cf. saturation water content of 21%) would give a mean lifetime water content of 15±3% by weight, implying an overall contribution to the uncertainty on the age of ~3%[298]. This is not large compared to the expected minimum uncertainty of ~5% (uncertainties added in quadrature, see **Table 7**), and so is not of major concern. Similar arguments can be used to constrain the effects of the infilling of porosity by carbonate.

The water content of a ceramic buried in a sediment is more complicated. The porosity of a ceramic will differ from that of the sediment matrix, but it is readily measured by simply saturating the ceramic in water, weighing, drying and weighing again. Then it is assumed that the fraction of saturation that applies to the sediment matrix also applies to the ceramic[17]. The lifetime average water content estimated for the matrix is applied to the γ dose rate, and that for the ceramic to the beta dose rate.

---

[a]The age calculation spreadsheet attached to this paper allows the testing of the sensitivity of the ages to various parameters.

[b]A saturation water content can be measured for sand by adding sediment and excess water to say, a pre-weighed 100 ml syringe and applying pressure to remove the excess water. The point at which the syringe plunger stops moving is well-defined, and increasing the pressure does not extrude more water. The syringe and wet sand are weighed to obtain the saturated weight, and then placed in an oven and dried to obtain the dry weight: the ratio of the weight loss of the saturated sample during drying to the dry weight is the saturation water content.

1335

[bH1] Box 2: The Single Aliquot Regenerative (SAR) dose procedure

Assuming first order filling of an electron trap during irradiation, the subsequent luminescence signal can then be expressed as (based on[63]):

$$L(D) = S_j.\chi(D).N_0.\left(1 - e^{-b.D}\right) \quad \text{.....(4)}$$

where L is the number of luminescence photons, S and χ describe the dependence of luminescence sensitivity (here photons per recombining electron) on measurement number, j, and dose, D, respectively, N_0 is an upper limit to the number of trapped electrons (determined by the trap density), and b is a constant describing the rate of filling of the electron trap per unit dose. If the OSL trap is fully emptied during measurement, then $T(D_T)$, the response to a subsequent test dose D_T can be written as:

$$T(D_T) = S_{j+1}.\chi(D_T).N_0.(1 - e^{-b.D_T})$$

Thus, if D_T is now fixed

$$\frac{L(D)}{T} = \frac{S_j}{S_{j+1}}.K.\chi(D).(1 - e^{-b.D}) \quad \text{.....(5)}$$

where $K = 1/(\chi(D_T).\left(1 - e^{-b.D_T}\right))$ is a constant. Equation 5 represents the luminescence response to dosing and measurement in any one SAR cycle. If the ratio S_j/S_{j+1} is constant, the sensitivity-corrected luminescence signal *(L/T)* is independent of SAR cycle, and for any given dose, D, takes on a unique value. This result has been confirmed by numerical simulations using a more complex model that takes into account competing electron trapping and recombination processes[81], and by experiment (**Fig. 5a**).

In practice, the sensitivity-corrected luminescence from the 'i'th SAR cycle is usually identified as L_i/T_i. The first SAR cycle is denoted by i=0 because it is different from all later cycles, in that the dose, D_0, was absorbed before any subsequent laboratory pretreatment such as preheating. If D_0 was absorbed in nature, then it is often referred to as D_n (the measured value of D_n is D_e). In all later cycles (i=1, k), the aliquot has been preheated and light exposed before absorbing a dose D_i. Note also that this formulation assumes that the probability of trapping electrons in this system does not change with repeated dosing and emptying (b is independent of j and i), and does not change from natural irradiation to laboratory irradiation, assumptions fundamental to any added or regenerated dose procedure.

Although it is the exponentially saturating population of the electron trap (Equation 4) that records the chronometric information, it is important to realise that the resulting sensitivity-corrected luminescence response curve (Equation 5) does not mirror the growth of the electron trap population. The luminescence response curve may not be a simple saturating exponential and thus may not plateau at high doses; it can continue to increase, or even decrease, with dose, all depending on the behaviour of $\chi(D)$.

[bH3] Box 3: Testing for quartz purity

SAR dose measurements are most successful if the quartz OSL is dominated by the fast-component. One important step in ensuring this is to remove any other minerals likely to give luminescence. In practice, this means ensuring that all feldspar has been successfully separated in the sample preparation steps described above. Unfortunately, the chemical pretreatment intended to remove feldspar contamination is not always completely successful[299, 300]. The reasons for this are unclear, but presumably involve occluded feldspar grains, or feldspathic-like impurities within individual quartz grains. Feldspar impurities is a problem because feldspar is sensitive to the wavelengths used to stimulate quartz (usually 450 to 530 nm), and so can contaminate the quartz OSL signal. Luminescence from feldspar impurities is also significantly unstable, and much more difficult to bleach. If additional etching with HF does not remove residual signal contamination, then instrumental separation must be considered. For stimulation with blue or green wavelengths, the decay rate of the feldspar signal is considerably slower than that of the quartz fast-component, and so the use of the early background subtraction approach reduces the importance of any feldspar contamination. But feldspar, in contrast to quartz[59], is sensitive to infrared (IR) stimulation. This characteristic can be used to test for, and to reduce, contamination of the quartz OSL by feldspar OSL; this is done by inserting an IR stimulation immediately prior to the measurement of L_i (but not T_i) in an additional recycling ratio test[93]. If the resulting $(L_i/T_i)/(L_1/T_1)$ recycling ratio (often referred to as the *OSL IR depletion ratio* in the literature) is indistinguishable from unity, then feldspar OSL does not contribute significantly to the quartz signal. In samples where the feldspar contamination remains of significance even after additional etching with HF, it can be reduced by inserting the IR stimulation step in front of every L and T measurement[301], although such a 'double SAR' approach is expensive in measurement time. There are also other instrumental methods for minimising any feldspar contribution, but these are not in routine use[40, 302].

Tables

Table 1 Synthesis of different dating applications and events that can be constrained using quartz OSL. Columns 4-5 indicate the general suitability of OSL dating in different geological settings and key practical consideration that can influence OSL dating reliability. (Suitability classification: O = Optimal; R = routine with appropriate methodological considerations; S = sub-optimal; C = challenging; N = not recommended; Nv = novel or not widely used)

Application type	Event being dated	Signal resetting agent	Suitability and age interpretation	Practical considerations
Aeolian (wind-transported)	Formation of desert and coastal dunes[83, 146, 161, 261, 303-311]	Daylight	O; direct dating	Usually well-reset by sub-aerial exposure. Dune fields reflect transitional climates from arid to humid to allow sand movement and subsequent trapping. OSL dates last movement, and can be used to derive dune aggradation and migration rates and desert albedo changes. Bioturbation and pedogenesis processes can affect low-cohesion, near-surface dune deposits. Significant beta-dose heterogeneity possible in low radioactivity dune deposits and/or coarse grained sand dunes. Does not significantly affect average behaviour. Dating of gypsum dunes by targeting embedded quartz grains.
	Loess accumulation[95, 99, 104, 148, 312-321]	Daylight	O; direct dating	Fine-grain deposits with limited sand-sized quartz. Coarse silt can be used, but feldspar contamination may be difficult to remove.

Fluvial, alluvial, beach (high-energy water transport)	Terrace deposition and abandonment[106, 269, 322-324]	Daylight	R-C; direct dating of fluvial deposition; indirect dating of floodplain abandonment	In all cases, both sub-aerial and sub-aqueous daylight exposure likely for fluvial sediment transported downstream through many reworking cycles, with intervening periods of direct daylight exposure during low flow. Thus well-sorted distinct sand lenses/layers derived from low energy, shallow water environments are most likely to be well-bleached; they also provide a simplified dosimetry.
	Channel migration[325, 326]	Daylight	R-C; direct dating of channel deposition; indirect dating of channel erosion	
	Channel cutting and filling; floodplain aggradation and alluvial fan formation[327]	Daylight	R-C; direct dating of filling events, indirect dating of cutting or incision events	
	Palaeoflood deposits[211, 212, 328]	Daylight	R-C: direct dating of flood events	Bleaching during flood unlikely, but prior bleaching of sediments before flood entrainment seems common.
	Beach formation associated with sea level changes[217, 293, 329-331]	Daylight	O-C; direct dating	Usually well reset by sub-aerial and sub-aqueous bleaching. High carbonate contents common in low-latitude beach deposits, may lead to complexity (time-dependent dose rates) if carbonate content changes with time.
	Tsunami deposits[332-334]	Daylight	S-N; direct dating	Bleaching unlikely during event but sediments entrained in shallow water likely already well-bleached.
Lacustrine and offshore-marine	Lake level variations[335-340]	Daylight	S-C; direct dating of lake full phases (sedimentation);	Sampling by coring usually precludes *in situ* γ dose rate measurement. Organic-rich, low-energy lakes may have limited coarse-grain quartz yields. Time-dependent dose rates can arise from both U-series

(low-energy water transport)			indirect dating of lake drying phases (non-deposition)	disequilibria and sediment compaction/dewatering associated with accumulation of overburden (especially true for gyttja).
	Formation of lake-margin deposits (deltas, lake shoreline features)[143, 151, 152, 341-343]	Daylight	R; direct dating	Used to date lake high stands. Marginal deposits may be more accessible and suitable than lake bed deposits (in terms of grain size, bleaching history). Sub-aerial and sub-aqueous bleaching likely for beach deposits.
	Ocean floor sedimentation[5, 13, 14, 144, 344, 345]	Daylight	R-C; direct dating	Bleaching sub-aerial (dust) or sub-aqueous (fluvial input). Time-dependent dose rates due to U-series disequilibria may increase complexity, especially in the presence of high carbonate content. High water content reduces dose rate and extends age range. Usually very low coarse-grained quartz content.
Glacigenic (ice-related)	Moraine / till formation[157, 346-348]	Daylight	R–C; direct dating of ice margin	For all glacial sediments, low OSL signal sensitivity is common in primary ice-eroded material. Limited/no daylight exposure possible. If sediment unexposed to daylight during the last transport, the OSL age will relate to an earlier transport event, but dose rate may have changed.
	Proglacial outwash plain activation[157, 159, 349, 350]	Daylight	R; direct dating of outwash plain; indirect dating of ice margin	Transport distance from ice-margin important for bleaching.

	Glaciofluvial channel activation[150, 351, 352]	Daylight	R; direct dating of channel activation; indirect dating of ice margin	Event-related activation may lead to limited daylight exposure.
	Glaciolacustrine sedimentation[353]	Daylight	R–S; direct dating of proglacial lake sedimentation.	Sediment deposited in ice-marginal turbid lakes may experience little/no daylight exposure; OSL age may therefore reflect previous transport events.
	Glacioaeolian deposition[163, 209, 354-356]	Daylight	O; indirect dating of (peri)-glacial processes	See "sand dune formation" and "loess accumulation" above.
Colluvium, solifluction sheets, debris flows (gravitational mass movements)	Slope failures, formation and progradation[357-360]	Daylight	SR-C; direct dating	Limited transport distances and/or daylight exposure durations can increase the likelihood for heterogeneous bleaching. Poorly sorted deposits may suffer from spatially heterogeneous radiation fields.
Archaeology, palaeontology, palaeoanthropology (including karst deposits)	Site depositional history[97, 105-107, 193, 194, 198, 202, 361-363]	Daylight	O-R; direct dating	Covers a wide-range of depositional contexts (see above for details). Open-air archaeological sites have better bleaching conditions and fewer post-depositional complexities than caves and rock shelters. Complexity from syn-depositional mixing and contamination by older generations of pre-existing deposits may arise in cave settings.
	Internment of autochthonous fossils / cultural materials in sediments[201, 207, 208, 210, 364]	Daylight	O-R; indirect dating but close association with dating event	Multiple cycles of human occupation may cause post-depositional disturbance (digging, burials, fire pits).

	Internment of allochthonous fossils / cultural materials in sediments[230, 365]	Daylight	O-R; indirect dating and poor association with dating event	OSL provides minimum age for fossils and archaeological material. Animal disturbance of host sediments is possible in dens and pitfall traps.
	In situ production of cultural materials, including debitage production[97, 135, 136, 366]	Heat (lithics, fireplaces) Daylight	R, C, Nv; direct dating	Stones (fireplace, pot-boilers) usually straightforward if heated sufficiently to fully reset. Heated lithics with no stratigraphic context (museum specimens) will have poorly constrained γ dose rates.
	Heating of pottery, bricks, tiles. Manufacturing of mortars[131, 132, 367-370]	Heat, Daylight (mortars)	O; direct	Straightforward but extraction of sufficient coarse quartz may not always be possible in pottery. Surrounding sediment/brick should be collected for γ dose rate estimation
Soil and regolith processes	Formation of soil A horizons[125, 169, 172]	Daylight	C, Nv; direct dating	Bleaching by turbation ongoing until soil surface buried. Age usually reflects time of burial. Old soils well-bleached, young soils usually incompletely bleached. Scatter in D_e can be interpreted in terms of turbation rates.
	Sediment mixing between layers[170, 240, 371]	Daylight	C-N; direct dating	Single-grain studies may provide insight into grain movement histories. Reliable dating not usually possible, but identification of mixing may be possible.
	Soil creep rates[168, 372]	Daylight	C, Nv; direct dating	Reliable interpretation of apparent ages challenging.
	Formation of pedogenic and biogenic structures (carbonate nodules, termite mounds, root casts)[171, 173]	Daylight	C-N, Nv; direct dating	Careful sampling important to isolate individual formation events. Problems of interpretation similar to those for soil creep rates. Carbonate-rich structures may involve time-dependent dose rates.

Neo-tectonics and volcanic histories	Occurrence of palaeo-earthquakes[164-167, 373-375]	Daylight before/after seismic events	R-C; indirect dating of seismic event itself but close stratigraphic association	Sediments associated with palaeo-earthquakes often experienced limited transport (and so daylight exposure), particularly colluvium, debris flows or locally intruded deposits. Targeting stable palaeo-surfaces can improve dating reliability.
	Offset of geomorphic surfaces due to fault movement[376-381]	Daylight before and after faulting event	R-C; indirect dating of faulting event itself but close stratigraphic association	Limited transport distances and daylight exposure if sampling fluvial, colluvium, debris flows or locally intruded deposits. Rock surface dating may be applicable.
	Dating fault gouge and dike intrusions[138]	Frictional heating	R-C; direct dating of faulting or seismic event	Sand-sized quartz grains may not be present in gouge. Gouge may be very thin, making sampling challenging
	Volcanic eruptions – dating proximaldeposits[382-384]	Heating by magma	R-C; indirect dating of volcanic event itself but close stratigraphic association	Quartz from volcanic sources usually insensitive, weak fast-component. But quartz from contact-heated sediments likely to have improved OSL sensitivity.
	Volcanic eruptions – dating distal deposits [104, 351, 354, 364, 385, 386]	Daylight	R-C; indirect dating of volcanic event itself but close stratigraphic association	Sampling above and below discrete tephra horizons constrains ash fall events. Sampling of deposits that host cryptotephra is also possible.
Burial dating of rock surfaces	Construction of megaliths, cairns, stone walls, etc. Dating erratics,	Daylight	R-C, Nv; direct dating	Only likely applicable to sandstones and some quartzite clasts because of poor quartz OSL sensitivity in primary rocks (e.g. granites).

	scree slopes, rockfalls, cobble beaches and beach ridges[187, 188, 284]			
Exposure dating of rock surfaces	Construction of megaliths, cairns, stone walls, etc. Rock art dating. Dating erratics, scree slopes, rockfalls, cobble beaches and beach ridges [15, 187, 287]	Daylight	C, Nv; direct dating	Known-age exposure samples needed for calibration. Only likely applicable to sandstones and some quartzite clasts because of poor quartz OSL sensitivity in primary rocks (e.g. granites).
Thermochronometry	Bedrock exhumation[387, 388]	Cooling below closure temperatures of 30-40^{o}C	C, Nv; direct dating	Signal saturation restricts applications to rapidly exhumed settings or elevated temperature settings. Combination of quartz OSL with other signals (TL, IRSL, post-IR IRSL) may offer more versatility. Only likely applicable to sandstones and some quartzite clasts because of poor quartz OSL sensitivity in primary rocks (e.g. granites).
Palaeo-lightning events	Fulgurite formation [141]	Heating of trapped quartz grains	O-R, Nv; direct dating	Target quartz grains occluded in the fused matrix.

Table 2. Example tables containing suggested minimum sample-specific information that should be presented in a publication containing quartz OSL luminescence ages. All uncertainties expressed at 1σ confidence level and contain both random and systematic components. More general characteristics (especially dose recovery) are also required to assess reliability, and can be summarised in associated text.

a)

Lab.code	^{238}U, Bq.kg^{-1}	^{226}Ra, Bq.kg^{-1}	^{232}Th, Bq.kg^{-1}	^{40}K, Bq.kg^{-1}	*beta dose rate, Gy.ka^{-1}	* γ dose rate, Gy.ka^{-1}
1	51 ± 12	46.0 ± 1.2	61.0 ± 1.2	562 ± 20	2.29 ± 0.06	1.48 ± 0.04
2	72 ± 12	48.2 ± 1.1	60.6 ± 1.2	566 ± 16	2.32 ± 0.05	1.50 ± 0.04
3	58 ± 9	45.2 ± 0.9	60.2 ± 1.0	581 ± 13	2.33 ± 0.05	1.48 ± 0.04
4	46 ± 8	43.8 ± 0.8	32.2 ± 0.8	158 ± 8	1.05 ± 0.04	0.81 ± 0.04

Note: * dry infinite matrix dose rates

b)

Lab.code	Site	Depth, cm	w.c. %	OSL D_e, Gy	(n_r)	(n_a)	Total dose rate, Gy/ka	OSL age, ka
1	Test site-A	65	16	95 ± 4	1	23	3.16 ± 0.16	30.0 ± 2.0
2	Test site-B	65	16	73 ± 4	0	12	3.19 ± 0.16	22.9 ± 1.7
3	Test site-C	65	16	107 ± 6	0	24	3.20 ± 0.16	33.5 ± 2.5
4	Test site-C	30	11	43 ± 2	1	35	1.79 ± 0.09	23.9 ± 1.7

Note: (a) Mean grain size 215μm. (b) Site altitude 0 km. (c) w.c.: water content. (d) n_r, n_a : number of rejected and accepted aliquots, respectively.

References

1. Noller, J.S.S., J.M.: Lettis, W.R.;. Quaternary Geochronology: Methods and Applications (American Geophysical Union, 2013).
2. Wintle, A. & Huntley, D. Thermoluminescence dating of a deep-sea sediment core. *Nature* **279**, 710-712 (1979).
3. Huntley, D.J., Godfrey-Smith, D.I. & Thewalt, M.L.W. Optical dating of sediments. *Nature* **313**, 105-107 (1985).
4. Qiu, F.Y. & Zhou, L.P. A new luminescence chronology for the Mangshan loess-palaeosol sequence on the southern bank of the Yellow River in Henan, central China. . *Quaternary Geochronology* **30**, 24-33 (2015).
5. Sugisaki, S. et al. High resolution optically stimulated luminescence dating of a sediment core from the southwestern Sea of Okhotsk. *Geochemistry, Geophysics, Geosystems* **13** (2012).
6. Buylaert, J.-P. et al. A robust feldspar luminescence dating method for Middle and Late Pleistocene sediments. *Boreas* **41**, 435-451 (2012).
7. Jain, M. Extending the dose range: Probing deep traps in quartz with 3.06 eV photons. *Radiation Measurements* **44**, 445–452 (2009).
8. Hütt, G., Jaek, I. & Tchonka, J. Optical dating: K-feldspars optical response stimulation spectra. *Quaternary Science Reviews* **7**, 381–385 (1988).
9. Sohbati, R., Murray, A.S., Lindvold, L., Buylaert, J.-P. & Jain, M. Optimization of laboratory illumination in optical dating. *Quaternary Geochronology* **39**, 105-111 (2017).
10. Nelson, M.S.G., H.J.; Johnson, J.A.; Rittenour, T.M.; Feathers, J.K.; Mahan, S.A. User guide for luminescence sampling in archaeological and geological contexts. *Advances in Archaeological Practice* **3**, 166-177 (2015).
11. Rajapara, H.M., Kumar, V., Chauhan, N., Gajjar, P.N. & Singhvi, A.K. Bleaching of blue light stimulated luminescence of quartz by moonlight. *Journal of Earth System Science* **129**, 1-7 (2020).
12. Chen, Y.W.C., Y.G.; Murray A.S.;Liu, T.K.;Lai, T.C.;. Luminescence dating of neotectonic activity on the southwestern coastal plain, Taiwan. *Quaternary Science Reviews* **22**, 1223-1229 (2003).
13. Sugisaki, S. et al. High resolution OSL dating back to MIS 5e in the central Sea of Okhotsk. *Quaternary Geochronology* **5**, 293-298 (2010).
14. Armitage, S.J. & Pinder, R.C. Testing the applicability of optically stimulated luminescence dating to Ocean Drilling Program cores. *Quaternary Geochronology* **39**, 124-130 (2017).
15. Gliganic, L.A., Meyer, M.C., Sohbati, R., Jain, M. & Barret, S. OSL surface exposure dating of a lithic quarry in Tibet: Laboratory validation and application. *Quaternary Geochronology* **49**, 199-204 (2019).
16. Prescott, J.R. & Hutton, J.T. Cosmic ray contributions to dose rates for luminescence and ESR dating: large depths and long-term time variations. *Radiation Measurements* **23**, 497–500 (1994).
17. Aitken, M.J. Thermoluminescence Dating (Academic Press, London, 1985).
18. Li, B.J., Z.; Roberts, R. G.; Li, S. . Review and assessment of the potential of post-IR IRSL dating methods to circumvent the problem of anomalous fading in feldspar luminescence. *Geochronometria* **41**, 178-201 (2014).
19. Porat, N., Faerstein, G., Medialdea, A. & Murray, A.S. Re-examination of common extraction and purification methods of quartz and. *Ancient TL* **33**, 22-30 (2015).
20. Chu, S.Y.F., Ekström, L.P. & Firestone, R.B. http://nucleardata.nuclear.lu.se/toi/ (1999).
21. Ivanovich, M. & Harmon, R.S. Uranium-series disequilibrium: applications to earth, marine, and environmental sciences. 2. ed. (Clarendon Press, Oxford, 1992).
22. Roesch, W.C. & Attix, F.H. in Attix, F.H., Roesch, W.C. (Eds.). Radiation Dosimetry. Volume I: Fundamentals (Academic Press, New York and London, 1968).
23. Bourdon, B., Henderson, G.M., Lundstrom, C.C. & Turner, S.P. (eds) Uranium-series Geochemistry, pp. 656 (Mineralogical Society of America, Washington, D.C., 2003).

24. Bøtter-Jensen, L., Agersnap Larsen, N., Markey, B.G. & McKeever, S.W.S. Al2O3:C as a sensitive OSL dosemeter for rapid assessment of environmental photon dose rates. *Radiation Measurements* **27**, 295-298 (1997).
25. Richter, D., Dombrowski, H., Neumaier, S., Guibert, P. & Zink, A.C. Environmental gamma dosimetry with OSL of α-Al2O3: C for in situ sediment measurements. *Radiation protection dosimetry*, **141**, 27-35 (2010).
26. Kreutzer, S. et al. Environmental dose rate determination using a passive dosimeter: techniques and workflow for α-Al2O3: C chips. *Geochronometria* **45**, 56-67 (2019).
27. Miallier, D., Guérin, G., Mercier, N., Pilleyre, T. & Sanzelle, S. The Clermont radiometric reference rocks: a convenient tool for dosimetric purposes. *Ancient TL* **20**, 37-43 (2009).
28. Arnold, L.J., Duval, M., Falguères, C., Bahain, J.-J. & Demuro, M. Portable gamma spectrometry with cerium-doped lanthanum bromide scintillators: Suitability assessments for luminescence and electron spin resonance dating applications. *Radiation Measurements* **6-18**, 47 (2012).
29. Løvborg, L. & Kirkegaard, P. Response of 3" x 3" NaI(Tl) detectors to terrestrial gamma radiation. *Nuclear Instruments and Methods* **121**, 239-251 (1974).
30. Guérin, G. & Mercier, N. Determining gamma dose rates by field gamma spectroscopy in sedimentary media: results of Monte Carlo simulations. *Radiation Measurements*, **46**, 190-195 (2011).
31. Spooner, N.A. The optical dating signal from quartz. *Radiation Measurements* **23**, 593-600 (1994).
32. Bøtter-Jensen, L., Thomsen, K.J. & Jain, M. Review of optically stimulated luminescence (OSL) instrumental developments for retrospective dosimetry. *Rad. Meas* **45**, 253–257 (2010).
33. Clark-Balzan, L. & Schwenninger, J. First steps toward spatially resolved OSL dating with electron multiplying charge-coupled devices (EMCCDs): system design and image analysis. *Radiation Measurements* **47**, 797–802 (2012).
34. Richter, D., Richter, A. & Dornich, K. Lexsyg – a new instrument for luminescence research. *Geochronometria* **40**, 220–228 (2013).
35. Thomsen, K.J., Kook, M., Murray, A.S., Jain, M. & Lapp, T. Single-grain results from an EMCCD-based imaging system. *Radiation Measurements* **81**, 185–191 (2015).
36. Bøtter-Jensen, L. & Duller, G.A.T. A new system for measuring OSL from quartz samples. *Nucl. Tracks. Radiat. Meas* **20**, 549–553 (1992).
37. Bulur, E., Bøtter-Jensen, L. & Murray, A.S. Optically stimulated luminescence from quartz measured using linear modulation technique. *Radiation Measurements* **32**, 407-411 (2000).
38. Huntley, D.J., Short, M.A. & Dunphy, K. Deep traps in quartz and their use for optical dating. *Can. J. Phys* **74**, 81–91 (1996).
39. Bulur, E. An alternative technique for optically stimulated luminescence (OSL) experiment. *Radiat. Meas* **26**, 701–709 (1996).
40. Thomsen, K.J. et al. Minimizing feldspar OSL contamination in quartz UV-OSL using pulsed blue stimulation. *Radiation Measurements* **43**, 752–757 (2008).
41. Ankjærgaard, C. & Jain, M. Optically stimulated phosphorescence in quartz over the millisecond to second time scale: insights into the role of shallow traps in delaying luminescent recombination. *Journal of Physics D: Applied Physics* **43**, 255502 (2010).
42. Huntley, D.J., Godfrey-Smith, D.I. & Thewalt, M.L.W. Optically dating of sediments. *Nature* **313**, 105–107 (1985).
43. Duller, G.A.T., Bøtter-Jensen, L., Murray, A.S. & Truscott, A.J. Single grain laser luminescence (SGLL) measurement using a novel automated reader. *Nuclear Instruments and Methods B* **155**, 506–514 (1999).
44. Bøtter-Jensen, L., Bulur, E., Duller, G.A.T. & Murray, A.S. Advances in luminescence instrument systems. *Radiation Measurements* **32**, 523–528 (2000).
45. Bøtter-Jensen, L., Duller, G.A.T., Murray, A.S. & Banerjee, D. Blue light emitting diodes for optical stimulation of quartz in retrospective dosimetry and dating. *Radiation Protection Dosimetry* **84**, 335–340 (1999).

46. Duller, G.A.T., Bøtter-Jensen, L. & Murray, A.S. Combining infrared- and green-laser stimulation sources in single-grain luminescence measurements of feldspar and quartz. *Radiation Measurements* **37**, 543–550 (2003).
47. Hansen, V., Murray, A., Buylaert, J.P., Yeo, E.Y. & Thomsen, K. A new irradiated quartz for beta source calibration. *Radiation Measurements* **81**, 123-127 (2015).
48. Thomsen, K.J., Murray, A.S. & Bøtter-Jensen, L. Sources of variability in OSL dose measurements using single grains of quartz. *Radiation Measurements* **39**, 47–61 (2005).
49. Ankjærgaard, C. & Murray, A.S. Total beta and gamma dose rates in trapped charge dating based on beta counting. *Radiation Measurements* **42**, 352-359 (2007).
50. Vandenberghe, D., De Corte, F., Buylaert, J.-P. & Kučera, J. On the internal radioactivity in quartz. *Radiation Measurements* **43**, 771-775 (2008).
51. Guérin, G., Mercier, N. & Adamiec, G. Dose-rate conversion factors: update. *Ancient TL* **29**, 5-8 (2011).
52. Guérin, G., Mercier, N., Nathan, R., Adamiec, G. & Lefrais, Y. On the use of the infinite matrix assumption and associated concepts: a critical review. *Radiation Measurements* **47**, 778-785 (2012).
53. Guérin, G., Jain, M., Thomsen, K.J., Murray, A.S. & Mercier, N. Modelling dose rate to single grains of quartz in well-sorted sand samples: The dispersion arising from the presence of potassium feldspars and implications for single grain OSL dating. *Quaternary Geochronology* **27**, 52-65 (2015).
54. Mayya, R.M., Morthekai, P., Murari, M.K. & Singhvi, A.K. Towards quantifying beta microdosimetric effects in single grain quartz dose distribution. *Radiation Measurements* **41**, 1032–1039 (2006).
55. Guibert, P., Lahaye, C. & Bechtel, F. The importance of U-series disequilibrium of sediments in luminescence dating: a case study at the Roc de Marsal cave (Dordogne, France). *Radiation Measurements* **44**, 223-231 (2009).
56. Jain, M., Choi, J.H. & Thomas, P.J. The ultrafast OSL component in quartz: Origins and implications. *Radiation Measurements* **43**, 709-714 (2008).
57. Wintle, A.G. & Murray, A.S. The relationship between quartz TL, PTTL and OSL. *Radiation Measurements* **27**, 611–624 (1997).
58. Jain, M., Murray, A.S., Bøtter-Jensen, L. & Wintle, A.G. A single-aliquot regenerative-dose method based on IR (1.49 eV) bleaching of the fast OSL component in quartz. *Radiation Measurements* **39**, 309-318 (2005).
59. Jain, M., Murray, A.S. & Bøtter-Jensen, L. Characterisation of blue-light stimulated luminescence components in different quartz samples: implications for dose measurement. *Radiation Measurements* **37**, 441–449 (2003).
60. Murray, A.S. & Wintle, A.G. Isothermal decay of optically stimulated luminescence in quartz. *Radiation Measurements* **30**, 119–125 (1999).
61. Bøtter-Jensen, L. et al. Luminescence sensitivity changes in quartz as a result of annealing. *Radiation Measurements* **24**, 535-541 (1995).
62. Wintle, A.G. & Murray, A.S. Quartz OSL: effects of thermal treatment and their relevance to laboratory dating procedures. *Radiation Measurements* **32**, 387–400 (2000).
63. Moska, P. & Murray, A.S. Stability of the quartz fast-component in insensitive samples. *Radiation Measurements* **41**, 878-885 (2006).
64. Buylaert, J.P. et al. Luminescence dating of old (>70 ka) Chinese loess: A comparison of single-aliquot OSL and IRSL techniques. *Quaternary Geochronology* **2**, 9-14 (2007).
65. Chapot, M., Roberts, H.M., Duller, G.A. & Lai, Z.P. A comparison of natural- and laboratory-generated dose response curves for quartz optically stimulated luminescence signals from Chinese Loess. *Radiation Measurements* **47**, 1045-1052 (2012).
66. Lowick, S.E., Preusser, F. & Wintle, A.G. Investigating quartz optically stimulated luminescence dose–response curves at high doses. *Radiation Measurements* **45**, 975-984 (2010).
67. Ellerton, D. et al. An 800 kyr record of dune emplacement in relationship to high sea level. *Geomorphology* **354**, 106999 (2020).

68. Pawley, S.M., Bailey, R.M., Rose, J., Moorlock, B.S.P. & Hamblin, R.J.O. Age limits on Middle Pleistocene glacial sediments from OSL dating, north Norfolk, UK. *Quaternary Science reviews* **27**, 1363-1377 (2008).
69. Beerten, K.V., K. et al. Electron spin resonance (ESR), optically stimulated luminescence (OSL) and terrestrial cosmogenic radionuclide (TCN) dating of quartz from a Plio-Pleistocene sandy formation in the Campine area, NE Belgium. *Quaternary International* **556**, 144-158 (2020).
70. Madsen, A.T., Duller, G.A.T., Donnelly, J.P., Roberts, H.M. & Wintle, A.G. A chronology of hurricane landfalls at Little Sippewisset Marsh, Massachusetts, USA, using optical dating. *Geomorphology* **109**, 36-45 (2009).
71. Durcan, J.A. & Duller, G.A.T. The fast ratio: A rapid measure for testing the dominance of the fast component in the initial OSL signal from quartz. *Radiation Measurements* **46**, 1965-1072 (2011).
72. Ankjærgaard, C., Jain, M., Hansen, P.C. & Nielsen, H.B. Towards multi-exponential analysis in optically stimulated luminescence. *Journal of Physics D: Applied Physics* **43**, 195501 (2010).
73. Bailey, R.M., Yukihara, E.G. & McKeever, S.W.S. Separation of quartz optically stimulated luminescence components using green (525 nm) stimulation. *Radiation Measurements* **46**, 643-648 (2011).
74. Ballarini, M., Wallinga, J., Wintle, A. G. & Bos, A. J. J. A modified SAR protocol for optical dating of individual grains from young quartz samples. *Radiation Measurements*, 360-369 (2007).
75. Cunningham, A. & Wallinga, J. Selection of integration time intervals for quartz OSL decay curves. *Quaternary Geochronology* **5**, 657-666 (2010).
76. Duller, G.A.T., Bøtter-Jensen, L. & Murray, A.S. Optical dating of single sand-sized grains of quartz: sources of variability. *Radiation Measurements* **32**, 453-457 (2000).
77. Guérin, G. et al. Absorbed dose, equivalent dose, measured dose rates, and implications for OSL age estimates: Introducing the Average Dose Model. *Quaternary Geochronology* **41**, 163-173 (2017).
78. Murray, A.S. & Wintle, A.G. Luminescence dating of quartz using an improved single-aliquot regenerative-dose protocol. *Radiation Measurements* **32**, 57–73 (2000).
79. Murray, A.S., Roberts, R.G. & Wintle, A.G. Equivalent dose measurement using a single aliquot of quartz. *Radiation Measurements* **27**, 171-184 (1997).
80. Huntley, D.J. Note: some notes on language. *Ancient TL* **19**, 27-28 (2001).
81. Bailey, R.M. Towards a general kinetic model for optically and thermally stimulated luminescence of quartz. *Radiation Measurements* **33**, 17-45 (2001).
82. Murray, A.S. & Wintle, A.G. The single aliquot regenerative dose protocol: potential for improvements in reliability. *Radiation Measurements* **37**, 377–381 (2003).
83. Madsen, A.T., Murray, A.S. & Andersen, T.J. Optical dating of dune ridges on Rømø, a barrier island in the Wadden Sea, Denmark. *Journal of Coastal Research* **23**, 1259–1269 (2007).
84. Godfrey-Smith, D.I. Thermal effects in the optically stimulated luminescence of quartz and mixed feldspars from sediments. *Journal of Physics D: applied Physics* **27**, 1737-1746 (1994).
85. Wintle, A.G.M., A.S. Luminescence sensitivity changes in quartz. *Radiation Measurements* **30**, 107.118 (1999).
86. Smith, B.W. & Rhodes, E.J. Charge movements in quartz and their relevance to optical dating. *Radiation Measurements* **23**, 329-333 (1994).
87. Ankjærgaard, C., Murray, A.S. & Denby, P.M. Thermal pre-treatment (preheat) in the OSL dating of quartz: is it necessary? *Radiation Protection Dosimetry* **119**, 470–473 (2006).
88. Rhodes, E.J. Observations of thermal transfer OSL signals in glacigenic quartz. *Radiation Measurements* **32**, 595-602 (2000).
89. Madsen, A.T., Murray, A.S., Andersen, T.J., Pejrup, M. & Breuning-Madsen, H. Optically stimulated luminescence dating of young estuarine sediments: a comparison with 210Pb and 137Cs dating. *Marine Geology* **214**, 251–268 (2005).

90. Murray, A.S. Developments in optically transferred luminescence and photo-transferred thermoluminescence dating: application to a 2000-year sequence of flood deposits. *Geochimica et Cosmochimica Acta* **60**, 565–576 (1996).
91. Singh, A. et al. Counter-intuitive influence of Himalayan river morphodynamics on Indus Civilisation urban settlements. *Nature Communications* **8**, 1–14 (2017).
92. Guérin, G.C., B.; Lahaye, C.; Thomsen, K. J.; Tribolo, C.; Urbanova, P.; Guibert, P.; Mercier, N.; Valladas, H.;. Testing the accuracy of a single grain OSL Bayesian central dose model with known-age samples. *Radiation Measurements* **81**, 62-70 (2015).
93. Duller, G.A.T. Distinguishing quartz and feldspar in single grain luminescence measurements. *Radiation Measurements* **37**, 161-165 (2003).
94. Thomsen, K.J. et al. Testing single-grain quartz OSL methods using sediment samples with independent age control from the Bordes-Fitte rockshelter (Roches d'Abilly site, Central France. *Quaternary Geochronology* **31**, 77–96 (2016).
95. Stevens, T. et al. Ice-volume-forced erosion of the Chinese Loess Plateau global Quaternary stratotype site. *Nature Communications* **9**, 983–983 (2018).
96. Vandenberghe, D. et al. Exploring the method of optical dating and comparison of optical and 14C ages of Late Weichselian coversands in the southern Netherlands. *Journal of Quaternary Science* **19**, 73-86 (2004).
97. Guérin, G. et al. The complementarity of luminescence dating methods illustrated on the Mousterian sequence of the Roc de Marsal: A series of reindeer-dominated, Quina Mousterian Layers dated to MIS 3. *Quaternary International* **433**, 102-115 (2017).
98. Nielsen, A., Murray, A.S., Pejrup, M. & Elberling, B. Optically stimulated luminescence dating of a Holocene beach ridge plain in Northern Jutland, Denmark. *Quaternary Geochronology* **1**, 305-312 (2006).
99. Buylaert, J.P. et al. Optical dating of Chinese loess using sand-sized quartz: Establishing a time frame for Late Pleistocene climate changes in the western part of the Chinese Loess Plateau. *Quaternary Geochronology* **3**, 99-113 (2008).
100. Roberts, H.M. & Duller, G.A.T. Standardised growth curves for optical dating of sediment using multiple-grain aliquots. *Radiation Measurements* **38**, 241-252 (2004).
101. Duller, G.A.T. Improving the accuracy and precision of equivalent doses determined using the optically stimulated luminescence signal from single grains of quartz. *Radiation Measurements* **47**, 770-777 (2012).
102. Jacobs, Z., Roberts, R.G., Nespoulet, R., El Hajraoui, M.A. & Debénath, A. Single-grain OSL chronologies for Middle Palaeolithic deposits at El Mnasra and El Harhoura 2, Morocco: Implications forLate Pleistocene huma-environment interactions along the Atlantic coast of northwest Africa. *Journal of Human Evolution* **62**, 377-394 (2012).
103. Gliganic, L.A., Jacobs, Z. & Roberts, R.G. Luminescence characteristics and dose distributions. *Archaeological and Anthropological Science* **4**, 115-135 (2012).
104. Demuro, M., Arnold, L.E., Froese, D.G. & Roberts, R.G. OSL dating of loess deposits bracketing Sheep Creek tephra beds, northwest Canada: Dim and problematic single-grain OSL characteristics and their effect on multi-grain age estimates. *Quaternary Geochronology* **15**, 67-87 (2013).
105. Guérin, G. et al. A multi-method luminescence dating of the Palaeolithic sequence of La Ferrassie based on new excavations adjacent to the La Ferrassie 1 and 2 skeletons. *Journal of Archaeological Science* **58**, 147-166 (2015).
106. Arnold, L.J. et al. OSL dating of individual quartz 'supergrains' from the Ancient Middle Palaeolithic site of Cuesta de la Bajada, Spain. *Quaternary Geochronology* **36**, 78–101 (2016).
107. Demuro, M., Arnold, L.J., Aranburu, A., Gómez-Olivencia, A. & Arsuaga, J.L. Single-grain OSL dating of the Middle Palaeolithic site of Galería de las Estatuas, Atapuerca (Burgos, Spain). *Quaternary Geochronology* **49**, 138-145 (2019).
108. Murray, A.S. & Olley, J.M. Precision and accuracy in the optically stimulated luminescence dating of sedimentary quartz. *Geochronometria* **21**, 1–16 (2002).
109. Preusser, F. et al. Quartz as a natural luminescence dosimeter. *Earth-Science Reviews* **97**, 184-214 (2009).

110. Rhodes, E.J. Optically stimulated luminescence dating of sediments over the past 200,000 years. *Annual Review of Earth and Planetary Sciences* **39**, 461-488 (2011).
111. Madsen, A.T. & Murray, A.S. Optically stimulated luminescence dating of young sediments: a review. *Geomorphology* **109**, 3–16 (2009).
112. Wallinga, J. Optically stimulated luminescence dating of fluvial deposits: A review. *Boreas* **31**, 303-322 (2003).
113. Thrasher, I.M., Mauz, B., Chiverrell, R.C. & Lang, A. Luminescence dating of glaciofluvial deposits: A review. *Earth-Science Reviews* **97**, 133-146 (2009).
114. Jacobs, Z. & Roberts, R.G. Advances in optically stimulated luminescence dating of individual grains of quartz from archeological deposits. *Evolutionary Athropology* **16**, 210–223 (2007).
115. Fleming, S.J. The pre-dose technique: a new thermo-luminescent dating method. *Archaeometry* **15**, 13-30 (1973).
116. Wintle, A.G. Thermoluminescence dating of late Devensian loesses in Southern England. *Nature* **289**, 479-480 (1981).
117. Wintle, A.G., Li, S.H. & Botha, G.A. Luminescence dating of colluvial deposits from Natal, South Africa. *South African Journal of Science* **89**, 77-82 (1993).
118. Lang, A. Infra-red stimulated luminescence dating of holocene reworked silty sediments. *Quaternary Science Reviews* **13**, 525-528 (1994).
119. Chawla, S. & Singhvi, A.K. Thermoluminescence dating of Archaeological Sediments. *Naturwissenschaften* **76**, 416-419 (1989).
120. Owen, L.A. et al. Relic permafrost structures in the Gobi of Mongolia: Age and significance. *Journal of Quaternary Science* **13**, 539-547 (1998).
121. Balescu, S. & Lamothe, M. Comparison of TL and IRSL age estimates of feldspar coarse grains from waterlain sediments. *Quaternary Science Reviews* **13**, 437-444 (1994).
122. Edwards, S.R. Luminescence dating of sand from the Kelso Dunes, California. *The dynamics and environmental context of aeolian sedimentary systems*, 59-68 (1993).
123. Lamothe, M. & Huntley, D.J. Thermoluminescence dating of Late Pleistocene sediments, St. Lawrence Lowland, Quebec. *Geographie Physique et Quaternaire* **42**, 33-44 (1988).
124. Banerjee, D., Singhvi, A.K., Pande, K., Chandra, B.P. & Gogte, V. Towards a direct dating of fault gouges using luminescence dating techniques - methodological aspects. *Current Science* **77**, 256-268 (1999).
125. Singhvi, A.K., Bronger, A., Pant, R.K. & Sauer, W. Thermoluminescence dating and its implications for the chronostratigraphy of loess-paleosol sequences in the Kashmir Valley (India). *Chemical Geology: Isotope Geoscience Section* **65**, 45-56 (1987).
126. Bhandari, N., Sen Gupta, D., Singhvi, A.K., Nijampurkar, V.N. & Vohra, C.P. Thermoluminescene dating of glaciers. *PACT* **9**, 513-521 (1983).
127. Sohbati, R., Murray, A.S., Jain, M., Buylaert, J.P. & Thomsen, K.J. Investigating the resetting of OSL signals in rock surfaces. *Geochronometria* **30**, 249–258 (2011).
128. Pietsch, T.J., Olley, J.M. & Nanson, G.C. Fluvial transport as a natural luminescence sensitiser of quartz. *Quaternary Geochronology* **3**, 365–76 (2008).
129. Li, S.-H. Luminescence sensitivity changes of quartz by bleaching, annealing and UV exposure. *Radiation Effects and Defects in Solids* **157**, 357-364 (2002).
130. Koul, D.K. & Chougaonkar, M.P. The pre-dose phenomenon in the OSL signal of quartz. *Radiation Measurements* **42**, 1265-1272 (2007).
131. Benea, V. et al. Luminescence dating of neolithic ceramics from lumea nouă, Romania. *Geochronometria* **28**, 9-16 (2007).
132. Ideker, C.J., Byrd Finley, J., Rittenour, T.M. & Nelson, M.S. Single-grain optically stimulated luminescence dating of quartz temper from prehistoric Intermountain Ware ceramics, northwestern Wyoming, USA. *Quaternary Geochronology* **42**, 42-55 (2017).
133. Armitage, S.J. & King, G.E. Optically stimulated luminescence dating of hearths from the Fazzan Basin, Libya: A tool for determining the timing and pattern of Holocene occupation of the Sahara. *Quaternary Geochronology* **15**, 88-97 (2013).

134. al Khasawneh, S., Murray, A., Bonatz, D. & Freiesleben, T. Testing the application of post IR IRSL dating to Iron- and Viking-age ceramics and heated stones from Denmark. *Quaternary Geochronology* **30**, 386-391 (2015).
135. Guérin, G. et al. Multi-method (TL and OSL), multi-material (quartz and flint) dating of the Mousterian site of Roc de Marsal (Dordogne, France): correlating Neanderthal occupations with the climatic variability of MIS 5–3. *Journal of Archaeological Science* **39**, 3071-3084 (2012).
136. Moayed, N.K. et al. Bypassing the Suess-effect: Age determination of charcoal kiln remains using OSL dating. *Journal of Archaeological Science* **120**, 105176 (2020).
137. Ahn, H.-S. et al. Magnetic assessment of OSL and radiocarbon ages of sediments beneath a lava in Jeju Island, Korea: Implication of possible resetting of OSL signals and age constraint of the late Quaternary lava. *Quaternary Geochronology* **48**, 45-63 (2018).
138. Porat, N., Levi, T. & Weinberger, R. Possible resetting of quartz OSL signals during earthquakes—Evidence from late Pleistocene injection dikes, Dead Sea basin, Israel. *Quaternary Geochronology* **2**, 272-277 (2007).
139. Kim, J.H. et al. Experimental investigations on dating the last earthquake event using OSL signals of quartz from fault gouges. *Tectonophysics* **769**, 228191 (2019).
140. Tsakalos, E. et al. Absolute dating of past seismic events using the Optically Stimulated Luminescence (OSL) technique on fault gouge material-A case study of the Nojima Fault Zone, SW Japan. *Journal of Geophysical Research: Solid Earth* **125**, 019257 (2019).
141. Navarro-González, R. et al. Paleoecology reconstruction from trapped gases in a fulgurite from the late Pleistocence of the Libiyan Desert. *Geology* **35**, 117–120 (2007).
142. Godfrey-Smith, D.I., Huntley, D.J. & Chen, W.H. Optical dating studies of quartz and feldspar sediment extracts. *Quaternary Science Reviews* **7**, 373-380 (1988).
143. Li, G. et al. Quantitative precipitation reconstructions from Chagan Nur revealed lag response of East Asian summer monsoon precipitation to summer insolation during the Holocene in arid northern China. *Quaternary Science Reviews* **239**, 106365 (2020).
144. Stokes, S. et al. Alternative chronologies for Late Quaternary (Last Interglacial-Holocene) deep sea sediments via optical dating of silt-sized quartz. *Quaternary Science Reviews* **22**, 925–941 (2003).
145. Singhvi, A.K. & Porat, N. Impact of luminescence dating on geomorphological and palaeoclimate research in drylands. *Boreas* **37**, 536-558 (2008).
146. Telfer, M.W. & Thomas, D.S.G. Late Quaternary linear dune accumulation and chronostratigraphy of the southwestern Kalahari: implications for aeolian palaeoclimatic reconstructions and predictions of future dynamics. *Quaternary Science Reviews* **26**, 2617-2630 (2007).
147. Stevens, T., Thomas, D.S.G., Armitage, S.J., Lunn, H.R. & Lu, H. Reinterpreting climate proxy records from late Quaternary Chinese loess: A detailed OSL investigation. *Earth-Science Reviews* **80**, 111-136 (2007).
148. Kang, S. et al. Early Holocene weakening and mid- to late Holocene strengthening of the East Asian winter monsoon. *Geology* **48**, 1043–1047 (2020).
149. Zeng, L. et al. Response of dune mobility and pedogenesis to fluctuations in monsoon precipitation and human activity in the Hulunbuir dune field, northeastern China, since the last deglaciation. *Global and Planetary Change* **168**, 1-14 (2018).
150. Murton, J.B., Bateman, M.D., Dallimore, S.R., Teller, J.T. & Yang, Z. Identification of Younger Dryas outburst flood path from lake Agassiz to the arctic Ocean. *Nature* **464**, 740–43 (2010).
151. Armitage, S.J., Bristow, C.S. & Drake, N.A. West African monsoon dynamics inferred from abrupt fluctuations of Lake Mega-Chad. *Proceedings of the National Academy of Sciences of the United States of America* **112**, 8543–8548 (2015).
152. Cohen, T.J. et al. Hydrological transformation coincided with megafaunal extinction in central Australia. *Geology* **43**, 195–199 (2015).
153. De Deckker, P. et al. Marine Isotope Stage 4 in Australasia: a full glacial culminating 65,000 years ago – global connections and implications for human dispersal. *Quaternary Science Reviews* **204**, 187–207 (2019).

154. Cohen, K.M. & Gibbard, P.L. Global chronostratigraphical correlation table for the last 2.7 million years, version 2019 QI-500. *Quaternary International* **500**, 20-31 (2019).
155. Vandenberghe, J. Multi-proxy analysis: a reflection on essence and potential pitfalls. *Netherlands Journal of Geosciences — Geologie en Mijnbouw* **91**, 263-269 (2012).
156. Marković, S.B. et al. Loess correlations – Between myth and reality. *Palaeogeography, Palaeoclimatology, Palaeoecology* **509**, 4-23 (2018).
157. Svendsen, J.I. et al. Late Quaternary ice sheet history of northern Eurasia. *Quaternary Science Reviews* **23**, 1229-1271 (2004).
158. Thiede, J. https://en.wikipedia.org/wiki/Quaternary_Environment_of_the_Eurasian_North (2003).
159. Smedley, R.K. et al. New age constraints for the limit of the British-Irish ice sheet on the Isles of scilly. *Journal of Quaternary Science* **32**, 48–62 (2017).
160. Clark, C.D. http://www.britice-chrono.group.shef.ac.uk/ (2018).
161. Lancaster, N. et al. The INQUA Dunes Atlas chronologic database. *Quaternary International* **410**, 3-10 (2016).
162. Lancaster, N. https://www.dri.edu/inquadunesatlas/.
163. Buylaert, J.P. et al. Optical dating of relict sand wedges and composite-wedge pseudomorphs in Flanders, Belgium. *Boreas* **38**, 160–175 (2009).
164. Cheong, C.S. et al. Determination of slip rate by optical dating of fluvial deposits from the Wangsan fault, SE Korea. *Quaternary Science Reviews* **1207-1211**, 22 (2003).
165. Choi, S.-J. et al. Estimation of possible maximum earthquake magnitudes of Quaternary faults in the southern Korean Peninsula. *Quaternary International* **344**, 53-63 (2014).
166. Vandenberghe, D. et al. Late Weichselian and Holocene earthquake events along the Geleen fault in NE Belgium: OSL age constraints. *Quaternary International* **199**, 56-74 (2009).
167. Fattahi, M. et al. Holocene slip-rate on the Sabzevar thrust fault, NE Iran, determined using optically stimulated luminescence (OSL). *Earth and Planetary Science Letters* **245**, 673-684 (2006).
168. Heimsath, A.M., Chappell, J., Spooner, N.A. & Questiaux, D.G. Creeping soil. *Geology* **30**, 111–114 (2002).
169. Gliganic, L.A., May, J.-H. & Cohen, T.J. All mixed up: using single-grain equivalent dose distribution to identify phases of pedogenic mixing on dryland alluvial fan. *Quaternary International* **362**, 23–33 (2015).
170. Bateman, M.D., Frederick, C.D., Jaiswal, M.K. & Singhvi, A.K. Investigations into the potential effects of pedoturbation on luminescence dating. *Quaternary Science Reviews* **22**, 1169–76 (2003).
171. Rink, W.J. et al. Subterranean transport and deposition of quartz by ants in sandy sites relevant to age overestimation in optical luminescence dating. *Journal of Archaeological Science* **40**, 2217-2226 (2013).
172. Gray, H.J., Keen-Zebert, A., Furbish, D.J., Tucker, G.E. & Mahan, S.A. Depth dependent soil mixing persists across climatic zone. *Proceedings of the National Academy of Sciences* **117**, 8750–8756 (2020).
173. Kristensen, J.A. et al. Quantification of termite bioturbation in a savannah ecosystem: application of OSL dating. *Quaternary Geochronology* **30B**, 334-341 (2015).
174. Brown, N.D. Which geomorphic process can be informed by luminescence measurements? *Geomorphology* **367**, 107296 (2020).
175. Madsen, A.T., Murray, A.S., Jain, M., Andersen, T.J. & Pejrup, M. A new method for measuring bioturbation rates in sandy tidal flat sediments based on luminescence dating. *Estuarine, Coastal and Shelf Science* **92**, 464–472 (2011).
176. Xu, Z. et al. Climate-driven changes to dune activity during the Last Glacial Maximum and deglaciation in the Mu Us dune field, north-central China,. *Earth and Planetary Science Letters*, **427**, 149-159 (2015).
177. Stevens, T. et al. Abrupt last glacial dust fall over southeast England associated with dynamics of the British-Irish ice sheet,. *Quaternary Science Reviews*, **250**, 106641 (2020).
178. Porat, N., Rosen, S.A., Boaretto, E. & Avni, Y. Dating the Ramat Saharonim Late Neolithic desert cult site. *Journal of Archaeological Science* **33**, 1341-1355 (2006).

179. Huang, C.C. et al. Extraordinary Floods of 4100-4000 a BP recorded at the Late Neolithic Ruins in the Jinghe River Gorges, Middle Reach of the Yellow River, China. *Palaeogeography, Palaeoclimatology, Palaeoecology* **289**, 1-9 (2010).
180. Saunders, J.W. et al. A mound complex in Louisiana at 5400-5000 years before present. *Science* **277**, 1796-1799 (1997).
181. Burbidge, C.I., Batt, C.M., Barnett, S.M. & Dockrill, S.J. The potential for dating the old Scatness site, Shetland, by optically stimulated luminescence. *Archaeometry* **43**, 589-596 (2001).
182. Roberts, R.G. et al. Luminescence dating of rock art and past environments using mud-wasp nests in northern Australia. *Nature* **387**, 696–699 (1997).
183. Pederson, J.L. et al. Age of Barrier Canyon-style rock art constrained by cross-cutting relations and luminescence dating techniques. *Proceedings of the National Academy of Sciences* **111**, 12986–12991 (2014).
184. Blain, S., Bailiff, I.K., Guibert, P., Bouvier, A. & Baylé, M. An intercomparison study of luminescence dating protocols and techniques applied to medieval brick samples from Normandy (France). *Quaternary Geochronology* **5**, 311-316 (2007).
185. Guibert, P., Christophe, C., Urbanova, P., Guérin, G. & Blain, S. Modeling incomplete and heterogeneous bleaching of mobile grains partially exposed to the light: towards a new tool for single grain OSL dating of poorly bleached mortars. *Radiation Measurements* **107**, 48-57 (2017).
186. Greilich, S., Glasmacher, U.A. & Wagner, G.A. Optical dating of granitic stone surfaces. *Archaeometry* **47**, 645-665 (2005).
187. Chapot, M.S., Sohbati, R., Murray, A.S., Pederson, J.L. & Rittenour, T.M. Constraining the age of rock art by dating a rockfall event using sediment and rock-surface luminescence dating techniques. *Quaternary Geochronology* **13**, 18–25 (2012).
188. Sohbati, R., Murray, A.S., Buylaert, J.-P., Almeida, N.A.C. & Cunha, P.P. Optically stimulated luminescence (OSL) dating of quartzite cobbles from the Tapada do Montinho archaeological site (east-central Portugal). *Boreas* **41**, 452-562 (2012).
189. Petraglia, M. et al. Middle Paleolithic Assemblages from the Indian Subcontinent Before and After the Toba Super-Eruption. *Science* **317**, 114–116 (2007).
190. Armitage, S.J. et al. The southern route 'out of Africa': evidence for an early expansion of modern humans into Arabia. *Science* **331**, 453–456 (2011).
191. Mishra, S., Chauhan, N. & Singhvi, A.K. Continuity of Microblade Technology in the Indian Subcontinent since at least 45 ka: Implications for the Dispersal of Modern humans. *PLoS 1* **8** (2013).
192. Meyer, M.C. et al. Permanent human occupation of the central Tibetan Plateau in the early Holocene. *Science* **355**, 64–67 (2017).
193. Hu, Y. et al. Late Middle Pleistocene Levallois stone-tool technology in southwest China. *Nature* **565**, 82–85 (2019).
194. Zhang, X.L. et al. The earliest human occupation of the high-altitude Tibetan Plateau 40 thousand to 30 thousand years ago. *Science* **362**, 1049-1051 (2018).
195. Roberts, R. et al. Optical and radiocarbon dating at Jinmium rock shelter in northern Australia. *Nature* **393**, 358–362 (1998).
196. Bowler, J.M. et al. New ages for human occupation and climate change at Lake Mungo, Australia. *Nature* **421**, 837–840 (2003).
197. Hamm, G. et al. Cultural innovation and megafauna interaction in the early settlement of arid Australia. *Nature* **539**, 280–283 (2016).
198. Clarkson, C. et al. New evidence for human occupation of northern Australia by 65,000 years ago. *Nature* **547**, 306–310 (2017).
199. Lahaye, C. et al. Human occupation in South America by 20,000 BC: the Toca da Tira Peia site, Piauí, Brazil. *Journal of Archaeological Science* **40**, 2840-2847 (2013).
200. Lahaye, C. et al. Another site, same old song: the Pleistocene-Holocene archaeological sequence of Toca da Janela da Barra do Antonião-North, Piauí, Brazil. *Quaternary Geochronology* **49**, 223-229 (2019).

201. Jacobs, Z. et al. Timing of archaic hominin occupation of Denisova Cave in southern Siberia. *Nature* **565**, 594–599 (2019).
202. Zilhão, J. et al. Last Interglacial Iberian Neandertals as Fisher-Hunter-Gatherers. *Science* **367**, 1443 (2020).
203. Bouzouggar, A. et al. 82,000-year-old shell beads from North Africa and implications for the origins of modern human behavior. *Proceedings of the National Academy of Sciences* **104**, 9964–9969 (2007).
204. Carter, T. et al. Earliest occupation of the Central Aegean (Naxos), Greece: Implications for hominin and Homo sapiens' behavior and dispersals. *Science advances* **5**, eaax0997 (2019).
205. Petraglia, M. et al. Population increase and environmental deterioration correspond with microlithic innovations in South Asia ca. 35,000 years ago. *Proceedings of the National Academy of Sciences* **106**, 12261–12266 (2009).
206. Henshilwood, C.S. et al. A 100,000-Year-Old Ochre-Processing Workshop at Blombos Cave, South Africa. *Science* **334**, 219–222 (2011).
207. Roberts, R.G. et al. New ages for the last Australian megafauna: continent-wide extinction about 46,000 years ago. *Science* **292**, 1888–1892 (2001).
208. Prideaux, G.J. et al. An arid-adapted middle Pleistocene vertebrate fauna from south-central Australia. *Nature* **445**, 422–425 (2007).
209. Haile, J. et al. Ancient DNA reveals late survival of mammoth and horse in interior Alaska. *Proceedings of the National Academy of Sciences* **106**, 22363–22368 (2009).
210. Hocknull, S.A. et al. Extinction of eastern Sahul megafauna coincides with sustained environmental deterioration. *Nature Communications* **11**, 2250 (2020).
211. Medialdea, A., Thomsen, K.J., Murray, A.S. & Benito, G. Reliability of equivalent-dose determination and age-models in the OSL dating of historical and modern palaeoflood sediments. *Quaternary Geochronology* **22**, 11–24 (2014).
212. Kale, V.S., Singhvi, A.K., Mishra, P.K. & Banerjee, D. Sedimentary records and luminescence chronology of Late Holocene palaeofloods in the Luni River, Thar Desert, northwest India. *Catena* **40**, 337-358 (2000).
213. Arnold, L.J., Roberts, R.G., Galbraith, R.F. & DeLong, S.B. A revised burial dose estimation procedure for optical dating of young and modern-age sediments. *Quaternary Geochronology* **4**, 306–325 (2009).
214. Galbraith, R.F. & Roberts, R.G. Statistical aspects of equivalent dose and error calculation and display in OSL dating: an overview and some recommendations. *Quaternary Geochronology* **11**, 1–27 (2012).
215. Arnold, L.J., Demuro, M. & Ruiz, N. Empirical Insights into multi-grain averaging effects from 'pseudo' single-grain OSL measurements. *Radiation Measurements* **47**, 652–658 (2012a).
216. Timar-Gabor, A. et al. On the importance of grain size in luminescence dating using quartz. *Radiation Measurements* **106**, 464-471 (2017).
217. Choi, J.H., Murray, A.S., Cheong, C.S., Hong, D.G. & Chang, H.W. The resolution of stratigraphic inconsistency in the luminescence ages of marine terrace sediments from Korea. *Quaternary Science Reviews* **22**, 1201–1206 (2003).
218. Singarayer, J.S. & Bailey, R.M. Component-resolved bleaching spectra of quartz optically stimulated luminescence: preliminary results and implications for dating. *Radiation Measurements* **38**, 111-118 (2004).
219. Zhou, L.P., Fu, D.P. & Zhang, J.F. An analysis of the components of the luminescence signals of selected polymineral and quartz samples from loess in western China and southern Tajikistan, and their suitability for optical dating. *Quaternary Geochronology* **5**, 149–153 (2010).
220. Galbraith, R.F., Roberts, R.G., Laslett, G.M., Yoshida, H. & Olley, J.M. Optical dating of single and multiple grains of quartz from Jinmium rock shelter, northern Australia: Part I, experimental design and statistical models. *Archaeometry* **41**, 339-364 (1999).
221. Bailey, R.M. & Arnold, L.J. Statistical modelling of single grain quartz De distributions and an assessment of procedures for estimating burial dose. *Quaternary Science Reviews* **25**, 2475–2502 (2006).

222. Combès, B. & Philippe, A. Bayesian analysis of individual and systematic multiplicative errors for estimating ages with stratigraphic constraints in optically stimulated luminescence dating. *Quaternary Geochronology* **39**, 24–34 (2017).
223. Philippe, A., Guérin, G. & Kreutzer, S. BayLum-An R package for Bayesian analysis of OSL ages: An introduction. *Quaternary Geochronology* **49**, 16–24 (2019).
224. Combès, B. et al. A Bayesian central equivalent dose model for optically stimulated luminescence dating. *Quaternary Geochronology* **28**, 62-70 (2015).
225. Thomsen, K.J., Murray, A.S., Bøtter-Jensen, L. & Kinahan, J. Determination of burial dose in incompletely bleached fluvial samples using single grains of quartz. *Radiation Measurements* **42**, 370-379. (2007).
226. Jain, M., Murray, A.S. & Bøtter-Jensen, L. Optically stimulated luminescence dating: How significant is incomplete light exposure in fluvial environments? *Quaternaire* **15**, 143-157 (2004).
227. Gliganic, L.A., Cohen, T.J., Meyer, M. & Molenaar, A. Variations in luminescence properties of quartz and feldspar from modern fluvial sediments in three rivers. *Quaternary Geochronology* **41**, 70–82 (2017).
228. Arnold, L.J. et al. Single-grain TT-OSL bleaching characteristics: Insights from modern analogues and OSL dating comparisons. *Quaternary Geochronology* **49**, 45–51 (2019).
229. Murray, A.S., Thomsen, K.J., Masuda, N., Buylaert, J.P. & Jain, M. Identifying well-bleached quartz using the different bleaching rates of quartz and feldspar luminescence signals. *Radiation Measurements* **47**, 688–695 (2012).
230. Demuro, M., Arnold, L.J., Parés, J.M. & Sala, R. Extended-range luminescence chronologies suggest potentially complex bone accumulation histories at the Early-to-Middle Pleistocene palaeontological site of Huéscar-1 (Guadix-Baza basin, Spain). *Quaternary International* **389**, 191–212 (2015).
231. Möller, P. & Murray, A.S. Drumlinised glaciofluvial and glaciolacustrine sediments on the Småland peneplain, South Sweden – new information on the growth and decay history of the Fennoscandian Ice Sheets during MIS 3. *Quaternary Science Reviews* **122**, 1–29, (2015).
232. Duller, G.A.T. Single-grain optical dating of Quaternary sediments: why aliquot size matters in luminescence dating. *Boreas* **37**, 589–612 (2008).
233. Jacobs, Z., Wintle, A.G., Duller, G.A., Roberts, R.G. & Wadley, L. New ages for the post-Howiesons Poort, late and final Middle stone age at Sibudu, South Africa. *Journal of Archaeological Science* **35**, 1790-1807 (2008).
234. Fitzsimmons, K.E., Stern, N. & Murray-Wallace, C.V. Depositional history and archaeology of the central Lake Mungo lunette, Willandra Lakes, southeast Australia. *Journal of Archaeological Science* **41**, 349-364 (2014).
235. Galbraith, R.G. & Galbraith, R.F. Estimating the component ages in a finite mixture. *Nucl. Tracks Radiat. Meas.* **17**, 197-206 (1990).
236. Jacobs, Z., Duller, G.A.T., Wintle, A.G. & Henshilwood, C.S. Extending the chronology of deposits at Blombos Cave, South Africa, back to 140 ka using optical dating of single and multiple grains of quartz. *Journal of Human Evolution* **51**, 255-273 (2006).
237. David, B. et al. Sediment mixing at Nonda Rock: investigations of stratigraphic integrity at an early archaeological site in northern Australia and implications for the human colonisation of the continent. *Journal of Quaternary Science* **22**, 449–479 (2007).
238. Bateman, M.D. et al. Detecting post-depositional sediment disturbance in sandy deposits using optical luminescence. *Quaternary Geochronology* **2**, 57–64 (2007).
239. Wolfe, S., Murton, J., Bateman, M. & Barlow, J. Oriented-lake development in the context of late Quaternary landscape evolution, McKinley Bay Coastal Plain, western Arctic Canada. *Quaternary Science Reviews* **242**, 106414 (2020).
240. Arnold, L.J. & Roberts, R.G. Stochastic modelling of multi-grain equivalent dose (De) distributions: implications for OSL dating of sediment mixtures. *Quaternary Geochronology* **4**, 204-230 (2009).
241. Rufer, D. & Preusser, F. Potential of autoradiography to detect spatially resolved radiation patterns in the context of trapped charge dating. *Geochronometria* **34**, 1-13 (2009).

242. Smedley, R.K., Duller, G.A.T., Rufer, D. & Utley, J. Empirical assessment of beta dose heterogeneity in sediments: implications for luminescence dating. *Quaternary Geochronology* **56**, 101052 (2020).
243. Nathan, R., Puthusserry, T., Jain, M. & Murray, A.S. Environmental dose rate heterogeneity due to beta microdosimetry and its implications for luminescence dating: Monte Carlo modelling and experimental validation. *Radiation Measurements* **37**, 305–313 (2003).
244. Guibert, P., Bechtel, F., Schvoerer, M., Müller, P. & Balescu, S. A new method for gamma dose-rate estimation of heterogeneous media in TL dating. *Radiation Measurements*, **29**, 561-572 (1998).
245. Burbidge, C.I. & Duller, G.A.T. Combined gamma and beta dosimetry, using Al2O3:C, for in situ measurements on a sequence of archaeological deposits. *Radiation Measurements* **37**, 285-291 (2003).
246. Guérin, G. & Mercier, N. Field gamma spectrometry, Monte Carlo simulations and potential of non-invasive measurements. *Geochronometria* **39**, 40-47 (2012).
247. Guérin, G. & Mercier, N. Preliminary insight into dose deposition processes in sedimentary media on a scale of single grains: Monte Carlo modelling of the effect of water on the gamma dose rate. *Radiation Measurements*, **47**, 541-547 (2012).
248. Degering, D. & Degering, A. Change is the only constant - time-dependent dose rates in luminescence dating. *Quaternary Geochronology* **58**, 101074 (2020).
249. Singhvi, A.K., Banerjee, D., Ramesh, R., Rajaguru, S.N. & Gogte, V. A Luminescence method for dating "dirty" pedogenic carbonates for paleoenvironmental reconstruction. *Earth and Planetary Science Letters* **139**, 321, (1996).
250. Nathan, R.P. & Mauz, B. On the dose-rate estimate of carbonate-rich sediments for trapped charge dating. *Radiation Measurements* **43**, 14–25 (2008).
251. Olley, J.M., Murray, A.S. & Roberts, R.G. The effects of disequilibria in the uranium and thorium decay chains on burial dose rates in fluvial sediments. *Quaternary Geochronology* **15**, 751–760 (1996).
252. Tanner, A.B. in The Natural radiation Environment III, Conf. 780422, Dept. of Commerce (Viginia, 1978).
253. Olley, J.M., Roberts, R.G. & Murray, A.S. Disequilibria in the uranium decay series in sedimentary deposits at Allens cave, Nullarbor Plain, Australia: Implications for dose rate determinations. *Radiation Measurements* **27**, 433–443 (1997).
254. Murray, A.S., Helsted, L.M., Autzen, M., Jain, M. & Buylaert, J.P. Measurement of natural radioactivity: Calibration and performance of a high-resolution gamma spectrometry facility. *Radiation Measurements* **15**, 215-220 (2018).
255. Murray, A.S., Buylaert, J.P. & Thiel, C. A luminescence dating intercomparison based on a Danish beach-ridge sand. *Radiation Measurements* **81**, 32-38 (2015).
256. Durcan, J.A., King, G.E. & Duller, G.A. DRAC: Dose Rate and Age Calculator for trapped charge dating. *Quaternary Geochronology* **28**, 54-61 (2015).
257. Kreutzer, S. et al. Introducing an R package for luminescence dating analysis. *Ancient TL* **30**, 1-8 (2012).
258. Peng, J., Dong, Z., Han, F., Long, H. & Liu, X. R package numOSL: numeric routines for optically stimulated luminescence dating. *Ancient TL* **31**, 41-48 (2013).
259. Lai, Z.P., Brückner, H., Zöller, L. & Füllinga, A. Existence of a common growth curve for silt-sized quartz OSL of loess from different continents. *Radiation Measurements* **42**, 1432-1440 (2007).
260. Burbidge, C.I., Duller, G.A.T. & Roberts, H.M. De determination for young samples using the standardised OSL response of coarse-grain quartz. *Radiation Measurements* **41**, 278-288 (2006).
261. Telfer, M.W. & Hesse, P.P. Palaeoenvironmental reconstructions from linear dunefields: Recent progress, current challenges and future directions. *Quaternary Science Reviews* **78**, 1-21 (2013).
262. Thomsen, K.J., Murray, A. & Jain, M. The dose dependency of the over-dispersion of quartz OSL single grain dose distributions. *Radiation Measurements* **47**, 732–739 (2012).

263. Timar-Gabor, A. et al. Optical dating of Romanian loess: A comparison between silt-sized and sand-sized quartz. *Quaternary International* **240**, 62-70 (2011).
264. Qin, J.T. & Zhou, L.P. Stepped-irradiation SAR: A viable approach to circumvent OSL equivalent dose underestimation in last glacial loess of northwestern China. *Radiation Measurements* **44**, 417–422 (2009).
265. Timar-Gabor, A. & Wintle, A.G. On natural and laboratory generated dose response curves for quartz of different grain sizes from Romanian loess. *Quaternary Geochronology* **18**, 34-40 (2013).
266. Timar-Gabor, A. et al. Fundamental investigations of natural and laboratory generated SAR dose response curves for quartz OSL in the high dose range. *Radiation Measurements* **81**, 150-156 (2015).
267. Chauhan, N., Anand, S., Selvam, P., Mayya, Y.S. & Singhvi, A.K. Extending the upper age limits in the luminescence dating of sediments: A feasibility study of using large grains. *Radiation Measuirements* **44**, 629-633 (2009).
268. Heydari, M. & Guérin, G. OSL signal saturation and dose rate variability: Investigating the behaviour of different statistical models. *Radiation Measurements* **120**, 96-103 (2018).
269. Rittenour, T. Luminescence dating of fluvial deposits: applications to geomorphic, palaeoseismic and archaeological research. *Boreas* **37**, 613-635 (2008).
270. Lai, Z. Chronology and the upper dating limit for loess samples from Luochuan section in the Chinese Loess Plateau using quartz OSL SAR protocol. *Journal of Asian Earth Sciences* **37**, 176-185 (2010).
271. Ankjærgaard, C. et al. Violet stimulated luminescence: geo- or thermochronometer? *Radiation Measurements* **81**, 78-84 (2015).
272. Wang, X.L., Lu, Y.C. & Wintle, A.G. Recuperated OSL dating of fine-grained quartz in Chinese loess. *Quaternary Geochronology* **1**, 89-100 (2006).
273. Arnold, L.J. & Demuro, M. Insights into TT-OSL signal stability from single-grain analyses of known-age deposits at Atapuerca, Spain. *Quaternary Geochronology* **30**, 472-478 (2015).
274. Duller, G.A.T. & Wintle, A.G. A review of the thermally transferred optically stimulated luminescence signal from quartz for dating sediments. *Quaternary Geochronology* **7**, 6-20 (2012).
275. Hansen, V. et al. Towards the origins of over-dispersion in beta source calibration. *Radiation Measurements* **120**, 157-162 (2018).
276. Stevens, T., Armitage, S.J., Lu, H. & Thomas, D.S.G. Sedimentation and diagenesis of Chinese loess: Implications for the preservation of continuous, high-resolution climate records. *Geology* **34**, 849-852 (2006).
277. Yi, S. et al. High resolution OSL and post-IR IRSL dating of the last interglacial-glacial cycle at the Sanbahuo loess site (northeastern China). *Quaternary Geochronology* **30**, 200-206 (2015).
278. Sugisaki, S. et al. OSL dating of fine-grained quartz from Holocene Yangtze delta sediments. *Quaternary Geochronoogy* **30**, 226-232 (2015).
279. Olley, J.M., Caitcheon, G.G. & Murray, A.S. The distribution of apparent doses as determined by optically stimulated luminescence in small aliquots of fluvial quartz: implications of dating young sediments. *Quaternary Science Reviews* **17**, 1033-1040 (1998).
280. Olley, J.M., Caitcheon, G.G. & Roberts, R.G. The origin of dose distributions in fluvial sediments, and the prospect of dating single grains from fluvial deposits using optically stimulated luminescence. *Radiation Measurements* **30**, 207-217 (1999).
281. Sanderson, D.C.W. & Murphy, S. Using simple portable OSL measurements and laboratory characterisation to help understand complex and heterogeneous sediment sequences for luminescence dating. *Quaternary Geochronology* **5**, 299-305 (2010).
282. Muños-Salinas, E., Bishop, P., Sanderson, D.C.W. & Zamorano, J. Interpreting luminescence data from a portable OSL reader: three case studies in fluvial settings. *Earth Surface Processes and Landforms* **36**, 651-660 (2010).
283. Stone, A.E.C., Bateman, M.D. & Thomas, D.S.G. Rapid age assessment in the Namib Sand Sea using a portable luminescence reader. *Quaternary Geochronology* **30**, 134-140 (2015).

284. Simms, A.R., DeWitt, R., Kouremenos, P. & Drewry, A.M. A new approach to reconstructing sea levels in Antarctica using optically stimulated luminescence of cobble surfaces. *Quaternary Geochronology* **6**, 50-60 (2011).
285. Souza, P.E. et al. Luminescence dating of buried cobble surfaces from sandy beach ridges: a case study from Denmark. . *Boreas* **48**, 841-855 (2019).
286. Jenkins, G.T.H., Duller, G.A.T., Roberts, H.M., Chiverrell, R.C. & Glasser, N.F. A new approach for luminescence dating glaciofluvial deposits - High precision optical dating of cobbles. *Quaternary Science Reviews* **192**, 263-273 (2018).
287. Sohbati, R., Murray, A.S., Chapot, M.S., Jain, M. & Pederson, J. Optically stimulated luminescence (OSL) as a chronometer for surface exposure dating. *Journal of Geophysical Research* **117**, B09202 (2012).
288. Rades, E.F., Sohbati, R., Lüthgens, C., Jain, M. & Murray, A. First luminescence-depth profiles from boulders from moraine deposits: Insights into glaciation chronology and transport dynamics in Malta valley, Austria. *Radiation Measurements* **120**, 281-289 (2018).
289. Gray, H.J., Jain, M., Sawakuchi, A.O., Mahan, S. & Tucker, G. Luminescence as a sediment tracer and provenance tool. *Reviews of Geophysics* **57**, 987-1017 (2019).
290. Aitken, M.J. An Introduction to Optical Dating. The Dating of Quaternary Sediments by the Use of Photon-Stimulated Luminescence (Oxford University Press, Oxford, 1998).
291. Karimi Moayed, N. et al. Bypassing the Suess-effect : age determination of charcoal kiln remains using OSL dating. *Journal of Archaeological Science* **120**, 105176 (2020).
292. Vandenberghe, D., Derese, C. & Houbrechts, G. Residual doses in recent alluvial sediments from the Ardenne (S Belgium). *Geochronometria* **28**, 1-8 (2007).
293. Rémillard, A.M. et al. Quartz OSL dating of late Holocene beach ridges from the Magdalen Islands (Quebec, Canada). *Quaternary Geochronology* **30**, 264-269 (2015).
294. Murray, A.S. & Funder, S. OSL dating of a Danish Eemian coastal marine deposit: a test of accuracy. *Quaternary Science Reviews* **22**, 1177-1183 (2003).
295. Sanguino, J. & Montes, R. in Neandertales cantábricos, estado de la cuestión 489-504 (Museo de Altamira, Santander, 2005).
296. Curry, C.W., Bennett, R.H., Hulbert, M.H., Curry, K.J. & Faas, R.W. Comparative Study of Sand Porosity and a Technique for Determining Porosity of Undisturbed Marine Sediment. *Marine Georesources & Geotechnology* **22**, 231–252 (2004).
297. Nelson, M.S. & Rittenour, T.M. Using grain-size characteristics to model soil water content: Application to dose-rate calculation for luminescence dating. *Radiation Measurements* **81**, 142-149 (2015).
298. Zimmerman, D.W. Thermoluminescent dating using fine grains from pottery. *Archaeometry* **13**, 29-52 (1971).
299. Lawson, M.J., Daniels, J.T.M. & Rhodes, E.J. Assessing Optically Stimulated Luminescence (OSL) signal contamination within small aliquots and single grain measurements utilizing the composition test *Quaternary International* **362**, 34-41 (2015).
300. Antohi-Trandafir, O. et al. Luminescence properties of natural muscovite relevant to optical dating of contaminated quartz samples. *Radiation Measurements* **109**, 1-7 (2018).
301. Banerjee, D., Murray, A.S., Bøtter-Jensen, L. & Lang, A. Equivalent dose estimation from a single aliquot of polymineral fine-grains. *Radiation Measurements* **33**, 73–93 (2001).
302. Denby, P.M., Bøtter-Jensen, L., Murray, A.S. & Moska, P. Application of pulsed OSL to the separation of the luminescence components from a mixed quartz/feldspar sample. *Radiation Measurements* **41**, 774–779 (2006).
303. Fan, Y. et al. History and mechanisms for the expansion of the Badain Jaran Desert, northern China, since 20 ka: Geological and luminescence chronological evidence. *The Holocene* **26**, 532-548 (2015).
304. Yu, L., Lai, Z., An, P., Pan, T. & Chang, Q. Aeolian sediments evolution controlled by fluvial processes, climate change and human activities since LGM in the Qaidam Basin, Qinghai-Tibetan Plateau. *Quaternary International* **372**, 23-32 (2015).
305. Hesse, P.P. How do longitudinal dunes respond to climate forcing? Insights from 25 years of luminescence dating of the Australian desert dunefields. *Quaternary International* **410**, 11-29 (2016).

306. Wang, X.F., Zhao, H., Yang, H.Y. & Wang, K.Q. Optical dating reveals that the height of Earth's tallest megadunes in the Badain Jaran Desert of NW China is increasing. *Journal of Asian Earth Sciences* **185**, 104025 (2019).
307. Xu, Z. et al. Critical transitions in Chinese dunes during the past 12,000 years. *Science Advances* **6**, 8020 (2020).
308. Kocurek, G. et al. White Sands Dune Field, New Mexico: Age, dune dynamics and recent accumulations. *Sedimentary Geology* **197**, 313-331 (2007).
309. Li, G.Q. et al. Environmental changes in the Ulan Buh Desert, southern Inner Mongolia, China since the middle Pleistocene based on sedimentology, chronology and proxy indexes. *Quaternary Science Reviews* **128**, 69-80 (2015).
310. Tamura, T. et al. Seasonal control on coastal dune morphostratigraphy under a monsoon climate, Mui Ne dunefield, SE Vietnam. *Geomorphology* **370**, 107371 (2020).
311. Yang, L., Wang, T., Long, H. & He, Z. Late Holocene dune mobilization in the Horqin dunefield of northern China. *Journal of Asian Earth Sciences* **138**, 136-147 (2017).
312. Roberts, H.M., Wintle, A.G., Maher, B.A. & Hu, M. Holocene sediment-accumulation rates in the western Loess Plateau, China, and a 2500-year record of agricultural activity, revealed by OSL dating. *The Holocene* **11**, 477-483 (2001).
313. Lai, Z.P. & Wintle, A.G. Locating the boundary between the Pleistocene and the Holocene in Chinese loess using luminescence. *The Holocene* **16**, 893-899 (2006).
314. Kang, S. et al. Increasing effective moisture during the Holocene in the semiarid regions of the Yili Basin, Central Asia: Evidence from loess sections. *Quaternary Science Reviews* **246**, 106553 (2020).
315. Tecsa, V. et al. Revisiting the chronostratigraphy of Late Pleistocene loess-paleosol sequences in southwestern Ukraine: OSL dating of Kurortne section. *Quaternary International* **542**, 65-79 (2020).
316. Stevens, T. et al. Abrupt last glacial dust fall over southeast England associated with dynamics of the British-Irish ice sheet. *Quaternary Science Reviews* **250**, 106641 (2020).
317. Xu, Z., Stevens, T., Yi, S., Mason, J.A. & Lu, H. Seesaw pattern in dust accumulation on the Chinese Loess Plateau forced by late glacial shifts in the East Asian monsoon. *Geology* **46**, 871-874 (2018).
318. Constantin, D. et al. High-resolution OSL dating of the Costineşti section (Dobrogea, SE Romania) using fine and coarse quartz. *Quaternary International* **334-335**, 20-29 (2014).
319. Fuchs, M. et al. The loess sequence of Dolní Věstonice, Czech Republic: A new OSL-based chronology of the Last Climatic Cycle. *Boreas* **42**, 664-677 (2013).
320. Roberts, H.M., Muhs, D.R., Wintle, A.G., Duller, G.A.T. & Bettis III., E.A. Unprecedented last-glacial mass accumulation rates determined by luminescence dating of loess from western Nebraska. *Quaternary Research* **59**, 411-419 (2003).
321. Bosq, M. et al. Chronostratigraphy of two Late Pleistocene loess-palaeosol sequences in the Rhône Valley (southeast France). *Quaternary Science Reviews* **245**, 106473 (2020).
322. Srivastava, P., Juyal, N., Singhvi, A.K. & Wasson, R.J. Luminescence chronology of river adjustment and incision of Quaternary sediments in the alluvial plain of the Sabarmati River, north Gujarat, India. *Geomorphology* **36**, 217-229 (2001).
323. Zhang, J.F. et al. Optical dating of a hyperconcentrated flow deposit on a Yellow River terrace in Hukou, Shaanxi, China. *Quaternary Geochronology* **5**, 194-199 (2010).
324. Sim, A.K. et al. Dating recent floodplain sediments in the Hawkesbury-Nepean River system, eastern Australia using single-grain quartz OSL. *Boreas* **43**, 1-21 (2014).
325. Arnold, L.J., Bailey, R.M. & Tucker, G.E. Statistical treatment of fluvial dose distributions from southern Colorado arroyo deposits. *Quaternary Geochronology* **2**, 162-167 (2007).
326. Srivastava, P., Singh, I.B., Sharma, M. & Singhvi, A.K. Luminescence chronometry and Late Quaternary geomorphic history stratigraphic record of the Ganga plains, India: A review. *Palaeogeography, Palaeoclimatology, Palaeoecology* **197**, 13-41 (2003).
327. Townsend, K.F.N., M.S.; Rittenour, T.M.; Pederson, J.L. Anatomy and evolution of a dynamic arroyo system, Kanab Creek, southern Utah, USA *GSA Bulletin* **131**, 2094–2109 (2019).

328. Shen, H., Yu, L., Zhang, H., Zhao, M. & Lai, Z. OSL and radiocarbon dating of flood deposits and its paleoclimatic and archaeological implications in the Yihe River Basin, East China. *Quaternary Geochronology* **30**, 398-404 (2015).
329. Jacobs, Z. Luminescence chronologies for coastal and marine sediments. *Boreas* **37**, 508-535 (2008).
330. Bateman, M.D. et al. The evolution of coastal barrier systems: a case study of the Middle-Late Pleistocene Wilderness barriers, South Africa. *Quaternary Science Reviews* **30**, 63-81 (2010).
331. Tamura, T. et al. Luminescence dating of beach ridges for characterizing multi-decadal to centennial deltaic shoreline changes during Late Holocene, Mekong River delta. *Marine Geology* **326-328**, 140-153 (2012).
332. Murari, M.K., Achyuthan, H. & Singhvi, A.K. Luminescence studies on the sediments laid down by the December 2004 tsunami event: Prospects for the dating of palaeo tsunamis and for the estimation of sediment fluxes. *Current Science* **92**, 367-371 (2007).
333. Cunha, P.P. et al. Optical dating of clastic deposits generated by an extreme marine coastal flood: The 1755 tsunami deposits in the Algarve (Portugal). *Quaternary Geochronology* **5**, 329-335 (2010).
334. Tamura, T., Sawai, Y. & Ito, K. OSL dating of the AD 869 Jogan tsunami deposit, northeastern Japan. *Quaternary Geochronology* **30**, 294-298 (2015).
335. Lukas, S., Preusser, F., Anselmetti, F.S. & Tinner, W. Testing the potential of luminescence dating of high-alpine lake sediments. *Quaternary Geochronology* **8**, 23-32 (2012).
336. Fu, X., Cohen, T.J. & Arnold, L.J. Extending the record of lacustrine phases beyond the last interglacial for Lake Eyre in central Australia using luminescence dating. *Quaternary Science Reviews* **162**, 88-110 (2017).
337. Kemp, C.W. et al. Climates of the last three interglacials in subtropical eastern Australia inferred from wetland sediment geochemistry. *Palaeogeography, Palaeoclimatology, Palaeoecology* **538**, 109463 (2020).
338. Lewis, R. et al. Insights into subtropical Australian aridity from Welsby Lagoon, North Stradbroke Island, over the past 80,000 years. *Quaternary Science Reviews* **234**, 106262 (2020).
339. Wallinga, J. & Bos, I.J. Optical dating of fluvio-deltaic clastic lake-fill sediments - A feasibility study in the Holocene Rhine delta (western Netherlands). *Quaternary Geochronology* **5**, 602-610 (2010).
340. Kortekaas, M., Murray, A.S., Sandgren, P. & Björck, S. OSL chronology for a sediment core from the southern Baltic Sea: A continuous sedimentation record since deglaciation. *Quaternary Geochronology* **2**, 95-101 (2007).
341. Gutiérrez, F. et al. Late Holocene evolution of playa lakes in the central sector of the Ebro Depression based on geophysical surveys and morpho-stratigraphic analysis of lacustrine terraces. *Geomorphology* **196**, 177-197 (2013).
342. Long, H., Shen, J., Wang, Y., Gao, L. & Frechen, M. High-resolution OSL dating of a late Quaternary sequence from Xingkai Lake (NE Asia): Chronological challenge of the "MIS 3a Mega-paleolake" hypothesis in China. *Earth and Planetary Science Letters* **428**, 281-292 (2015).
343. Smith, L.N. et al. Timing of lake-level changes for a deep last-glacial Lake Missoula: optical dating of the Garden Gulch area, Montana, USA. *Quaternary Science Reviews* **183**, 23-35 (2018).
344. Olley, J.M. et al. Optical dating of deep-sea sediments using single grains of quartz: a comparison with radiocarbon. *Sedimentary Geology* **169**, 175-189 (2004).
345. Armitage, S.J. Optically stimulated luminescence dating of Ocean Drilling Program core 658B: Complications arising from authigenic uranium uptake and lateral sediment movement. *Quaternary Geochronology* **30**, 270-274 (2015).
346. Houmark-Nielsen, M. Testing OSL failures against a regional Weichselian glaciation chronology from southern Scandinavia. *Boreas* **37**, 660-677 (2008).

347. Hu, G., Yi, C.-L., Zhang, J.-F., Liu, J.-H. & Jiang, T. Luminescence dating of glacial deposits near the eastern Himalayan syntaxis using different grain-size fractions. *Quaternary Science Reviews* **124**, 124-144 (2015).
348. Ou, X. et al. Single grain optically stimulated luminescence dating of glacial sediments from the Baiyu Valley, southeastern Tibet. *Quaternary Geochronology* **30**, 314-319 (2015).
349. Fuchs, M. & Owen, L.A. Luminescence dating of glacial and associated sediments: review, recommendations and future directions. *Boreas* **37**, 636-659 (2008).
350. Alexanderson, H. & Murray, A.S. Luminescence signals from modern sediments in a glaciated bay, NW Svalbard. *Quaternary Geochronology* **10**, 250-256 (2012).
351. Demuro, M., Froese, D.G., Arnold, L.J. & Roberts, R.G. Single-grain OSL dating of glaciofluvial quartz constrains Reid glaciation in NW Canada to MIS 6. *Quaternary Research* **77**, 305-316 (2012).
352. Rowan, A.V. et al. Optically stimulated luminescence dating of glaciofluvial sediments on the Canterbury Plains, South Island, New Zealand. *Quaternary Geochronology* **8**, 10-22 (2012).
353. Thomas, P.J., Murray, A.S., Kjær, K.H., Funder, S. & Larsen, E. Optically Stimulated Luminescence (OSL) dating of glacial sediments from Arctic Russia - depositional bleaching and methodological aspects. *Boreas* **35**, 587-599 (2006).
354. Demuro, M. et al. Optically stimulated luminescence dating of single and multiple grains of quartz from perennially-frozen loess in western Yukon Territory, Canada: Comparison with radiocarbon chronologies for the late Pleistocene Dawson tephra. *Quaternary Geochronology* **3**, 346-364 (2008).
355. Bateman, M.D., Murton, J.B. & Boulter, C. The source of De variability in periglacial sand wedges: Depositional processes versus measurement issues. *Quaternary Geochronology* **5**, 250-256 (2010).
356. Liu, X.J. & Lai, Z.P. Optical dating of sand wedges and ice-wedge casts from Qinghai Lake area on the northeastern Qinghai-Tibetan Plateau and its palaeoenvironmental implications. *Boreas* **42**, 333-341 (2013).
357. Arnold, L.J. et al. Optical dating of perennially frozen deposits associated with preserved ancient plant and animal DNA in north-central Siberia. *Quaternary Geochronology* **3**, 114-136 (2008).
358. Fuchs, M. & Lang, A. Luminescence dating of hillslope deposits-A review. *Geomorphology* **109**, 17-26 (2009).
359. Guerrero, J. et al. Landslide-dam paleolakes in the central Pyrenees, Upper Gállego River Valley, NE Spain: Timing and relationship with deglaciation. *Landslides* **15**, 1975-1989 (2018).
360. Völkel, J., Murray, A., Leopold, M. & Hürkamp, K. Colluvial filling of a glacial bypass channel near the Chiemsee (Stöttham) and its function as geoarchive. *Zeitschrift für Geomorphologie* **56**, 371-386 (2012).
361. Arnold, L.J., Demuro, M., Navazo Ruiz, M., Benito-Calvo, A. & Pérez-González, A. OSL dating of the Middle Palaeolithic Hotel California site, Sierra de Atapuerca, north-central Spain. *Boreas* **42**, 285-305 (2013).
362. Li, Z.-Y. et al. Late Pleistocene archaic human crania from Xuchang, China. *Science* **355**, 969–972 (2017).
363. Feathers, J.K., Rhodes, E.J., Huot, S. & Mcavoy, J.M. Luminescence dating of sand deposits related to late Pleistocene human occupation at the Cactus Hill Site, Virginia, USA. *Quaternary Geochronology* **1**, 167-187 (2006).
364. Froese, D.G. et al. Fossil and genomic evidence constrains the timing of bison arrival in North America. *Proceedings of the National Academy of Sciences* **114**, 3457-3462 (2017).
365. Méndez-Quintas, E. et al. First evidence of an extensive Acheulean large cutting tool accumulation in Europe from Porto Maior (Galicia, Spain). *Scientific Reports* **8**, 3082 (2018).
366. Susino, G.J. Optical dating and microwaste – archaeological applications. *Quaternary Geochronology* **5**, 306-310 (2010).
367. Bate, S. et al. Pottery versus sediment: Optically stimulated luminescence dating of the Neolithic Vinča culture, Serbia. *Quaternary International* **429**, 45-53 (2017).

368. Bailiff, I.K. Methodological developments in the luminescence dating of brick from English late-medieval and post-medieval buildings. *Archaeometry* **49**, 827-851 (2007).
369. Urbanová, P. et al. A novel interdisciplinary approach for building archaeology: The integration of mortar "single grain" luminescence dating into archaeological research, the example of Saint Seurin Basilica, Bordeaux. *Journal of Archaeological Science: Reports* **20**, 307-323 (2018).
370. Feathers, J.K., Johnson, J. & Kembel, S.R. Luminescence dating of Monumental stone architecture at Chavín de Huántar, Perú. *Journal of Archaeological Method and Theory* **15**, 266-296 (2008).
371. Johnson, M.O. et al. Quantifying the rate and depth dependence of bioturbation based on optically-stimulated luminescence (OSL) dates and meteoric 10Be. *Earth Surface Processes and Landforms* **39**, 1188-1196 (2014).
372. Furbish, D.J. et al. Soil Particle Transport and Mixing Near a Hillslope Crest: 2. Cosmogenic Nuclide and Optically Stimulated Luminescence Tracers. *Journal of Geophysical Research: Earth Surface* **123**, 1078-1093 (2018).
373. Liu, J.F. et al. OSL and AMS Dating of the Penultimate Earthquake at the Leigu Trench along the Beichuan Fault, Longmen Shan, in the Northeast Margin of the Tibetan Plateau. *Bulletin of the Seismological Society of America* **100**, 2681-2688 (2010).
374. Yang, H.L., Chen, J., Thompson, J.A. & Liu, J.F. Optical dating of the 12 May 2008, Ms 8.0 Wenchuan earthquake-related sediments: Tests of zeroing assumptions. *Quaternary Geochronology* **10**, 273-279 (2012).
375. Torabi, M., Fattahi, M., Amini, H., Ghassemi, M.R. & Karimi, N. OSL dating of landslide-dammed-lake deposits in the North of Tehran, Iran: 958 Ray-Taleghan/Ruyan earthquake. *Quaternary International* **In press**.
376. Rizza, M. et al. Using luminescence dating of coarse matrix material to estimate the slip rate of the Astaneh fault, Iran. *Quaternary Geochronology* **6**, 390-406 (2011).
377. Chen, Y., Li, S.-H., Sun, J. & Fu, B. OSL dating of offset streams across the Altyn Tagh Fault: Channel deflection, loess deposition and implication for the slip rate. *Tectonophysics* **594**, 182-194 (2013).
378. Gong, Z.J., Li, S.-H. & Li, B. Late Quaternary faulting on the Manas and Hutubi reverse faults in the northern foreland basin of Tian Shan, China. *Earth and Planetary Science Letters* **424**, 212-225 (2015).
379. Stockmeyer, J.M. et al. Active thrust sheet deformation over multiple rupture cycles: a quantitative basis for relating terrace folds to fault slip rates. *Geological Society of America Bulletin* **129**, 1337-1356 (2017).
380. Peltzer, G. et al. Stable Rate of Slip Along the Karakax Section of the Altyn Tagh Fault from Observation of Interglacial and Postglacial Offset Morphology and Surface Dating. *Journal of Geophysical Research: Solid Earth* **125**, e2019JB018893 (2020).
381. Sohbati, R., Borella, J., Murray, A., Quigley, M. & Buylaert, J.-P. Optical dating of loessic hillslope sediments constrains timing of prehistoric rockfalls, Christchurch, New Zealand. *Journal of Quaternary Science* **31**, 678-690 (2016).
382. Preusser, F., Rufer, D. & Schreurs, G. Direct dating of Quaternary phreatic maar eruptions. *Geology* **39**, 1135-1138 (2011).
383. Rittenour, T.M., Riggs, N.R. & Kennedy, L.E. Application of single-grain OSL to quartz xenocrysts within a basalt flow, San Francisco volcanic field, northern Arizona, USA. *Quaternary Geochronology* **10**, 300-307 (2012).
384. Liu, Z., Zhao, H., Wang, C.M. & Li, S.H. Estimation of paleo-firing temperatures using luminescence signals for the volcanic lava baked layer in Datong, China. *Quaternary Geochronology* **30**, 363-368 (2015).
385. Westgate, J.A. et al. Changing ideas on the identity and stratigraphic significance of the Sheep Creek tephra beds in Alaska and the Yukon Territory, northwestern North America. *Quaternary International* **178**, 183-209 (2008).
386. Anechitei-Deacu, V., Timar-Gabor, A., Fitzsimmons, K.E., Veres, D. & Hambach, U. Multi-method luminescence investigations on quartz grains of different sizes extracted from a loess

section in southeast Romania interbedding the campanian ignimbrite ash layer. *Geochronometria* **41**, 1-14 (2014).
387. Herman, F., Rhodes, E.J., Braun, J. & Heiniger, L. Uniform erosion rates and relief amplitude during glacial cycles in the Southern Alps of New Zealand, as revealed from OSL-thermochronology. *Earth and Planetary Science Letters* **297**, 183-189 (2010).
388. Guralnik, B. et al. OSL-thermochronometry using bedrock quartz: A note of caution. *Quaternary Geochronology* **25**, 37-48 (2015).

Supplementary Information

(Section numbering corresponds to the relevant section number in the main text)

2. Experimentation

(a) Sampling

Luminescence dating obviously starts in the field, where the sample containing quartz grains - usually sediment - must be collected. Since OSL dates the last exposure of sediment to daylight, one must avoid light exposure during sampling. The surface of the sediment, or of the sedimentary sequence of interest, is first cleaned by scraping back. This is not only to avoid the light exposed first few mm of the exposure, but also to provide a clear view of the stratigraphy and so avoid locations that may have been affected by post-depositional disturbances (ice wedges, animal burrows, roots, etc.). At least the first few cm must be removed; it is better to cut a section back by > 1 m to avoid air-exposed material and so to take samples where oxidation/reduction conditions and moisture content are more likely to be representative of the long term burial (see Section 2.1 on dose rates). All these operations can be done in full daylight and taking photographs of sampling site (overview) and sampling locations (detail) is recommended.

There are then two approaches to collecting a sediment sample: the simplest is to hammer tubes (metal or plastic, depending on the deposit) into the cleaned section; these are often intended for one-time use, but may be reusable [1]. This method is only suitable when the unit to be sampled is of sufficient thickness that the tube will not cross sedimentological boundaries. Ideally the gamma dose rate gradient across the tube should also be small; if possible, the tube should be at least 15 cm from any boundary. A plug of wadded paper or crumpled plastic bag should be placed in the tube, at the end closest to the section. This will support the sediment as it enters the tube and reduce the risk of it collapsing and mixing exposed and unexposed material. The tube must be filled completely, either with sample or by packing with plastic, to ensure that the material cannot move and mix during transport. In the laboratory the potentially light-exposed outer ~2-3 cm of each end of the tube is retained for radionuclide concentration measurements, and any other sedimentological analyses (e.g. grain size, mineralogy, geochemistry, ancient DNA, tephrochronology, etc.). The inner part of the tube is used for OSL measurements, and possibly for water content measurements.

If the unit is too thin to be sampled with a tube, then the second approach is to operate in the dark – either at night (moonlight is very low intensity, and will not significantly affect the OSL during the

short sampling exposure, see [2]), or under an opaque covering such as a tarpaulin. In both cases, it is safe to use a controlled light source, such as headlamp emitting dim orange light, or a red LED (e.g. bicycle rear light). It is usual to collect two parts for each sample: one mainly for OSL analysis and the other mainly for radiochemical analysis. The previously cleaned surface is first scraped to remove a further cm or so. This part is likely to have been exposed to daylight after the cleaning of the section, and is not suitable for OSL measurement; it is removed and retained for measurement of the radioelement concentrations and for any complementary measurements. Since exposure to light is unimportant for such measurements, this part of the sample may be collected in transparent bags. The second part of the sample, taken from further into the section, must be protected from light exposure, either by packing into metal containers, or fully opaque plastic bags. Usually a few hundred grams is sufficient – but that of course depends on the concentration and grain-size distribution of quartz grains in the sample. A carbonate-rich sandstone will generally yield less quartz than a desert sand, and a marine/lake core fewer sand-sized grains than a beach sand. If a narrow-grain-size fraction is to be targeted (e.g. for single-grain OSL), the amount of sediment required may be greater than usual.

If the target is ceramic material (pottery, bricks, tiles) or cobbles, heated stones etc., all sampling can be undertaken in daylight, although direct sunlight should be avoided. This is because, in the case of ceramics and heated stones, the potentially light-exposed surface of the sample is discarded in the laboratory, and in the case of cobbles, light is attenuated so rapidly that a few minutes of daylight does not affect the average luminescence signal in the outer 1 mm.

During sampling one must also consider the water content history of the site and the collection of (separate) samples for the present day water content. A subsample of the OSL samples (from inside tube) or the transparent bags (see above) can be used to determine this and the saturated water content (see in section 2.1.2 below). In order to retain as much moisture as possible sealable bags should be used and the ends of the tubes covered with plastic and sealed with tape.

Finally, sampling is the occasion to collect information relevant for calculating cosmic dose rates (Figure S1) by measuring or estimating the overburden of a sample. This includes the nature of the overburden (e.g. cave roof, sediment, etc.), the density and above all the thickness of the material covering every sample. The elevation of the site above sea level and geographical coordinates (latitude, longitude) should also be recorded. These field observations are used to calculate the cosmic dose rate [3]. Furthermore, in some cases (see section S2.1 below) where the sediment is heterogeneous on a scale of 10-50 cm (presence of rocks, sediment unconformity, boundary between sediment and air, or sediment and bedrock, etc.) it may be necessary to measure in situ gamma dose rates. It is often also possible to collect two separate dose rate samples (one from sediment to be dated and one from the adjacent rock/sediment causing heterogeneity), measure the radionuclide concentrations for both samples and then model the gamma dose rate (see Appendix H in [4]).

(b) Sample preparation

In the laboratory, that part of the sample intended for dose rate measurements is homogenised (usually by grinding) so that even a small sample of less than few grams is representative of the whole. This part may be from the ends of a sampling tube, or the outer few mm of a ceramic or heated stone. Section S2.1 lists typical methods for dose rate determination. It is good practice to keep a portion of the non-light-exposed material as back-up in case something goes wrong in sample preparation. The remaining part of the sample intended for OSL measurements undergoes several treatment steps to extract quartz grains (see Figure S2). The unexposed inner part of ceramics and heated stones is gently crushed. Then the crushed material, or the sediment, is wet sieved - a constrained grain size fraction is of importance not only because of measurement practicalities, but also because both laboratory and environmental dose rates are, to some degree, grain-size dependent – see section S2.1 below. The factors driving the selection of grain size are: (i) the abundance of that fraction in the samples; (ii) the ability to chemically etch the outer surface of the grains to remove the alpha-irradiated component (typically not smaller than fine sand, i.e. > 63 μm – grains must be large enough, or else nothing is left after the HF treatment described below); (iii) ease of manipulation of the grains. Generally, some choice is made within the range 63-300 μm (e.g. 90-125 μm or 180-250 μm); the fraction 150-180 μm is most suitable for measurements using single-grain discs with e.g. ø 200 μm holes.

The sample should remain at or close to room temperature in all the steps outlined below, to avoid the risk of thermal fading of the OSL signal; this applies particularly to the HF digestions steps. The selected size fraction is treated with 10% HCl for at least 30 minutes (until no reaction is visible) to remove carbonates - these may impede the reaction with HF - and with 10% H_2O_2 (for up to a few days) to remove finely disseminated organics. After HCl and H_2O_2 treatments, the grain fractions are washed with water (usually 2-3 times). Note that it is usually easier to soak more compact fine-grained (clayey-silty) sediment in water and treat with HCl, H_2O_2 first, to disaggregate the grains, before wet sieving. This is also true for carbonate-rich sandstones (e.g. aeolianites).

After sieving and treating with HCl and H_2O_2, there should be at least a few gram(s) of sample, at this point mainly a mixture of quartz, feldspar and possibly heavy-mineral grains in the chosen grain size fraction. If only quartz is desired, the sample may be placed directly in concentrated HF (40%); usually ~1 hour is sufficient to remove feldspar and etch the surface of the quartz grains (see below). If the feldspar grains are also required, then prior mineral separation is necessary (K-feldspars in particular are commonly used in other approaches to luminescence dating). Prior to mineral separation the mixed quartz/feldspar fraction can be etched for up to 40 min in 10% HF to remove surface coatings (e.g. iron oxides) and attached clay grains, washed in 10% HCl for ~20 mins, and then with water and dried. This step improves recovery in the following separation step. Density separation using aqueous heavy liquids (e.g. lithium heteropolytungstate, or LST) is a safe and convenient

approach; a density of 2.70 $g.cm^{-3}$ allows the heavy minerals to sink; 2.62 $g.cm^{-3}$ allows a quartz-rich fraction to sink; 2.58 $g.cm^{-3}$ allows a Na-rich feldspar fraction to sink, and floats mainly K-rich feldspar grains. Some laboratories use only a single 2.58 $g.cm^{-3}$ step, and rely on HF to remove any denser feldspars that remain in the quartz-rich fraction. Any heavy minerals surviving the HF treatment rarely, if ever, make a significant contribution to the quartz luminescence signal. Magnetic separation is also used to separate quartz and feldspar grains [5].

Finally, treatment with concentrated HF (40%) for 1 hour removes any remaining feldspar, and ~10 µm from the outer surface of the quartz grains, thus removing most of the quartz layer exposed to alpha particles from the surrounding sedimentary matrix during burial. The internal alpha activity of quartz is very small, and so this step significantly simplifies the dosimetry calculations. Some laboratories then soak the sample in 10% HCl for several hours to remove any fluorides that might have precipitated on the grain surfaces, because some fluoride salts are luminescent. Although there is no evidence that these amorphous precipitates are in fact a significant source of contamination in quartz OSL, some fluoride residues can be of sufficient thickness to significantly attenuate the OSL signal. Finally, the samples are washed (typically 3 times) with water and dried; it may be desirable then to sieve the samples again, to define the minimum grain size during beta irradiation, and, for single grain measurements, to avoid the risk of multiple grains in each hole in the sample holder. The quartz is then tested for signal purity (Section S2.2.1(a)); if it fails this test, the HF etch can be repeated (the additional mass loss will have a small effect on the average natural beta dose to the grains).

2.1. Dose Rate

2.1.1. Basic concepts

(a) Dose rate calculation using the infinite matrix assumption.

Various methods for determining the dose rate are summarised in Table S1. Concentrations of radionuclides may be expressed in activity concentrations [$Bq.kg^{-1}$] or mass concentrations. To calculate the activity concentration from a mass concentration (C_0, [$g.kg^{-1}$]) measurement, the atom concentration per unit mass of sediment (N, [kg^{-1}]) is first calculated using $N=C_0$ [$g.kg^{-1}$]/ Z (atomic weight [$g.mol^{-1}$]) x N_A (Avogadro's number [mol^{-1}]). N is then multiplied by the relevant decay constant (λ, [s^{-1}]) to give the radionuclide activity concentration. Measured concentrations may be reported in ppm [$\mu g.g^{-1}$] for U and Th, and percentage [%] for K; these must first be converted to [$g.kg^{-1}$]. In the case of K, the mass concentration of ^{40}K must then be derived using the isotopic abundance (0.0117%).

Finally, for each nuclide, multiplying the activity concentration by the average energy emitted per disintegration (see e.g. https://www.nndc.bnl.gov/nudat2/ given in MeV, 1 MeV=1.6×10^{-13} J;) gives

what is known as the infinite matrix dose rate. Relevant conversion factors ($C_0 \times N_A \times \lambda/Z$) (summarised in Table S2) are regularly compiled and updated (e.g. [6]). Table S3 uses these data to derive infinite matrix dose rates from a sand containing representative concentrations of ^{40}K, ^{238}U and ^{232}Th. Figure S3 shows the ^{238}U and ^{232}Th radioactive decay chains, and Figure S4 groups radionuclides according to their potential mobility in sediment, and presents the relative contribution of each group to the total dose rate, assuming the relative activity concentrations of Table 3. Figure S5 summarises the potential variability in ^{40}K, ^{238}U and ^{232}Th concentrations, and their relative contributions to dose rates. Figure S6b) illustrates how variable beta dose rates can be at the 100 µm scale.

(b) In situ gamma dose rate measurements

In some cases, sediment is heterogeneous at the scale of the penetration distance of gamma rays (~30-50 cm, see Figure S6a), e.g. if it is poorly sorted, and includes pebble and cobbles, or is adjacent to a rock wall. Then the infinite matrix gamma dose rate may not be representative of the gamma dose rate to which the sample was exposed during burial. As an alternative, the gamma dose rate may be measured in situ, at the sample location, e.g. with luminescent Al_2O_3:C pellets. Aluminium oxide is very similar to quartz in terms of dose absorption characteristics, and doping with carbon gives this material a very sensitive luminescence response to dose [7]. In practice, pellets are left buried in an aluminium tube of ~2-3 mm thickness (to prevent beta particles from reaching the pellets) for 6-12 months, after which the absorbed dose is sufficient to induce a measurable OSL signal [8], [9]. This directly measured dose rate is the sum of gamma and cosmic dose rates, as affected by escape of ^{222}Rn and the water content of the sediment over the period of measurement. The other common way of determining in situ gamma dose rates involves the use of a field gamma spectrometer, typically with a NaI(Tl) or LaBr probe. Calibration involves measurements in infinite media with known radionuclide concentrations [10]. Data analysis may consist of estimating effective K, U and Th concentrations using the 'windows technique' (see Appendix L in [4]), and then converting these concentrations into effective infinite matrix dose rates. The concentration of K is based on the emission rate of the 1461 keV peak, of U of the 1764 keV peak and of Th of the 2615 keV (e.g. [11]). Otherwise, one may use the proportionality between gamma dose rate and the count rate above a certain energy channel, in what is called the threshold technique [12], [13]. The advantage of the threshold technique lies in the inclusion of a greater portion of the recorded spectra to estimate the gamma dose rates, thereby reducing the uncertainties for a given counting time (typically several minutes), but this approach does not give any nuclide-specific information.

2.1.2. Practicalities

Water content measurements – Constraining the average water content of a deposit is very important to the accuracy of a luminescence age, because a 1% increase/decrease in life-time average

water content typically leads to a 1% increase/decrease in derived age[1]. Well-sorted sands have only a small variation in porosity, from fully (~38%) to loosely (46%) compacted [14], and because the grain surfaces are in physical contact (in contrast to e.g. clay-rich deposits) it is very difficult to over-compress sand by increased overburden pressure. When fully saturated with water, 42% porosity corresponds to 21% by weight water content. Because the packing density is reproducible, a saturation water content can be measured for a sandy deposit by adding sediment and excess water to say, a pre-weighed 100 ml syringe and applying pressure to remove the excess water. The point at which the syringe plunger stops moving is well-defined, and increasing the pressure does not extrude more water. The syringe and wet sand are weighed to obtain the saturated weight, and then placed in an oven and dried to obtain the dry weight – the ratio of the weight loss of the saturated sample during drying to the dry weight is the saturation water content. If the sediment was likely to have been below the ground-water table throughout the burial period, this is the lifetime average water content. Otherwise, the likely fraction of saturation during the burial period must be estimated from a knowledge of the local hydrology (drainage, precipitation, etc.) and sediment characteristics [15]. The observed water content (*i.e.* the water content in a field sample, measured simply by drying a known weight of wet material) can often be taken as a lower limit to lifetime water content, since typical sampling sites (cleaned sections, gully walls, river or road cuts etc.) are usually significantly drier than corresponding material a few metres deeper into the section. In the worst case, where no further constraints can be placed on water content history, the mid-point between field and saturated water content can be chosen, and an estimate of uncertainty adopted, equal to 25% of the range. Then all possible values are covered by ±2 times the uncertainty. For example a measured water content of, say, 9% (cf. saturation water content of 21%) would give a mean lifetime water content of 15±3% by weight, implying an overall contribution to the uncertainty on the age of ~3% [16]. This is not large compared to the expected minimum uncertainty of ~5% (uncertainties added in quadrature, see Table S8), and so is not of major concern. Similar arguments can be used to constrain the effects of the infilling of porosity by carbonate.

The water content of a ceramic buried in a sediment is more complicated. The porosity of a ceramic will differ from that of the sediment matrix, but it is readily measured by simply saturating the ceramic in water, weighing, drying and weighing again. Then it is assumed that the fraction of saturation that applies to the matrix also applies to the ceramic [4]. The lifetime average water content estimated for the matrix is applied to the gamma dose rate, and that for the ceramic to the beta dose rate.

[1] The age calculation spreadsheet attached to this paper allows the reader to test the sensitivity of the ages to various parameters.

2.2. Testing the applicability of a SAR protocol

2.2.1. Dose estimation using SAR

(a) Testing for quartz purity

The chemical pretreatment intended to remove any feldspar contamination is not always completely successful [17, 18]. The reasons for this are unclear, but presumably involve occluded feldspar grains, or even feldspathic-like impurities within individual quartz grains. This is a problem because the luminescence from feldspar impurities is significantly unstable, and much more difficult to bleach. Unfortunately, feldspar is sensitive to the wavelengths used to stimulate quartz (usually 450 to 530 nm), and so can contaminate the quartz signal. If additional etching with HF does not remove residual signal contamination, then instrumental separation must be considered. For stimulation with blue or green wavelengths, the decay rate of the feldspar signal is considerably slower than that of the quartz fast component, and so the use of the early background subtraction approach helps to reduce the importance of any feldspar contamination. But, feldspar, in contrast to quartz [19], is sensitive to infrared (IR) stimulation. This characteristic can be used to test for, and to reduce, contamination of the quartz OSL by inserting an IR stimulation immediately prior to the measurement of L_i (but not T_i) in an additional recycling ratio test [20]. If this $(L_i/T_i)/(L_1/T_1)$ ratio is indistinguishable from that measured without IR (see section 2.2.2 in main text), then feldspar does not contribute significantly to the quartz signal. In samples where the feldspar contamination is of significance, it can be reduced by inserting the IR stimulation step in front of every L and T measurement [21], although this is expensive in measurement time. There are also other instrumental methods for minimising any feldspar contribution, but these are not in routine use [22, 23, 24].

(b) Instrumentation for determining the D_e

The instrumentation for determining the absorbed dose is relatively simple and comprises four main components: 1) luminescence detector, 2) stimulation light source, 3) source of ionising radiation and 4) heating system. **Error! Reference source not found.** summarises the relationship of these four components to the quartz grains to be measured.

The main challenge in designing such a system is the instrumental sensitivity. The ability to measure an absorbed dose depends both on the sensitivity of the sample (i.e. the number of photons emitted per unit mass [kg^{-1}] and per unit absorbed dose [$kg^{-1}.Gy^{-1}$]), on the instrument sensitivity, i.e. the fraction of the emitted photons that are actually detected by the instrument (detection efficiency), and the relationship of this signal to the instrument background noise. Detection efficiency depends on the light path (controlling the fraction of the emitted signal reaching the detector, and dependent on

geometry, mirrors, lenses and filters), the choice of photon detector (how many photons arriving at the detector are required to give a detected event – the quantum efficiency) and the wavelength and intensity of the stimulation light source (the more rapidly the charge is released (detrapped), the stronger the initial luminescence signal compared to background. For a given detection wavelength, the electron detrapping rate depends on the wavelength-dependent photoionization cross-section and the power density of the stimulation light).

The luminescence detector consists of a photon detector and detection filter(s). Natural phosphors such as quartz are relatively inefficient in converting absorbed dose into luminescence and thus the emitted luminescence signal is usually too weak to be detected by the naked eye. To measure such signals precisely, a highly sensitive light detector with a low noise (background) level and good light collection are essential. The latter requires as large as possible solid angle subtended by the detector surface at the sample – this is usually achieved by as short as possible distance between sample and detector, or by focussing through lenses. In OSL the luminescence signal is emitted as a consequence of optical stimulation, which is ~10^{15} times more intense than the OSL signal itself. OSL is an anti-Stokes emission, i.e. the energy of the optical stimulation is less than that of the emitted luminescence. Appropriate detection filters must be used both to separate the luminescence from the stimulation light and to define the spectral detection window.

Photon detector - Figure S8 shows the emission spectrum from quartz obtained by stimulation with 647 nm laser light. Quartz has a relatively broad OSL emission peaking at ~360 nm (full width half maximum, FWHM ~80 nm). Photomultiplier tubes (PMT) operating in photon-counting mode, sensitive in the blue/UV range are most commonly used for detecting quartz OSL, mainly because of their high sensitivity, large dynamic range and low dark count rate. A high signal-to-noise ratio is particularly important when measuring insensitive samples and/or samples having absorbed small radiation doses (i.e. young samples). The quantum efficiency (the effectiveness of the PMT at converting photons into electrons) is typically up to ~30 %, depending on the wavelength of the luminescence. The only major drawback of using PMTs is that they do not provide information on the spatial variation of the emitted luminescence. In applications where such spatial information is of importance (e.g. rock surface luminescence dating) electron-multiplier charge-coupled devices (EMCCD) can be used, although they are in general less sensitive than PMTs (e.g. [25], [26], [27]).

Detection filters - The use of detection filters is important both to define the wavelength window of interest and to separate the emitted luminescence from scattered stimulation light. In quartz OSL dating, the UV/blue emission is usually detected through a broadband Hoya U-340 glass filter, which has its peak transmission at 340 nm with a FWHM of 80 nm (see Figure S9). The main emission from quartz is centred at 365 nm and thus, in principle, a significant improvement in light detection is available by choosing a detection filter closer to the main emission of quartz. However, moving the

detection window closer to the stimulation wavelength (usually 470 nm, see below) is likely to lead to a significant increase in background signal (from breakthrough of the stimulation light) and hence the signal-to-noise ratio is not necessarily improved [28].

Stimulation light source – In quartz OSL, the electron detrapping rate depends both on the intensity and the wavelength of the optical stimulation light (see Figure S10; [29, 30]); the more intense and the shorter the wavelength the stronger the OSL signal per unit time. For most OSL applications, optical stimulation is at a constant light intensity (continuous wave mode), but modulating the intensity of the stimulation light (e.g. linear modulated OSL, LM-OSL; [31]) can be used to visually separate the traps involved in the OSL production. In some applications, pulsing the stimulation light and only detecting in between short (~50 μs) bursts of stimulation light (Pulsed OSL, POSL) can help to separate quartz and feldspar OSL signals instrumentally [23]. POSL stimulation can also be used to gain insight into the physics of recombination processes (e.g. [32]).

Optical stimulation of quartz can be achieved using any visible light source such as filtered lamp systems [28], lasers [33, 34, 26], light emitting diodes (LEDs) [35] and laser diodes [36, 26]. In most quartz multi-grain OSL dating applications, blue (450-470 nm) or green (~525 nm) LEDs with power densities at the sample position ranging between ~40 and 100 mW/cm^2 are used, resulting in the decay of the fast OSL component in a few seconds. As LEDs have a broad emission (FWHM of ~30 nm) it is often necessary to stimulate through cut-off filters to ensure an effective separation of stimulation light and detection windows ([37], see Figure S9). Higher energy light sources (e.g. 405 nm laser diode [38]) can be used to access deeper traps insensitive to blue light. In single-grain applications, stimulation by a green (532 nm) solid state laser providing a power density of ~50 W/cm^2 is commonly used [39].

Source of ionising radiation - The measured natural OSL signal must be calibrated in terms of absorbed dose. As different aliquots can have very different luminescence sensitivities, it is necessary to calibrate aliquots individually. This calibration is performed by comparing the natural OSL signal to that arising from a known laboratory dose given to each aliquots (using a SAR protocol, Section 2.2 in main text). This known dose can be given by any source of ionising radiation, but for convenience this is usually a beta source containing the artificial radionuclide ^{90}Sr ($\tau_{½}$ 28.8 years) and its short lived progeny ^{90}Y. This combination of emitters has a maximum beta energy of 2.27 MeV and a mean energy of ~600 keV, which makes it relatively easy to shield sufficiently for it to be safe to use.

The laboratory dose rate to a quartz sample depends on the activity of the source, the source/sample distance, sample grain size, and on the substrate material on which the grains sit. Because of this the source must be calibrated for each irradiation geometry (particularly for different substrates and grain-size range). The calibration is usually done by using a portion of quartz grains that has been given a

known dose using a standardised gamma source. An appropriate SAR protocol then aims at determining the duration of beta irradiation that provides a sensitivity-normalised luminescence intensity equal to that induced by the reference gamma dose [40]. Some laboratories make available sensitive quartz which has absorbed a well-known dose, so that others without access to a calibrated gamma source can calibrate their own beta source as required.

Heating system – to obtain accurate measurements of D_e, it is important to perform reproducible thermal pre-treatments and to be able to keep the aliquot at a given temperature during optical stimulation. OSL dating systems will usually heat up to 700 °C using heating rates typically ranging between 0.01 and 10 °C /s, although temperatures above 350 °C are rarely used.

4. Reproducibility and data deposition

(a) ***Data reporting:*** It is common in the literature to read articles describing equivalent dose determination in detail, while dose rate data are often summarised in a way that renders recalculation or reproducibility studies difficult. Until recently most articles containing luminescence ages presented new data (with variable degree of detail). However, publications addressing larger scale questions by presenting meta-analyses of published datasets are becoming more frequent. To encourage this, detailed information behind the OSL ages is required, both to allow the assessment of the quality of the data, and to ensure that the same underlying assumptions are adopted, and so enable the derivation of a coherent data set. Bayesian modelling of OSL ages under stratigraphic constraints may require a combination of raw measurement files and details of calibration uncertainties, both for equivalent dose and dose rate measurements [41], [42]. Here we discuss data reporting in terms of good practice, in the sense that it provides sufficient information for later comparisons to be made between studies that focus on the same research question – and thus, on the same samples, stratigraphic records or dated events.

When publishing OSL results, it should be made clear to the reader whether the signal is fast component-dominated (perhaps with a figure showing a comparison with known fast-component dominated material such as calibration quartz [40]), and that the interpolation is not compromised by saturation effects (e.g. using an illustrative dose response curve, see Figure 4(c,f)). Although recuperation and recycling are important (and can be shown on the dose response curve), it is most important to document the dose or light recovery ratio for the material under consideration (Section 2.2.2(vi)). In general, it is not necessary to give a value for each sample from the same sedimentary suite, a single average with standard error and number of measurements (as in Figure 6(b)) is usually sufficient.

In presenting dose rates, the methods adopted should be presented first, starting with the type of instruments and experimental conditions (Table S1). Second, we recommend that the measured values are reported: for example, if high resolution gamma spectrometry has been used, then concentrations in K, U and Th should be given; if a beta counting system is used, then count-rates should be given. Reference to the calibration standards and procedures is of course desirable – laboratories commonly publish their protocols, e.g. [43], [44], [45].

The source of the conversion factors is important: in the two examples above, conversion is from (activity) concentrations to dose rates and from count rates to dose rates, for gamma spectrometry and beta counting, respectively (Table S2). The reader should also be able to find (i) which factors were used to account for grain size attenuation of beta dose rates (e.g. Table S4 below taken from [46]); (ii) if alpha dose rates were taken into account (and if so, which alpha dose rate efficiency factors were used); (iii) what water content value was used, how it was determined and which factors were used to account for the effect of water on dose rates (see Tables S5 and S6, and e.g. [47], [48], [16]); (iv) if an internal dose rate was considered - and if so, if it was measured or simply assumed [49]; (v) geographical coordinates, altitude and burial depth, together with the derived cosmic dose rates[2] (unless gamma and cosmic dose rates were measured directly using e.g. Al_2O_3:C pellets). In some cases, sediment may be rich in organic matter or carbonates; these may have changed through time, perhaps by oxidation (organic material) or by the formation of secondary carbonates in pore spaces. This leads to complexities resulting from sediment chemical composition; since quartz is the dosimeter, differential absorption of dose in the surrounding non-quartz material renders the infinite matrix assumption invalid, or at least approximate. If the amount of organic or carbonate material is quantified, differential dose rate absorption coefficients may then be used [47], and reported. Table S5 below gives attenuation factors to account for the effect of water and carbonates in infinite matrix conditions, while Table S6 details variations of the water correction factors in well-sorted sediment as a function of grain size.

To illustrate our suggestions, we provide Table S7(a,b); this represents our view of the minimum numerical reporting that allows the transparency required. The various underlying assumptions and the factors used should be given in the main text or as footnotes, together with any other relevant data (particularly the dose recovery summary).

For the reader to follow the details of an age calculation, and understand how the various effects and parameters are taken into account in practice, an age calculation spreadsheet is provide as Supplementary Material. This is not proposed as a standard data processing option (there are many more sophisticated software packages available) but it does provide a transparent and practical

[2] The age calculation spreadsheet provided here allows the calculation of cosmic dose rates as a function of latitude, altitude and burial depth following [3].

implementation of age calculation, parameterized functions to estimate cosmic dose rates and correction factors for the effect of water, grain size attenuation factors, etc.

(a) Uncertainty analysis of luminescence data follows guidelines such as those of the *Bureau International des Poids et Mesures* (the intergovernmental organisation through which Member States act together on matters related to measurement science and measurement standards). The Bureau's guide on the expression of uncertainty in measurement distinguishes between random and systematic uncertainties [50]. The measurement error is defined as the difference between the measured, or observed value, and the true value (measurand); it is unknown (since the true value is unknown) but it can be characterised by a probability density. Repetition of a measurement leads to random fluctuations of the observed values (and thus characterises random uncertainties), while the use of a given instrument, calibrated with a given standard, my lead to systematic bias in measurements. In other words, the scale of analysis dictates whether an uncertainty is random or systematic - for example, uncertainties that are systematic within each of several laboratories (e.g. calibration of a gamma spectrometer), will give rise to random fluctuations at the scale of an intercomparison study involving different laboratories (Table S8).

In both cases (systematic and random), provided everything has been done to reduce systematic uncertainties, both systematic and random errors may be assumed to follow a normal distribution. Table S8 lists the main parameters needed to calculate an OSL age (other than measurement uncertainties, which can, in principle, be reduced arbitrarily by simply making more measurements) and the typical standard deviation of the error, as well as comments on its nature (systematic or random).

Formally, one may write for all quantities at stake:

$$\tilde{x} = x + e$$

where $\tilde{x}$ is the measurement or observed value, x the true value and e the measurement error. We then introduce σ, the standard deviation of e (and $\tilde{x}$). For example, if we measure the equivalent dose on n aliquots, we generally approximate σ by the standard deviation of the D_e values, divided by the square root of n. Many quantities must be determined and added, multiplied or divided to finally obtain an age; for uncertainty propagation, if $z = x + y$ (or $z = x - y$), it is standard practice to approximate σ_z by $\sqrt{\sigma_x^2 + \sigma_y^2}$. If $z = y/x$ (or $z = yx$), then $\frac{\sigma_z}{z}$ is approximated by $\sqrt{\left(\frac{\sigma_x}{x}\right)^2 + \left(\frac{\sigma_y}{y}\right)^2}$.

Although there is no formal convention, OSL ages are almost exclusively reported with an uncertainty of one standard deviation of the error, i.e. the interval $[A - \sigma_A; A + \sigma_A]$ is the 68% confidence interval.

Figure S1. Cosmic dose rate as a function of burial depth (left) and altitude (right) (based on [3]).

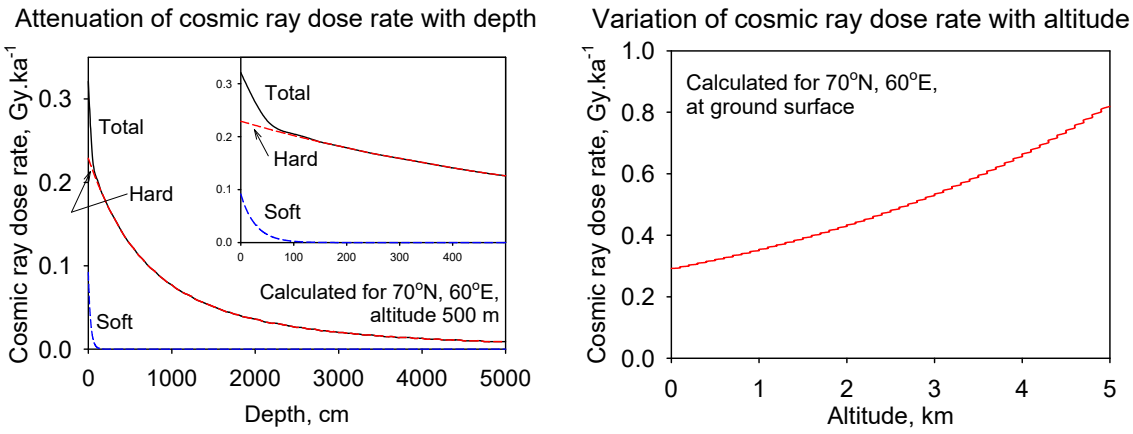

Figure S2. Schematic overview of the laboratory treatment to extract quartz grains from the sample. All these steps should be performed under subdued lighting conditions (using light of wavelength and intensity without a significant effect on the trapped charge population [51]). Q: quartz, H: heavy minerals, F: feldspar, NF: sodium-rich feldspar, KF: potassium-rich feldspar. The combined water drops [💧] and fan symbol [✲] indicate thorough washing and drying.

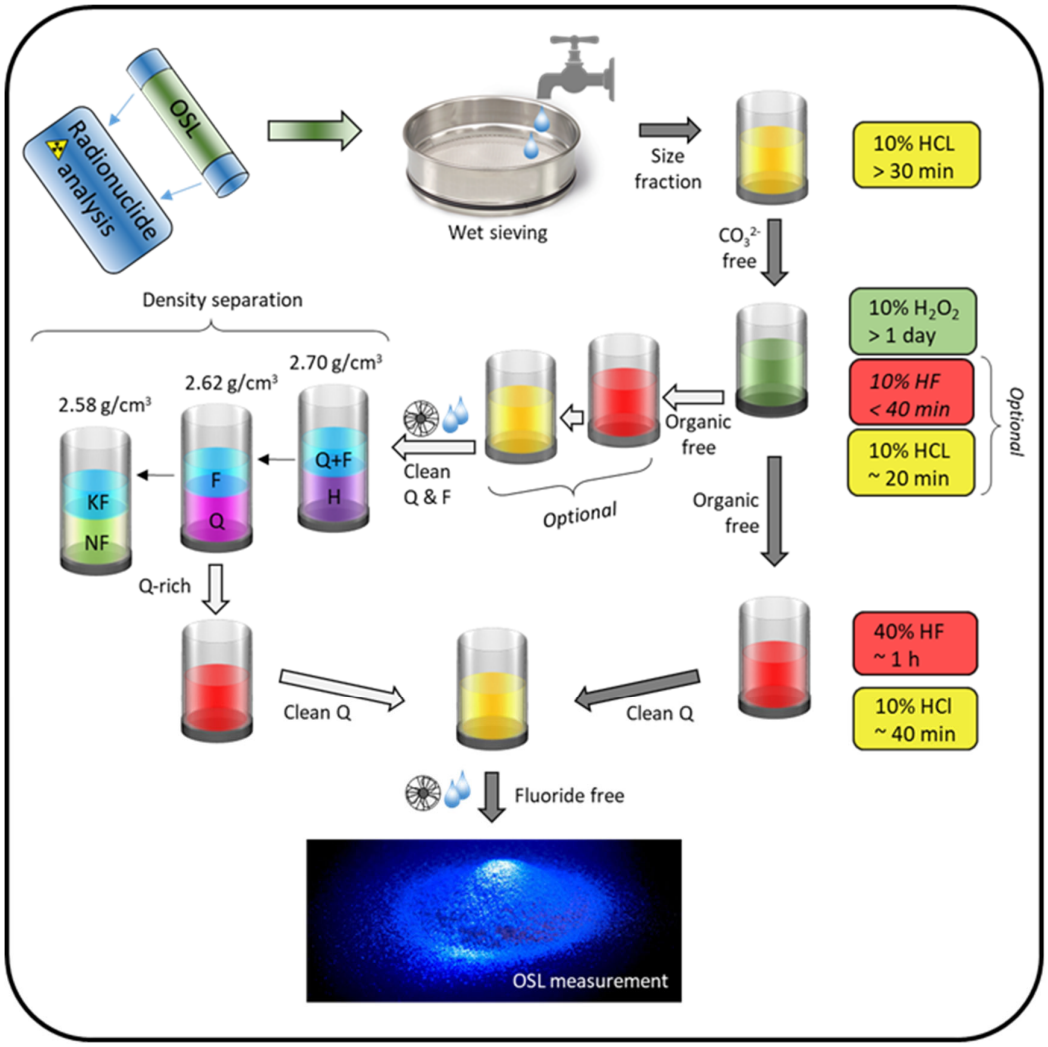

Figure S3. Radioactive decay chains of ^{238}U (left) and ^{232}Th (right). Long-lived radioisotopes of the same element are marked with rings of one colour. In secular equilibrium, the activity of each radionuclide is almost identical and follows the parent decay rate. While the ^{232}Th chain is unlikely to suffer from disequilibria (because of the short half lives of all of its progeny), the ^{238}U chain may be affected by ^{222}Rn escape (^{222}Rn is a gas and the half-life of several days makes it possible for it to move before decaying), or by loss or gain of ^{226}Ra and ^{238}U – both elements can be mobilised or deposited by changes in porewater geochemistry (e.g. salinity, dissolved carbonate, reduction/oxidation conditions).

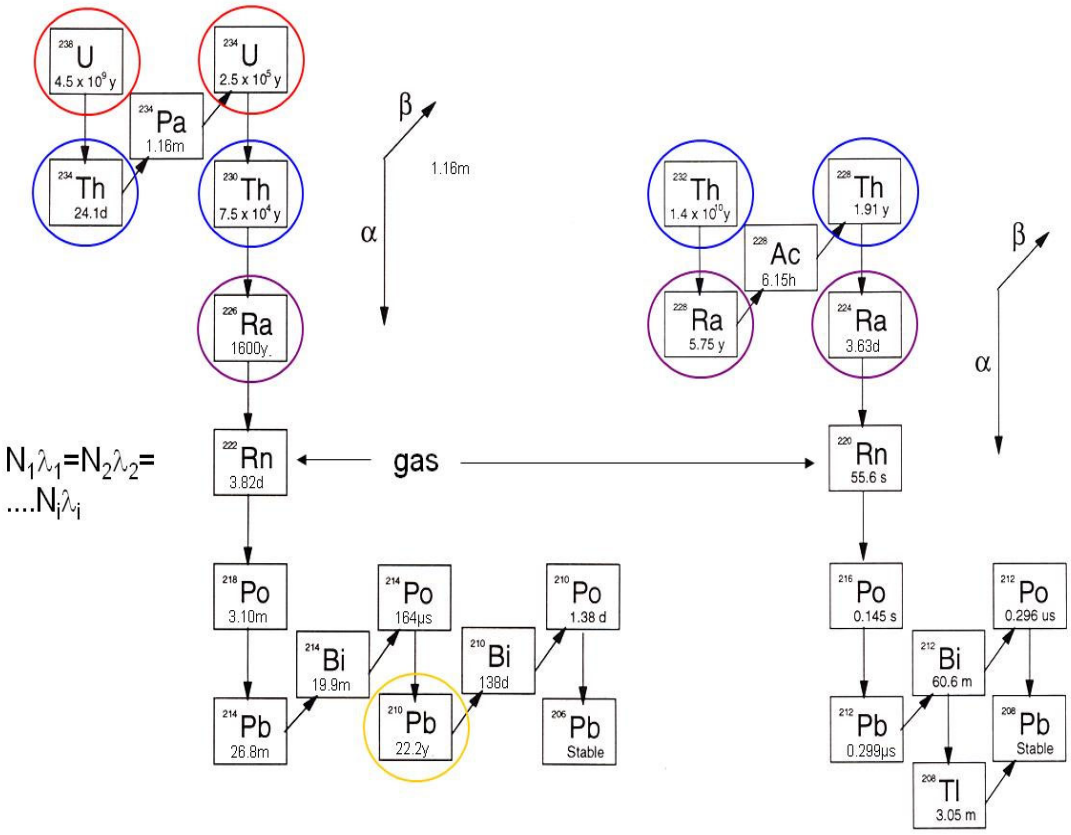

Figure S4. The radionuclides in the decay series are combined in groups reflecting the presumed potential for disequilibria based on half-lives and physico-chemical parameters (nuclides within each group can be deduced by comparison with Figure S3). The relative contribution of these groups to the total dose rate for a sand sample with the activities given in Table S2 is shown as %; these values can give some indication of the potential importance of radioactive disequilibria (bearing in mind that this is most likely to occur in the U series). Unless sediment is unusually rich in U (relative to K and Th), the contribution of the U series to the total dose rate is sufficiently small for most samples to make unlikely errors of more than 5% in the final age arising from disequilibrium.

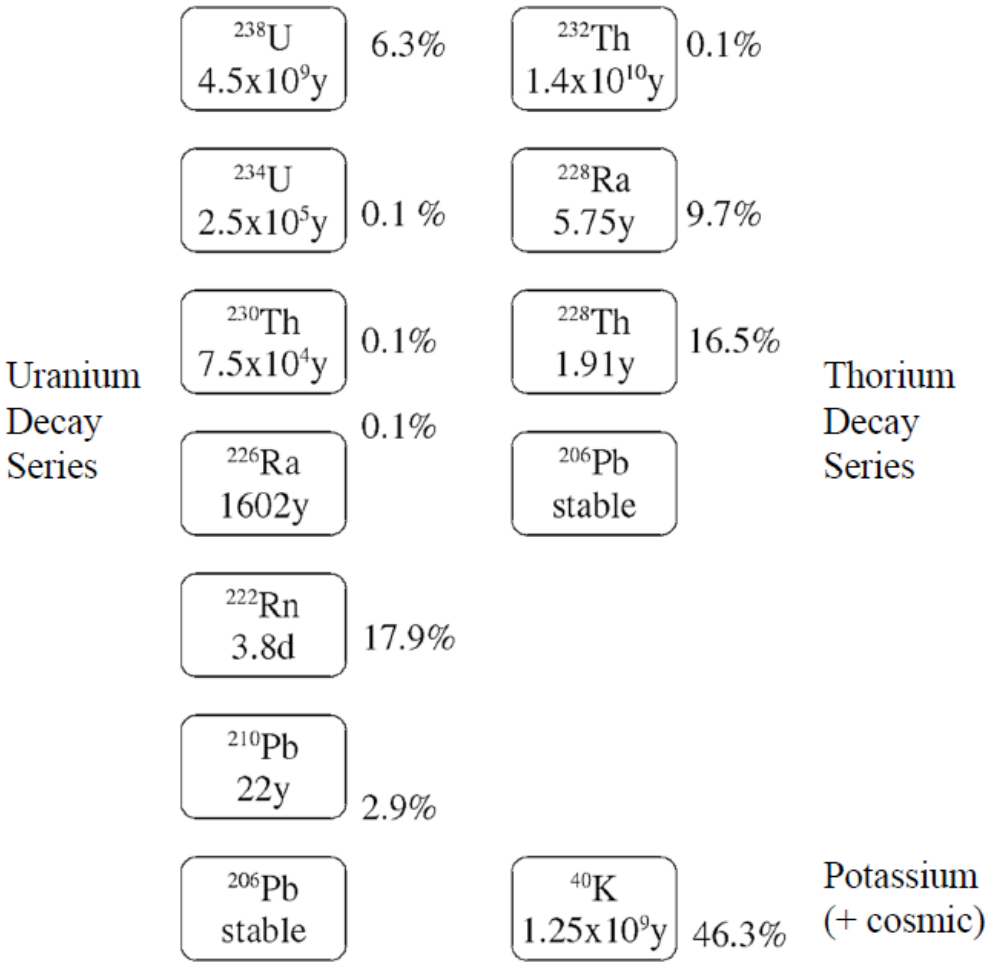

Figure S5 (reproduced from [52]). Variability in radionuclide concentrations in 3578 samples used for luminescence dating. Left – histograms of activity concentrations of ^{238}U (a), ^{226}Ra (b), ^{232}Th (c) and ^{40}K (d). Right – relative contributions to beta (a) and gamma (b) dose rates from ^{238}U, ^{232}Th and ^{40}K. The table summarises the concentration values.

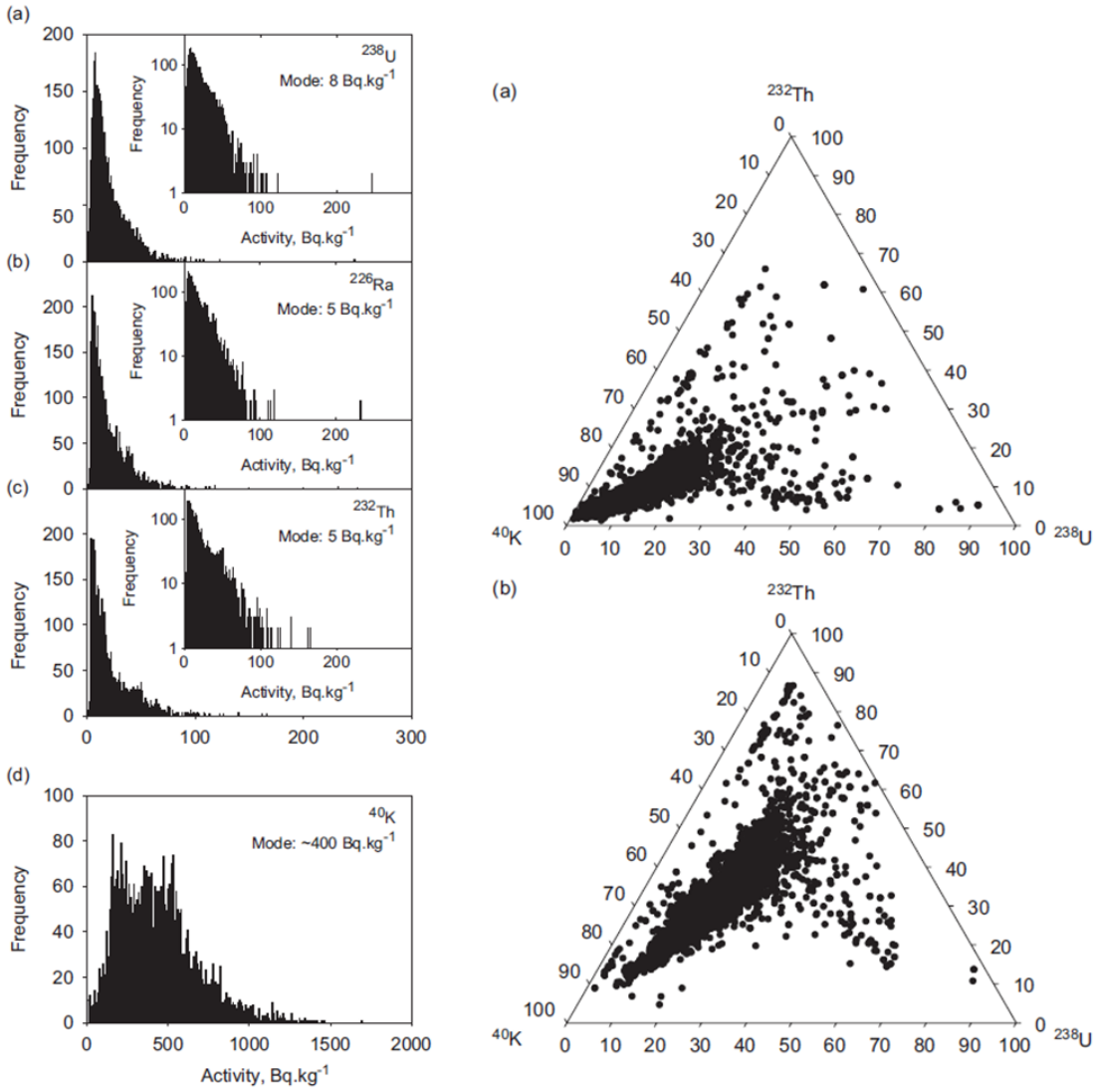

Mode, percentiles and median for the distributions of concentrations of ^{238}U, ^{226}Ra, ^{232}Th and ^{40}K in 3758 samples

	^{238}U	^{226}Ra	^{232}Th	^{40}K
Mode, Bq kg^{-1}	8	5	4	355
0.01-percentile, Bq kg^{-1}	0.20	2.72	2.84	40
Median, Bq kg^{-1}	15.30	14.35	15.34	406
0.99-percentile, Bq kg^{-1}	90.37	86.69	150.4	1182

Figure S6. Examples of heterogeneous dose rate distributions at the Palaeolithic site of Roc de Marsal [53, 54].

a) Gamma dose rates. The stratigraphic section (left panel) comprises sediment between two calcareous rocky horizons: bedrock at the bottom and collapsed rocks from the cave roof on top; the right panel is a schematic view of the section. The graph (inset) illustrates that gamma dose rates measured in situ with Al_2O_3:C dosimeters show large variations, because the limestone contains very low radionuclide concentrations compared to the sediment. In such cases, dating the sediment at or close to the interface requires careful assessment of the gamma dose rate.

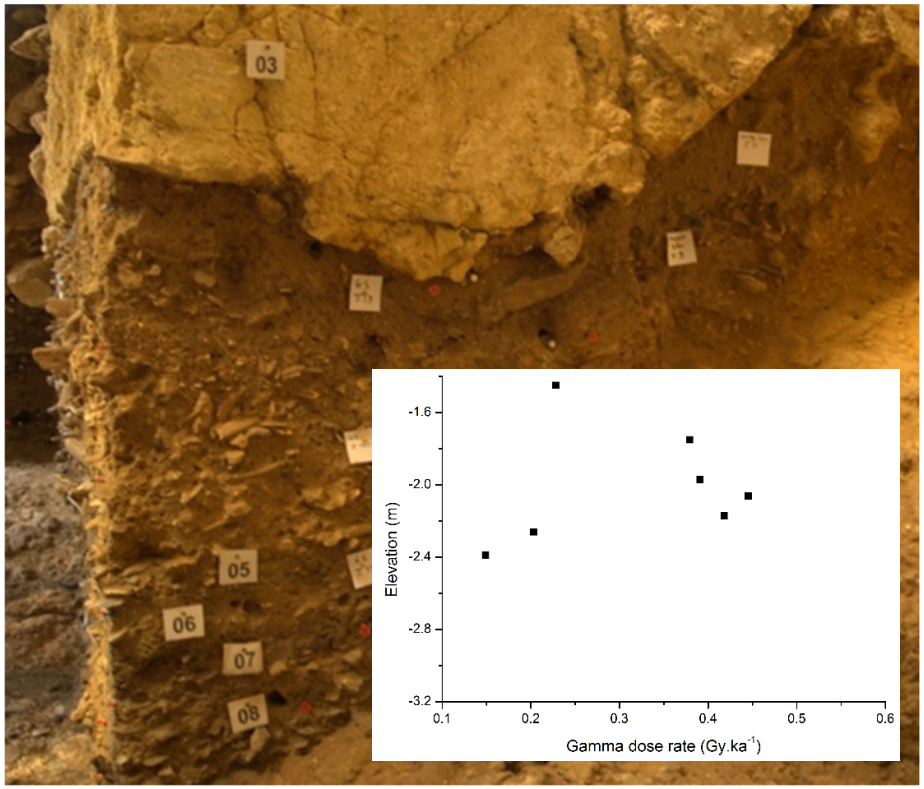

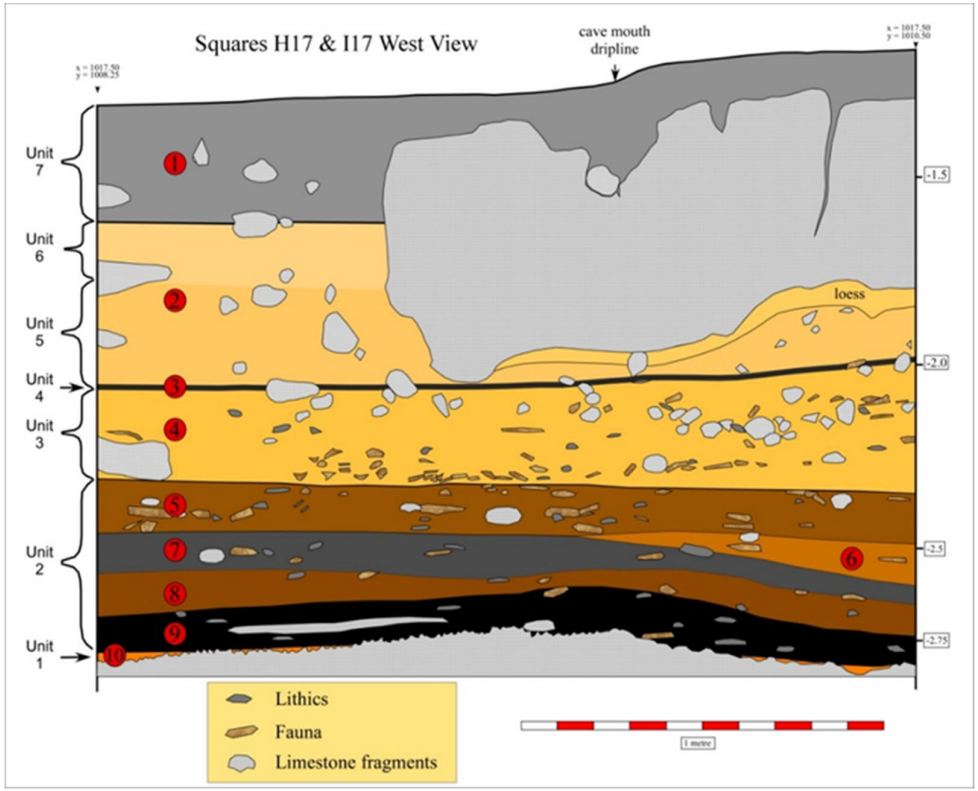

b)

b) Beta dose rates. Beta autoradiography [55] (right panel) allows qualitative estimation of dose rate heterogeneities. In the example shown here, the limestone gravel and effects of dissolution ('Loose brown patch') shown in left panel induce large variations in beta dose rates (right panel). 'Hotspots' appear in the form of small dark circular patches on the right image, in this case presumably K-feldspar grains. Generally low dose rates, poor sorting and coarser grain size distributions tend to indicate greater variability in dose rates [56, 57, 58, 59].

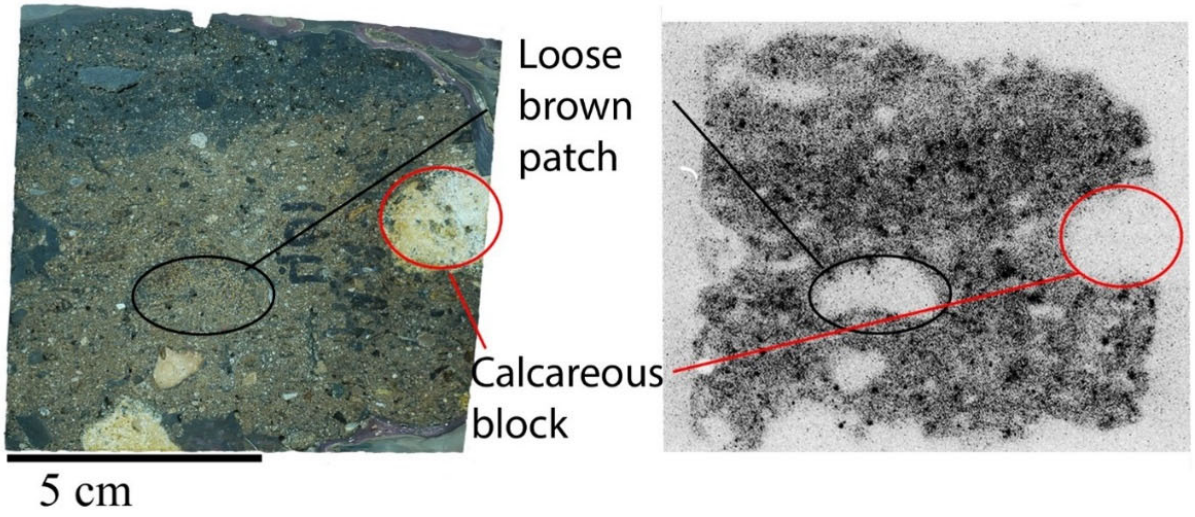

Figure S7. The main components in an OSL measurement system.

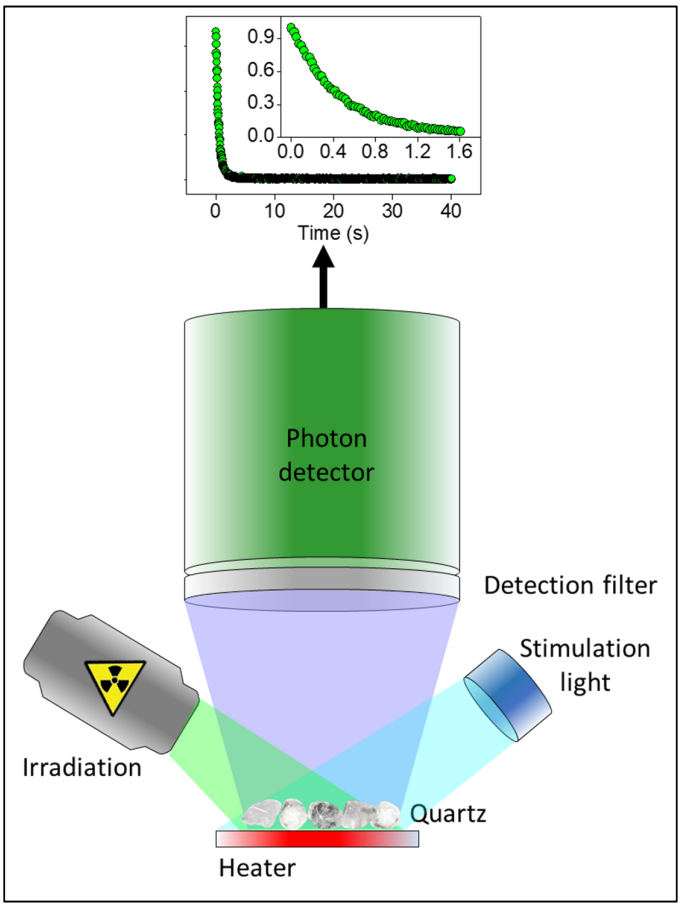

Figure S8. Emission spectra of several sedimentary quartz samples from South Australia obtained using stimulation at 647 nm (reproduced from *[60]*).

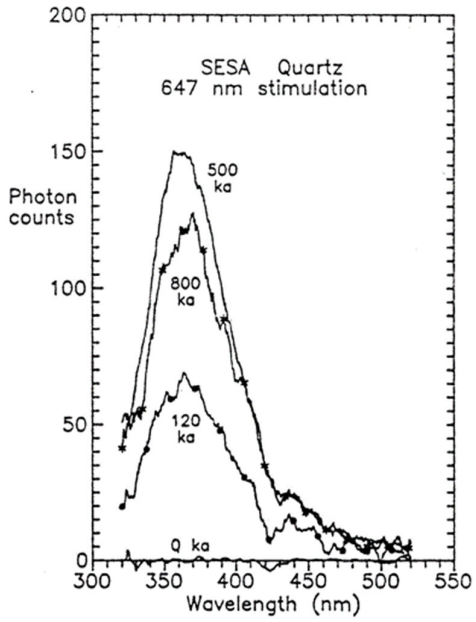

Figure S9. Detection: transmission of 7.5 mm of Hoya U-340 detection filter; Emission: Quartz OSL; Stimulation: emission spectra of typical blue and green LEDs. Cut-off filters: Typical cut-off filters used in front of blue and green stimulation LEDs to more effectively separate the stimulation light from the detection window.

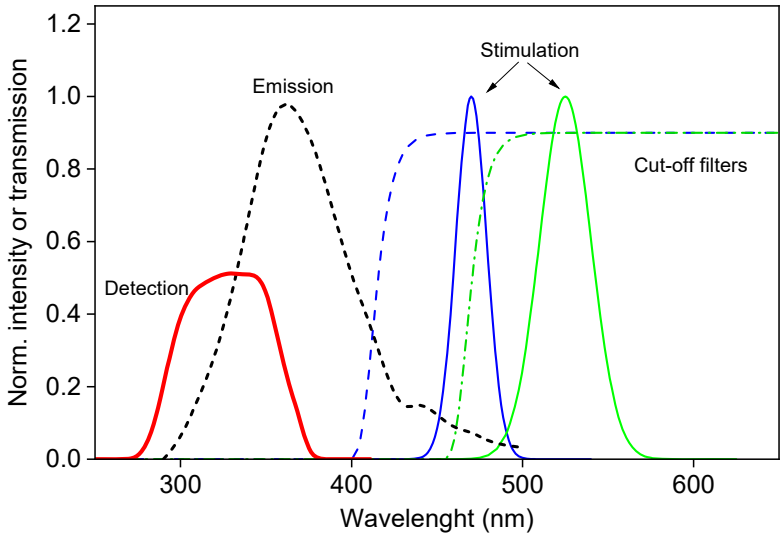

Figure S10. Optical stimulation (excitation) spectrum for a sedimentary quartz annealed at 850°C and detected through the Hoya U-340 glass filter. Reproduced from *[61]*.

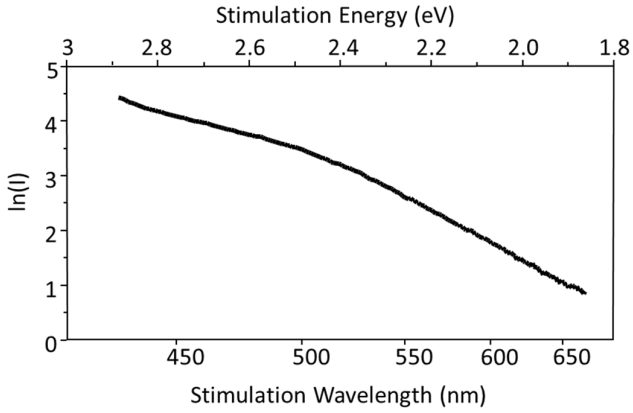

Table S1. Methods for the determination of dose rates. Where relevant (marked with a * below), it is usually desirable to ensure that ^{222}Rn is in equilibrium with its parent ^{226}Ra before measurement.

Method	Output	Comment	References
High-resolution gamma spectrometry*	[K], [U], [Th]	Allows some investigation of disequilibrium. Depending on detector, requires >10 g of sample.	[44], [62], [63]
Low-resolution gamma spectrometry*	[K], [U], [Th]	Slightly less sensitive than high resolution, but does not require cooling. Typically ~200 g sample	[64]
Beta counting*	Beta activity concentration	Conversion from count rate to dose rate is radionuclide dependent. Requires 10s of g sample.	[52], [65]
Alpha counting*	Alpha activity concentration	^{222}Rn difficult to control; lithium borate glassification can be used to ensure homogeneity	[4]; [66]
ICP-MS (Inductively Coupled Plasma-Mass Spectrometry), or OES (Optical Emission Spectrometry) for K	[K], [U], [Th]	Only a few hundred mg of material analysed, so homogenisation is of great importance.	[67] [68]
NAA (Neutron Activation Analysis)	[K], [U], [Th]	Only a few hundred mg of material analysed, so homogenisation is of great importance.	[69] [70]
In situ dosimeters	Gamma and cosmic dose rate at sample location	Requires long storage time on site (6-12 months). Useful in heterogeneous settings at the dm- or m-scale.	[8] [9] [71]
Field gamma spectrometer	effective [K], [U], [Th], or direct gamma dose rate at sample location	Useful when working in heterogeneous settings at the dm- or m-scale.	[12], [13]; [10]; [11]

Table S2. Energy release and dose rates in a) the ^{232}Th decay series, and b) the Uranium (^{238}U and ^{235}U) decay series, and c) Potassium (^{40}K) and Rubidium (^{87}Rb; only beta dose rates). Adapted from [6]

a) ^{232}Th decay series.

Isotope	Half-life (s)	Alpha		Beta		Gamma	
		E	DR	E	DR	E	DR
^{232}Th	$4.43\ 10^{17}$	4.003	0.0821	0.0113	0.0002	0.0011	0.0000
^{228}Ra	$1.81\ 10^{8}$	-	-	0.0092	0.0002	0.0004	0.0000
^{228}Ac	$2.21\ 10^{4}$	-	-	0.4171	0.0086	0.8602	0.0176
^{228}Th	$6.03\ 10^{7}$	5.406	0.1109	0.0195	0.0004	0.0031	0.0001
^{224}Ra	$3.16\ 10^{5}$	5.673	0.1164	0.0023	0.0000	0.0104	0.0002
^{220}Rn	$5.56\ 10^{1}$	6.288	0.1290	-	-	0.0006	0.0000
^{216}Po	$1.45\ 10^{-1}$	6.778	0.1390	-	-	0.0000	0.0000
^{212}Pb	$3.83\ 10^{4}$	-	-	0.1721	0.0035	0.1437	0.0029
^{212}Bi	$3.63\ 10^{3}$	2.175	0.0446	0.5034	0.0103	0.1039	0.0021
^{212}Po (0.641)	$2.99\ 10^{-4}$	5.631	0.1155	-	-	-	-
^{208}Tl (0.359)	$1.83\ 10^{2}$	-	-	0.2140	0.0044	1.2136	0.0249
total			**0.7375**		**0.0277**		**0.0479**
Pre-Rn total			**0.3093**		**0.0094**		**0.0180**

Notes.

1. Energies ("E) are given in MeV and represent the energy emitted per disintegration.
2. Branching ratios are shown in parenthesis against the radioelements in the branches; associated values given for energy release are after adjustment for branching. Note that the branching also affects the energy release of the radioelement at which the branching occurs; thus the value given for the alpha release by ^{212}Bi is 35.9% of the full energy - because ^{208}Tl is formed by alpha emission from ^{212}Bi.
3. Beta components include Auger electrons and internal conversion; gamma components include X-rays and annihilation radiation; alpha recoil and neutrinos are not included due to their insignificant contribution to dose-rates (cf. [72]).
5. A dash indicates that no radiation of that type is mentioned by the National Nuclear Data Centre.
6. Dose rate values ("DR") are given in Gy.ka^{-1} per ppm of parent (i.e. mg of parent per kg of sample), assuming equilibrium in the decay chains. The activity of the parent is 4.057 Bq per kg of sample.
7. The rows labelled 'pre-Rn' give the values for 100% escape of radon.
8. Relative differences are calculated between this paper and values from [72].
9. ^{216}At has been omitted since its contribution to the total energy is insignificant.

Table S2 continued.

b) Uranium (^{238}U and ^{235}U) decay series.

Isotope	Half-life (s)	Alpha			Beta			Gamma		
		E	DR	DR, nat. U	E	DR	DR, nat. U	E	DR	DR, nat. U
^{238}U	$1.41\ 10^{17}$	4.193	0.264	0.262	0.007	0.0005	0.0004	0.001	0.0001	0.0001
^{234}Th	$2.08\ 10^{6}$	-	-	-	0.059	0.0037	0.0037	0.008	0.0005	0.0005
^{234}Pa$_m$	$6.95\ 10^{1}$	-	-	-	0.810	0.0509	0.0506	0.016	0.0010	0.0010
^{234}Pa (0.0016)	$2.41\ 10^{4}$	-	-	-	0.001	0.0001	0.0001	0.001	0.0001	0.0001
^{234}U	$7.75\ 10^{12}$	4.759	0.299	0.297	0.012	0.0007	0.0007	0.001	0.0001	0.0001
^{230}Th	$2.38\ 10^{12}$	4.664	0.293	0.291	0.013	0.0008	0.0008	0.001	0.0001	0.0001
^{226}Ra	$5.05\ 10^{10}$	4.775	0.300	0.298	0.004	0.0002	0.0002	0.007	0.0005	0.0005
^{222}Rn	$3.30\ 10^{5}$	5.489	0.345	0.343	-	-	-	0.000	0.0000	0.0000
^{218}Po	$1.86\ 10^{2}$	6.001	0.377	0.375	-	-	-	-	-	-
^{214}Pb	$1.61\ 10^{3}$	-	-	-	0.291	0.0183	0.0182	0.239	0.0150	0.0149
^{214}Bi	$1.19\ 10^{3}$	0.001	0.000	0.000	0.654	0.0411	0.0408	1.475	0.0928	0.0921
^{214}Po	$1.64\ 10^{-4}$	7.687	0.483	0.480	-	-	-	0.000	0.0000	0.0000
^{210}Pb	$7.01\ 10^{8}$	-	-	-	0.033	0.0021	0.0021	0.005	0.0003	0.0003
^{210}Bi	$4.33\ 10^{5}$	-	-	-	0.389	0.0245	0.0243	-	-	-
^{210}Po	$1.20\ 10^{7}$	5.304	0.333	0.331	0.000	0.0000	0.0000	0.000	0.0000	0.0000
^{238}U total			2.695	2.676		0.1429	0.1419		0.1104	0.1096
^{238}U Pre-Rn total			1.156	1.148		0.0570	0.0566		0.0022	0.0022
^{235}U	$2.22\ 10^{16}$	4.114	1.663	0.012	0.029	0.0117	0.0001	0.164	0.0665	0.0005
^{231}Th	$2.20\ 10^{6}$	-	-	-	0.146	0.0591	0.0004	0.023	0.0094	0.0001
^{231}Pa	$1.03\ 10^{12}$	4.924	1.990	0.014	0.032	0.0130	0.0001	0.040	0.0160	0.0001
^{227}Ac	$6.87\ 10^{8}$	0.070	0.028	0.000	0.012	0.0049	0.0000	0.001	0.0002	0.0000
^{227}Th (0.986)	$1.61\ 10^{6}$	5.808	2.347	0.017	0.050	0.0202	0.0001	0.154	0.0621	0.0004
^{223}Fr (0.014)	$1.32\ 10^{3}$	0.005	0.002	0.000	0.000	0.0002	0.0000	0.001	0.0003	0.0000
^{223}Ra	$9.88\ 10^{5}$	5.664	2.289	0.016	0.068	0.0275	0.0002	0.135	0.0546	0.0004
^{219}Rn	$3.96\ 10^{0}$	6.753	2.729	0.019	0.007	0.0027	0.0000	0.058	0.0235	0.0002
^{215}Po	$1.78\ 10^{-3}$	7.392	2.987	0.021	-	-	-	-		
^{211}Pb	$2.17\ 10^{3}$	-	-	-	0.450	0.1817	0.0013	0.064	0.0258	0.0002
^{211}Bi	$1.28\ 10^{2}$	6.549	2.647	0.019	0.013	0.0053	0.0000	0.047	0.0191	0.0001
^{211}Po	$5.16\ 10^{-1}$	0.021	0.008	0.000	-	-	-	-	-	-
^{207}Tl	$2.86\ 10^{2}$	-	-	-	0.495	0.2002	0.0014	0.002	0.0009	0.0000
^{235}U total			16.690	0.1185		0.5265	0.0037		0.2807	0.0020
total				**2.795**			**0.1457**			**0.1116**
Pre-Rn total				**1.267**			**0.0603**			**0.0042**

Notes.

1. See notes 1-8 of Table S2(a).

2. The mass abundances used in the natural Uranium calculations for ^{238}U and ^{235}U (respectively 99.29% and 0.71%) correspond to the natural atomic abundances of 99.28% and 0.72% respectively.

3. The activity of the parent (per ppm of parent) is 12.44 Bq per kg of sample for ^{238}U, 79.94 for ^{235}U and 12.92 for natural Uranium.

4. The rows labelled 'pre-Rn' give the values for 100% escape of radon in the case of ^{238}U series, but because of the short half-life of ^{219}Rn the values given for natural Uranium include contributions of that gas and its daughters.

5. ^{218}At, ^{218}Rn, ^{210}Tl, ^{206}Tl and ^{215}At have been omitted since their contribution to the total is insignificant.

Table S2 continued.

c) Dose-rate data for Potassium and Rubidium.

		^{40}K	^{87}Rb
Natural abundance (mg.g^{-1})		0.119	283
Half-life (Ga)		1.248	48.1
Average energy per disintegration (MeV)	Beta	0.499	0.0817
	Gamma	0.1557	
Specific activity (Bq.kg^{-1}) for concentration of 1% nat. K and 50 ppm of nat. Rb	Total	316.4	44.8
	Beta	282.5	44.8
	Gamma	33.73	
Dose-rate (Gy.ka^{-1}) for concentrations as above	Beta	0.7982	0.0185
	Gamma	0.2491	

Notes.

1. The energy given for Potassium is that released per disintegration, i.e. after allowance for branching between beta and gamma (89.28% and 10.72% respectively).
2. The contents given in row 1 correspond to natural atomic abundances of 116.7 ppm and 27.8%.

Table S3. Typical concentrations of radionuclides in a well-sorted sand, and the derived infinite matrix dose rates (without grain size attenuation taken into account). In this case, ^{40}K alone contributes about 55% to the total, and the gamma dose rate about 35%.

Radio-nuclide	Activity $Bq.kg^{-1}$	Concentration	Beta dose rate, $Gy.ka^{-1}$	Gamma dose rate, $Gy.ka^{-1}$
^{40}K	300	~1%	0.76	0.24
^{238}U	20	~1.5 ppm	0.23	0.17
^{232}Th	20	~5 ppm	0.14	0.24
		Total:	1.12	0.65

Table S4. Beta self-dose values (φ) used to derive attenuation factors (1- φ) following the superposition theorem [73]. Values were calculated with Geant4 for the ^{232}Th decay series, the Uranium (^{238}U and ^{235}U) decay series (all in secular equilibrium), and ^{40}K, for two different minerals: quartz and potassium feldspar.

GEANT4						
Grain size (ø, µm)	Potassium		Uranium		Thorium	
	Quartz (d=2.65 g.cm^{-3})	$KAlSi_3O_8$ (d=2.60 g.cm^{-3})	Quartz (d=2.65 g.cm^{-3})	$KAlSi_3O_8$ (d=2.60 g.cm^{-3})	Quartz (d=2.65 g.cm^{-3})	$KAlSi_3O_8$ (d=2.60 g.cm^{-3})
20	0.007	0.007	0.038	0.037	0.048	0.047
40	0.014	0.014	0.057	0.056	0.077	0.075
60	0.022	0.021	0.072	0.07	0.098	0.097
80	0.029	0.028	0.084	0.082	0.117	0.115
100	0.037	0.035	0.095	0.093	0.134	0.131
120	0.044	0.042	0.105	0.103	0.149	0.146
140	0.052	0.05	0.115	0.113	0.163	0.16
160	0.059	0.057	0.125	0.122	0.176	0.173
180	0.067	0.064	0.134	0.131	0.188	0.185
200	0.075	0.072	0.143	0.14	0.2	0.196
250	0.095	0.091	0.165	0.161	0.225	0.221
300	0.114	0.11	0.185	0.181	0.247	0.243
400	0.154	0.148	0.223	0.217	0.286	0.281
600	0.231	0.223	0.289	0.282	0.35	0.343
800	0.304	0.294	0.346	0.338	0.403	0.395
1000	0.372	0.36	0.395	0.387	0.449	0.441

Table S5. Water and carbonate correction factors for a) beta radiation and b) gamma radiation. Reproduced from [47].

a) The water and carbonate correction factors for beta radiation.

Water content (m_w/m_s)	Carbonate content (m_c/m_s)							
	0		0.04		0.20		1.00	
0	–		K	0.99	K	0.99	K	0.99
			Th	0.99	Th	0.99	Th	0.99
			U	0.99	U	0.99	U	0.99
0.04	K	1.19	K	1.09	K	1.03	K	1.00
	Th	1.20	Th	1.09	Th	1.03	Th	1.00
	U	1.19	U	1.09	U	1.02	U	1.00
0.20	K	1.20	K	1.16	K	1.09	K	1.02
	Th	1.20	Th	1.17	Th	1.09	Th	1.02
	U	1.20	U	1.16	U	1.09	U	1.02
1.00	K	1.19	K	1.18	K	1.15	K	1.09
	Th	1.19	Th	1.18	Th	1.16	Th	1.09
	U	1.19	U	1.18	U	1.15	U	1.08

The water and carbonate content of the sediment is given as mass (m_w and m_c, respectively) per mass sediment (m_s). The factures are tabulated for independent determination of water and carbonate. The use of these tables requires the assessment of the mass of the *dry* sediment (the fraction having no water or carbonate). It is suggested that intermediate values are calculated using log interpolation.

b) The water and carbonate correction factors for gamma radiation.

Water content (m_w/m_s)	Carbonate content (m_c/m_s)							
	0		0.04		0.20		1.00	
0	–		K	1.02	K	1.02	K	1.01
			Th	1.04	Th	1.04	Th	1.03
			U	1.04	U	1.04	U	1.04
0.04	K	1.06	K	1.04	K	1.03	K	1.02
	Th	1.02	Th	1.03	Th	1.04	Th	1.03
	U	1.02	U	1.03	U	1.04	U	1.04
0.20	K	1.06	K	1.05	K	1.04	K	1.02
	Th	1.02	Th	1.02	Th	1.03	Th	1.03
	U	1.01	U	1.02	U	1.03	U	1.04
1.00	K	1.04	K	1.04	K	1.04	K	1.04
	Th	0.99	Th	0.99	Th	1.00	Th	1.03
	U	0.98	U	0.98	U	1.01	U	1.03

The water and carbonate content of the sediment is given as mass (m_w and m_c, respectively) per mass sediment (m_s).

Table S6 (reproduced from [48]). Water correction factors for gamma radiation obtained using Monte Carlo simulations for the three radioelements found in sediments, as a function of the packing system and grain size.

Grain radius (μm)	Cubic simple			Body-centred cubic			Face-centred cubic		
	K	U	Th	K	U	Th	K	U	Th
20	1.181 *0.002*	1.157 *0.017*	1.164 *0.019*	1.194 *0.008*	1.176 *0.030*	1.185 *0.034*	1.205 *0.002*	1.193 *0.034*	1.188 *0.032*
40	1.165 *0.002*	1.132 *0.016*	1.137 *0.019*	1.184 *0.010*	1.160 *0.027*	1.163 *0.027*	1.198 *0.002*	1.176 *0.027*	1.173 *0.033*
60	1.154 *0.003*	1.112 *0.015*	1.118 *0.021*	1.177 *0.011*	1.152 *0.024*	1.167 *0.022*	1.189 *0.003*	1.165 *0.032*	1.169 *0.038*
80	1.146 *0.003*	1.102 *0.014*	1.105 *0.017*	1.170 *0.013*	1.134 *0.024*	1.137 *0.017*	1.177 *0.003*	1.138 *0.030*	1.153 *0.031*
100	1.140 *0.003*	1.086 *0.014*	1.104 *0.019*	1.164 *0.014*	1.128 *0.025*	1.139 *0.032*	1.173 *0.003*	1.139 *0.029*	1.154 *0.045*
150	1.131 *0.003*	1.071 *0.017*	1.085 *0.016*	1.154 *0.016*	1.113 *0.027*	1.127 *0.036*	1.162 *0.004*	1.116 *0.032*	1.137 *0.030*
200	1.124 *0.004*	1.061 *0.015*	1.074 *0.016*	1.144 *0.018*	1.094 *0.022*	1.106 *0.028*	1.156 *0.004*	1.095 *0.031*	1.111 *0.038*
300	1.115 *0.005*	1.058 *0.015*	1.073 *0.017*	1.137 *0.02*	1.086 *0.025*	1.095 *0.027*	1.147 *0.005*	1.101 *0.032*	1.107 *0.033*
400	1.109 *0.005*	1.044 *0.014*	1.054 *0.017*	1.129 *0.023*	1.082 *0.023*	1.087 *0.035*	1.148 *0.005*	1.106 *0.029*	1.112 *0.038*
500	1.106 *0.006*	1.042 *0.017*	1.053 *0.016*	1.127 *0.025*	1.062 *0.022*	1.082 *0.031*	1.143 *0.006*	1.088 *0.029*	1.084 *0.031*

Table S7. Example tables containing suggested minimum information that should be presented in a publication containing quartz OSL luminescence ages.

a)

Lab.code	^{238}U, Bq.kg^{-1}	^{226}Ra, Bq.kg^{-1}	^{232}Th, Bq.kg^{-1}	^{40}K, Bq.kg^{-1}	*beta dose rate, Gy.ka^{-1}	*gamma dose rate, Gy.ka^{-1}
1	51 ± 12	46.0 ± 1.2	61.0 ± 1.2	562 ± 20	2.29 ± 0.06	1.48 ± 0.04
2	72 ± 12	48.2 ± 1.1	60.6 ± 1.2	566 ± 16	2.32 ± 0.05	1.50 ± 0.04
3	58 ± 9	45.2 ± 0.9	60.2 ± 1.0	581 ± 13	2.33 ± 0.05	1.48 ± 0.04
4	46 ± 8	43.8 ± 0.8	32.2 ± 0.8	158 ± 8	1.05 ± 0.04	0.81 ± 0.04

Note: * dry infinite matrix dose rates

b)

Lab.code	Site	Depth, cm	w.c. %	OSL D_e, Gy	(n_r)	(n_a)	Total dose rate, Gy/ka	OSL age, ka
1	Test site-A	65	16	95 ± 4	1	23	3.16 ± 0.16	30.0 ± 2.0
2	Test site-B	65	16	73 ± 4	0	12	3.19 ± 0.16	22.9 ± 1.7
3	Test site-C	65	16	107 ± 6	0	24	3.20 ± 0.16	33.5 ± 2.5
4	Test site-C	30	11	43 ± 2	1	35	1.79 ± 0.09	23.9 ± 1.7

Note: (a) Mean grain size 215µm. (b) Site altitude 0 km. (c) w.c.: water content. (d) n_r, n_a : number of rejected and accepted aliquots, respectively.

Table S8. Typical dose rate uncertainty budget for a 50 ka sample with dose rate of 2 Gy.ka^{-1} (neglecting sample measurement uncertainties). Dose rate derived from gamma spectrometry measurements of K,U,Th.

	¤Est. Relative Uncertainty %	Absolute uncertainty, ka	Nature of uncertainty when ages compared with:		
			#OSL ages from same section	#OSL ages from other sites	Non-OSL ages
Saturation water content	2	1	Usually ***Random***, (but likely ***Systematic*** if same grain-size distribution in all samples)	***Random***	***Random***
Fraction of saturation	4	2	***Random*** (assumed values for each sample chosen independently of each other) and/or ***Systematic*** (e.g. if site was wetter than assumed).	***Random***	***Random***
Gamma spectrometer calibration	2	1	#***Systematic*** for a single spectrometer (but each spectrometer has its own uncertainty on the counting of the calibration standards)	***Systematic*** for a single gamma spectrometer (but see cell to left)	***Systematic*** for a single gamma spectrometer (but see cell to left)
Conversion - activity to dose rate	2	1	***Systematic***	***Systematic***	***Systematic***
Beta source calibration	2	1	#***Systematic*** for a single source (but each source has its own uncertainty on measurement of the known-dose standard)	***Systematic*** for a single source (but see cell to left)	***Systematic*** for a single source (but see cell to left)
Cosmic ray uncertainty	0.02 Gy.ka^{-1}*	0.5	***Systematic*** for given elevation, relative depth and latitude.	***Random*** (unknown depth variation between sites)	***Random***
Beta attenuation factor	2	1	***Systematic***	***Systematic***	***Systematic***
Internal activity of quartz (assumed 0.02 Gy ka^{-1})	0.01 Gy.ka^{-1}*	0.03	***Systematic***	***Systematic***	***Systematic***
	Total:	3 (i.e. 6%)			

¤ Estimates only

* these two contributions are fixed, rather than relative to the dose rate.

for all OSL ages from the same laboratory (i.e. assuming a single set of calibration materials).

References

[1] H. N. Chandel, A. D. Patel, H. R. Vaghela and G. P. Ubale, »An effective and reusable sampling pipe for luminescence dating,« *Ancient TL,* vol. 24, nr. 1, pp. 21-22, 2006.

[2] H. M. Rajapara, V. Kumar, N. Chauhan, P. N. Gajjar and A. K. Singhvi, »Bleaching of blue light stimulated luminescence of quartz by moonlight,« *Journal of Earth System Science,* vol. 129, pp. 1-7, 2020.

[3] J. R. Prescott and J. T. Hutton, "Cosmic ray contributions to dose rates for luminescence and ESR dating: large depths and long-term time variations," *Radiation Measurements,* vol. 23, p. 497–500, 1994.

[4] M. Aitken, Thermoluminescence Dating, London: Academic Press, 1985, p. 153.

[5] N. Porat, G. Faerstein, A. Medialdea and A. Murray, »Re-examination of common extraction and purification methods of quartz and,« *Ancient TL,* vol. 33, pp. 22-30, 2015.

[6] G. Guérin, N. Mercier and G. Adamiec, »Dose-rate conversion factors: update.,« *Ancient TL,* vol. 29, nr. 1, pp. 5-8, 2011.

[7] L. Bøtter-Jensen, N. Agersnap Larsen, B. G. Markey and S. W. McKeever, »Al2O3:C as a sensitive OSL dosemeter for rapid assessment of environmental photon dose rates,« *Radiation Measurements,* vol. 27, nr. 2, pp. 295-298, 1997.

[8] D. Richter, H. Dombrowski, S. Neumaier, P. Guibert and A. C. Zink, "Environmental gamma dosimetry with OSL of α-Al2O3:C for in situ sediment measurements," *Radiation protection dosimetry,* vol. 141, p. 27–35, 2010.

[9] S. Kreutzer, L. Martin, G. Guérin, C. Tribolo, P. Selva and N. Mercier, "Environmental dose rate determination using a passive dosimeter: techniques and workflow for α-Al2O3:C chips," *Geochronometria,* vol. 45, p. 56–67, 2018.

[10] D. Miallier, G. Guérin, N. Mercier, T. Pilleyre and S. Sanzelle, "The Clermont radiometric reference rocks: a convenient tool for dosimetric purposes," *Ancient TL,* vol. 27, p. 37–42, 2009.

[11] L. J. Arnold, M. Duval, C. Falguères, J. J. Bahain and M. Demuro, "Portable gamma spectrometry with cerium-doped lanthanum bromide scintillators: Suitability assessments for luminescence and electron spin resonance dating applications," *Radiation Measurements,* vol. 47, p. 6–18, 2012.

[12] L. Løvborg and P. Kirkegaard, »Response of 3" x 3" NaI(Tl) detectors to terrestrial gamma radiation.,« *Nuclear Instrumensts and Methods ,* vol. 121, pp. 239-251, 1974.

[13] G. Guérin and N. Mercier, "Determining gamma dose rates by field gamma spectroscopy in sedimentary media: results of Monte Carlo simulations," *Radiation Measurements,* vol. 46, p. 190–195, 2011.

[14] C. W. Curry, R. H. Bennett, M. H. Hulbert, K. J. Curry and R. W. Faas, »Comparative Study of Sand Porosity and a Technique for Determining Porosity of Undisturbed Marine Sediment,« *Marine Georesources & Geotechnology,* vol. 22, p. 231–252, 10 2004.

[15] M. Nelson and T. Rittenour, »Using grain-size characteristics to model soil water content:

Application to dose-rate calculation for luminescence dating.,« *Radiation Measurements,* vol. 81, pp. 142-149, 2015.

[16] D. Zimmerman, »Thermoluminescent dating using fine grains from pottery.,« *Archaeometry,* vol. 13, pp. 29-52, 1971.

[17] M. Lawson, J. Daniels and E. Rhodes, »Assessing Optically Stimulated Luminescence (OSL) signal contamination within small aliquots and single grain measurements utilizing the composition test,« *Quaternary International,* vol. 362, pp. 34-41, 2015.

[18] O. Antohi-Trandafir, A. Timar-Gabor, A. Vulpoi, R. Bălc, J. Longman, D. Veres and S. Simon, »Luminescence properties of natural muscovite relevant to optical dating of contaminated quartz samples,« *Radiation Measurements,* vol. 109, pp. 1-7, 2018.

[19] M. Jain, A. S. Murray and L. Bøtter-Jensen, "Characterisation of blue-light stimulated luminescence components in different quartz samples," *implications for dose measurement Radiation Measurements,* vol. 37, p. 441–449, 2003.

[20] G. A. Duller, »Distinguishing quartz and feldspar in single grain luminescence measurements,« *Radiation Measurements,* vol. 37, pp. 161-165, 2003.

[21] D. Banerjee, A. S. Murray, L. Bøtter-Jensen and A. Lang, "Equivalent dose estimation from a single aliquot of polymineral fine-grains," *Radiation Measurements,* vol. 33, p. 73–93, 2001.

[22] P. M. Denby, L. Bøtter-Jensen, A. S. Murray and P. Moska, "Application of pulsed OSL to the separation of the luminescence components from a mixed quartz/feldspar sample," *Radiation Measurements,* vol. 41, p. 774–779, 2006.

[23] K. J. Thomsen, M. Jain, A. S. Murray, P. M. Denby, N. Roy and L. Bøtter-Jensen, "Minimizing feldspar OSL contamination in quartz UV-OSL using pulsed blue stimulation," *Radiation Measurements,* vol. 43, p. 752–757, 2008.

[24] M. Jain and A. Singhvi, »Limits to depletion of blue–green light stimulated luminescence in feldspars: implications for quartz dating.,« *Radiation Measurements,* vol. 33, p. 883–892, 2001.

[25] L. Clark-Balzan and J. Schwenninger, "First steps toward spatially resolved OSL dating with electron multiplying charge-coupled devices (EMCCDs): system design and image analysis," *Radiation Measurements,* vol. 47, p. 797–802, 2012.

[26] D. Richter, A. Richter and K. Dornich, "Lexsyg – a new instrument for luminescence research," *Geochronometria,* vol. 40, p. 220–228, 2013.

[27] K. J. Thomsen, M. Kook, A. S. Murray, M. Jain and T. Lapp, "Single-grain results from an EMCCD-based imaging system," *Radiation Measurements,* vol. 81, p. 185–191, 2015.

[28] L. Bøtter-Jensen and D. G.A.T, "A new system for measuring OSL from quartz samples," *Nucl. Tracks. Radiat. Meas,* vol. 20, p. 549–553, 1992.

[29] E. Bulur, L. Bøtter-Jensen and A. S. Murray, "Optically stimulated luminescence from quartz measured using the linear modulation technique," *Radiation Measurements,* vol. 32, p. 407–411, 2000.

[30] D. J. Huntley, M. A. Short and K. Dunphy, "Deep traps in quartz and their use for optical dating," *Canadian Journal of Physics,* vol. 74, p. 81–91, 1996.

[31] E. Bulur, "An alternative technique for optically stimulated luminescence (OSL) experiment," *Radiation Measurements,* vol. 26, p. 701–709, 1996.

[32] C. Ankjærgaard and M. Jain, "Optically stimulated phosphorescence in quartz over the millisecond to second time scale: insights into the role of shallow traps in delaying luminescent recombination," *Journal of Physics D: Applied Physics,* vol. 43, p. 255502, 2010.

[33] D. J. Huntley, D. I. Godfrey-Smith and M. L. W. Thewalt, "Optically dating of sediments," *Nature,* vol. 313, p. 105–107, 1985.

[34] G. A. T. Duller, L. Bøtter-Jensen, A. S. Murray and A. J. Truscott, "Single grain laser luminescence (SGLL) measurement using a novel automated reader," *Nuclear Instruments and Methods B,* vol. 155, p. 506–514, 1999.

[35] L. Bøtter-Jensen, K. J. Thomsen and M. Jain, "Review of optically stimulated luminescence (OSL) instrumental developments for retrospective dosimetry," *Radiation Measurements,* vol. 45, p. 253–257, 2010.

[36] L. Bøtter-Jensen, E. Bulur, G. A. T. Duler and A. S. Murray, "Advances in luminescence instrument systems," *Radiation Measurements,* vol. 32, p. 523–528, 2000.

[37] L. Bøtter-Jensen, G. A. T. Duller, A. S. Murray and D. Banerjee, "Blue light emitting diodes for optical stimulation of quartz in retrospective dosimetry and dating," *Radiation Protection Dosimetry,* vol. 84, p. 335–340, 1999.

[38] M. Jain, "Extending the dose range: Probing deep traps in quartz with 3.06 eV photons," *Radiation Measurements,* vol. 44, p. 445–452, 2009.

[39] G. A. T. Duller, L. Bøtter-Jensen and A. S. Murray, "Combining infrared- and green-laser stimulation sources in single-grain luminescence measurements of feldspar and quartz," *Radiation Measurements,* vol. 37, p. 543–550, 2003.

[40] V. Hansen, A. Murray, J. P. Buylaert, E. Y. Yeo and K. Thomsen, "A new irradiated quartz for beta source calibration," *Radiation Measurements,* vol. 81, pp. 123-127, 2015.

[41] B. Combès and A. Philippe, "Bayesian analysis of individual and systematic multiplicative errors for estimating ages with stratigraphic constraints in optically stimulated luminescence dating," *Quaternary Geochronology,* vol. 39, p. 24–34, 2017.

[42] A. Philippe, G. Guérin and S. Kreutzer, "BayLum-An R package for Bayesian analysis of OSL ages: An introduction," *Quaternary Geochronology,* vol. 49, p. 16–24, 2019.

[43] A. S. Murray, R. Marten, A. Johnston and P. Martin, »Analysis for naturally occurring radionuclides at environmental concentrations by gamma spectrometry.,« *Journal of Radioanalytical and Radiochemistry.,* vol. 115, pp. 263-288, 1987.

[44] P. Guibert and M. Schvoerer, »TL dating: Low background gamma spectrometry as a tool for the determination of the annual dose,« *International Journal of Radiation Applications and Instrumentation. Part D. Nuclear Tracks and Radiation Measurements,* pp. 231-238, 1991.

[45] Z. Jacobs and R. Roberts, »Single-grain chronologies for for the Still Bay and Howieson's Poort industries and the transition between them: Further analyses and statistical modelling,« *Journal of Human Evolution,* vol. 107, pp. 1-13, 2017.

[46] G. Guérin, N. Mercier, R. Nathan, G. Adamiec and Y. Lefrais, »On the use of the infinite matrix assumption and associated concepts: a critical review.,« *Radiation Measurements,* vol. 47, nr. 9, pp. 778-785, 2012.

[47] R. P. Nathan and B. Mauz, "On the dose-rate estimate of carbonate-rich sediments for trapped charge dating," *Radiation Measurements,* vol. 43, p. 14–25, 2008.

[48] G. Guérin and N. Mercier, »Preliminary insight into dose deposition processes in sedimentary media on a scale of single grains: Monte Carlo modelling of the effect of water on the gamma dose rate.,« *Radiation Measurements,,* vol. 47, nr. 7, pp. 541-547, 2012.

[49] A. S. Murray, J. P. Buylaert and C. Thiel, "A Luminescence Dating Intercomparison Based on a Danish Beach-ridge Sand," *Radiation Measurements,* vol. 81, pp. 32-38, 2015.

[50] I. I. I. BIPM, »Evaluation of measurement data-guide to the expression of uncertainty in measurement,« *JCGM 100: 2008 GUM 1995 with minor corrections. Joint Committe for Guides in Metrology,* pp. 1-132, 2008.

[51] R. Sohbati, A. S. Murray, L. Lindvold, J.-P. Buylaert and M. Jain, »Optimization of laboratory illumination in optical dating,« *Quaternary Geochronology,* vol. 39, pp. 105-111, 2017.

[52] C. Ankjærgaard and A. S. Murray, "Total beta and gamma dose rates based on beta counting in trapped charge dating," *Radiation Measurements,* vol. 42, p. 352–359, 2007.

[53] G. Guérin, E. Discamps, C. Lahaye, N. Mercier, P. Guibert, A. Turq, H. L. Dibble, S. P. McPherron, D. Sandgathe, P. Goldberg, M. Jain, K. J. Thomsen, M. Patou-Mathis, J.-C. Castel and M.-C. Soulier, »Multi-method (TL and OSL), multi-material (quartz and flint) dating of the Mousterian site of Roc de Marsal (Dordogne, France): correlating Neanderthal occupations with the climatic variability of MIS 5–3,« *Journal of Archaeological Science,* vol. 39, pp. 3071-3084, 2012.

[54] G. Guérin, M. Frouin, J. Tuquoi, K. J. Thomsen, P. Goldberg, V. Aldeias, C. Lahaye, N. Mercier, P. Guibert, M. Jain, D. Sandgathe, S. J. McPherron, A. Turq and H. L. Dibble, »The complementarity of luminescence dating methods illustrated on the Mousterian sequence of the Roc de Marsal: A series of reindeer-dominated, Quina Mousterian Layers dated to MIS 3,« *Quaternary International,* vol. 433, pp. 102-115, 2017.

[55] D. Rufer and F. Preusser, »Potential of autoradiography to detect spatially resolved radiation patterns in the context of trapped charge dating.,« *Geochronometria,* vol. 34, pp. 1-13, 2009.

[56] R. M. Mayya, P. Morthekai, M. K. Murari and A. K. Singhvi, "Towards quantifying beta microdosimetric effects in single grain quartz dose distribution," *Radiation Measurements,* vol. 41, p. 1032–1039, 2006.

[57] G. Guérin, M. Jain, K. J. Thomsen, A. S. Murray and N. Mercier, "Modelling dose rate to single grains of quartz in well-sorted sand samples: The dispersion arising from the presence of potassium feldspars and implications for single grain OSL dating," *Quaternary Geochronology,* vol. 27, pp. 52-65, 2015.

[58] R. K. Smedley, G. A. T. Duller, D. Rufer and J. Utley, "Empirical assessment of beta dose heterogeneity in sediments: implications for luminescence dating," *Quaternary Geochronology,* vol. 56, 2020.

[59] L. Martin, N. Mercier, S. Incerti, Y. Lefrais, C. Pecheyran, G. Guérin, M. Jarry, L. Bruxelles, F. Bon og C. Pallier, »Dosimetric study of sediments at the beta dose rate scale: Characterization and modelization with the DosiVox software.,« *Radiation Measurements,* vol. 81, pp. 134-141, 2015.

[60] D. J. Huntley, D. I. Godfrey-Smith and E. H. Haskell, "Light-induced emission spectra from some quartz and feldspars," *Nuclear Tracks and Radiation Measurements,* vol. 18, p. 127–131, 1991.

[61] L. Bøtter-Jensen, D. G.A.T. and P. N.R.J, "Excitation and emission spectrometry of stimulated luminescence from quartz and feldspars," *Radiation Measurements,* vol. 23, p. 613–616, 1994.

[62] A. S. Murray, L. Helsted, M. Autzen, M. Jain og J. Buylaert, »Measurement of natural radioactivity: Calibration and performance of a high-resolution gamma spectrometry facility,« *Radiation Measurements,* vol. 15, pp. 215-220, 2018.

[63] A. Murray og M. Aitken, »Analysis of low-level natural radioactivity in small mineral samples for use in thermoluminescence dating, using high-resolution gamma spectrometry,« *International Journal of Radiation Applications and Instrumentation. Part A. Applied Radiation and Isotopes,* vol. 39, pp. 145-158, 1988.

[64] M. Bu, A. S. Murray, M. Kook, L. M. Helsted, J.-P. Buylaert og K. J. Thomsen, »Characterisation of scintillator-based gamma spectrometers for,« *Radiation Measurements,* vol. 120, pp. 253-259, 2018.

[65] A. Cunningham, A. S. Murray, S. J. Armitage og M. Autzen, »High-precision natural dose rate estimates through beta counting,« *Radiation Measurements,* vol. 120, pp. 209-214, 2018.

[66] H. E. Jensen og J. R. Prescott, »The thick-source alpha particle countig technique: comparison with other techniques and solutions to the problem of overcounting,« *PACT (Rixensart, Belg.),* vol. 9, pp. 25-35, 1983.

[67] M. Sargent, H. Goenaga-Infante, K. Inagaki, L. Ma, J. Meija, A. Pramann, O. Rienitz, R. Sturgeon, J. Vogl, J. Wang og L. Yang, »The role of ICP-MS in inorganic chemical metrology,« *Meterologia,* vol. 56, p. 034005, 2019.

[68] R. Bailey, S. Stokes og H. Bray, »Inductively-Coupled Plasma Mass Spectrometry (ICP-MS) for dose rate determination: some guidelines for sample preparation and analysis.,« *Ancient TL,* vol. 21, pp. 11-15, 2003.

[69] S. Hossain, F. De Corte, D. Vandenberghe og P. Van den haute, »A comparison of methods for the annual radiation dose determination in the luminescence dating of loess sediment,« *Nuclear Instruments and Methods in Physics Research Section A: Accelerators, Spectrometers, Detectors and Associated Equipment,* vol. 490, nr. 3, pp. 598-613, 2002.

[70] S. M. Hossain, F. De Corte, D. Vandenberghe og P. Van den Haute, »The role of k0-NAA in the assessment of the annual radiation dose for use in TL/OSL dating of sediments,« *Journal of Radioanalytical and Nuclear Chemistry,* vol. 257, pp. 639-642, 2003.

[71] C. Burbidge og G. Duller, »Combined gamma and beta dosimetry, using Al2O3:C, for in situ measurements on a sequence of archaeological deposits.,« *Radiation Measurements,* vol. 37, pp. 285-291, 2003.

[72] G. Adamiec og M. J. Aitken, »Dose-Rate Conversion Factors: Update.,« *Ancient TL,* vol. 16, pp. 37-50, 1998.

[73] V. Mejdahl, »Thermoluminescence dating; beta-dose attenuation in quartz grains,« *Archaeometry,* vol. 21, pp. 61-72, 1979.

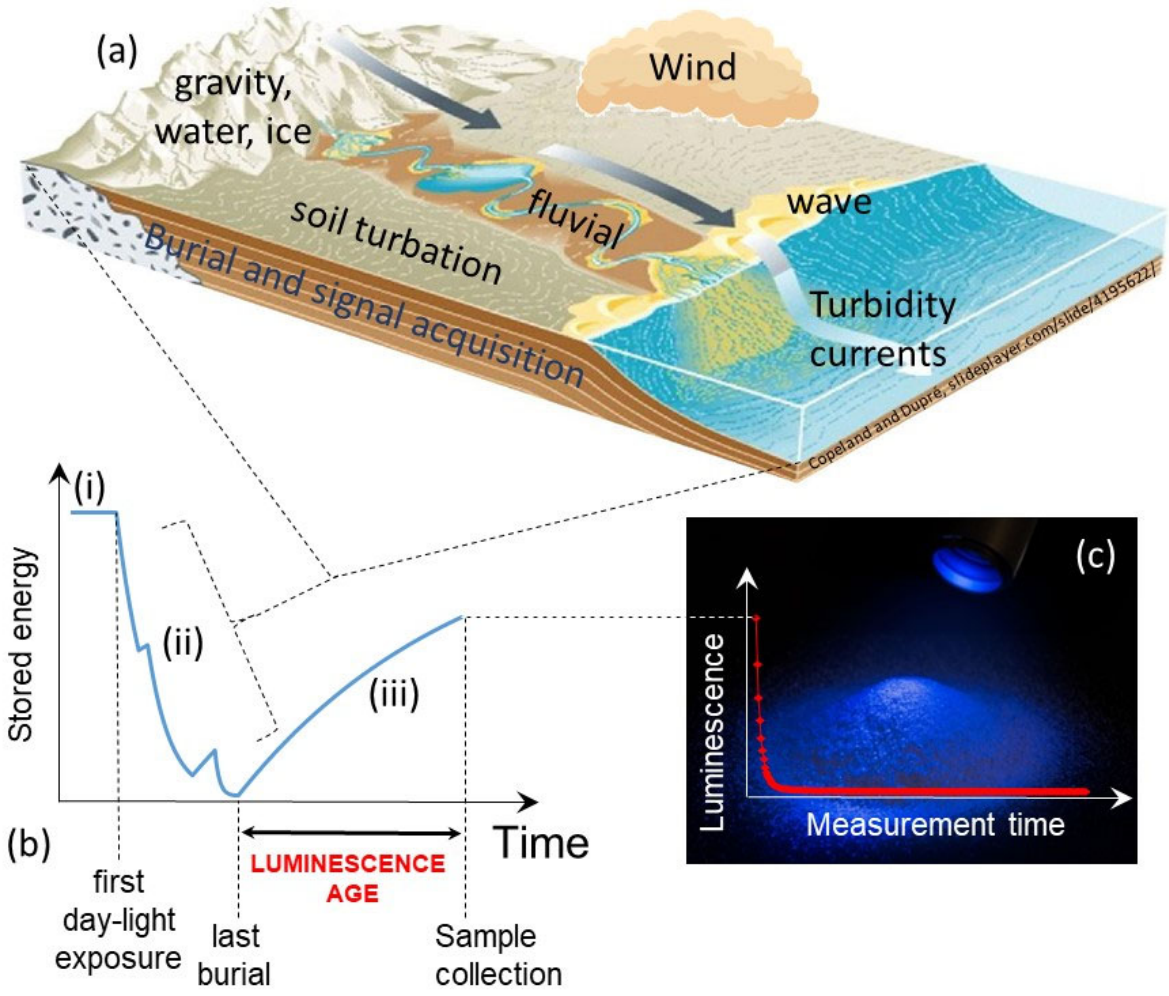

Figure 1: The erosion, transport and sedimentation cycle, and its relationship to the acquisition of a luminescence dating signal. (a) illustrates the various transport agencies that can lead to daylight exposure of mineral grains before final burial*. (b) any existing energy (i) stored in the quartz crystal structure is released by repeated daylight exposure (ii) during erosion and transport by wind, water, ice, gravity or turbation, interspersed with periods of burial. Sufficient net daylight exposure completely removes the previously stored energy. This energy builds up again (iii) during the most recent burial, until the quartz sand grains are sampled and taken to the laboratory. (c) Stimulating the sand grains with blue light releases the stored energy, some of which gives the luminescence signal. This signal decays rapidly with measurement time, as all the energy is released.
*gravity acts as an independent transport agency only on high gradients.

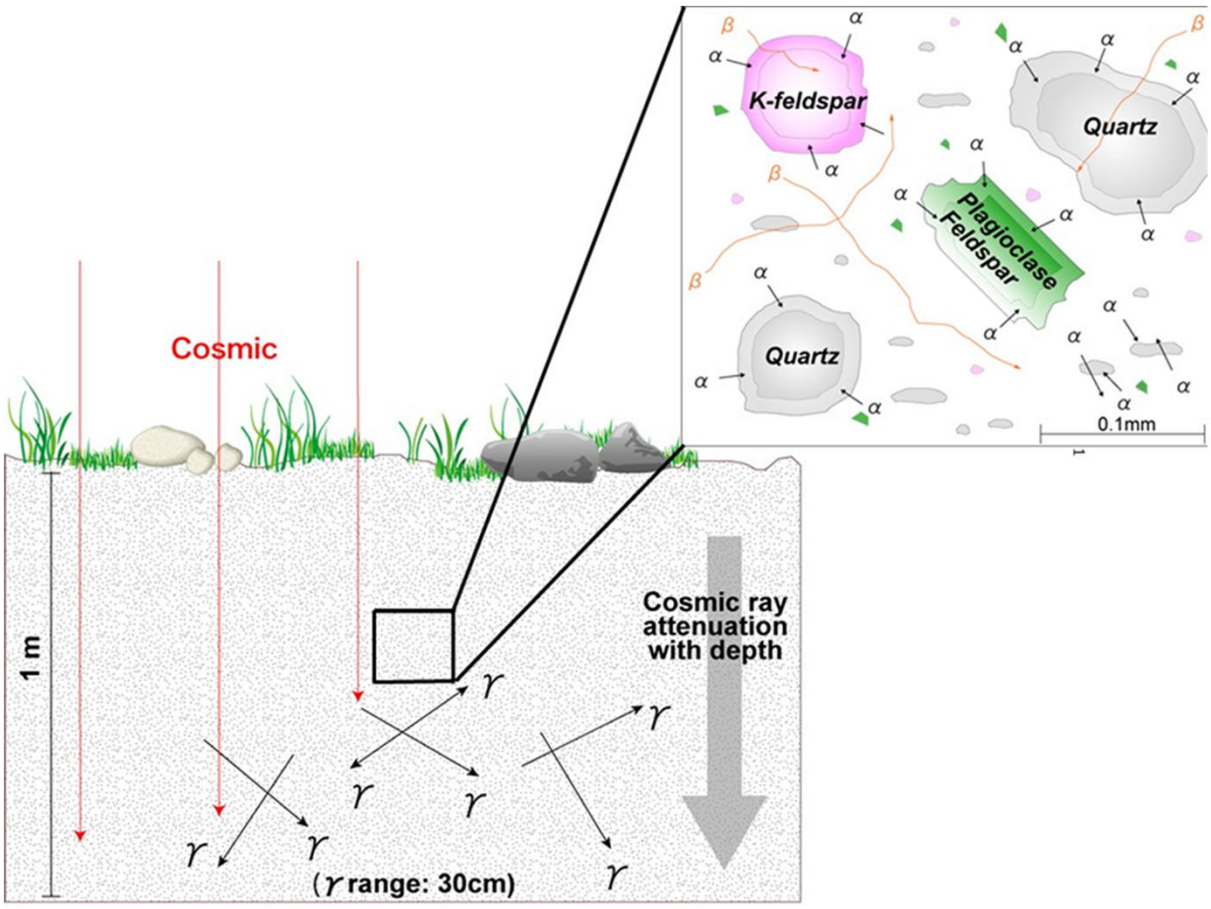

Figure 2. Dose rate components in luminescence dating. Decay of naturally occurring radionuclides (^{238}U, ^{232}Th and ^{40}K) produces ionising radiation (a-particles, b-particles, g-photons), each with a specific range in sediment. A small portion of the dose rate comes from cosmic rays hitting the Earth's surface. Figure redrawn from [206].

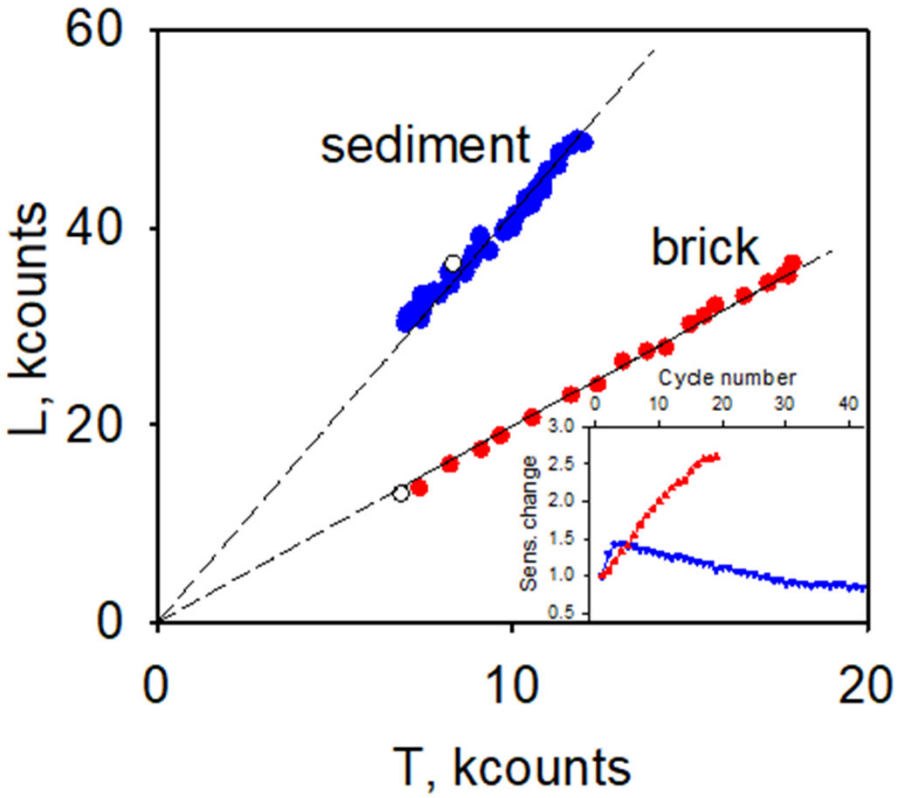

Figure 3. The proportional relationship between L_i and T_i for a large aliquot (containing hundreds of grains) of 180-250 µm quartz extracted from a fired brick (filled red circles, 19 cycles) and a quartz aliquot from a desert sediment (filled blue circles, 42 cycles). The sediment sample comes from the Kalahari Desert in Namibia (lab code: 175405) and the brick from a monastery floor in Sweden (lab code: 173701). The natural signals (L_0) are shown as open circles. Both datasets are consistent with straight lines (dashed) going through the origin, indicating that the ratio L_i/T_i is constant for each sample. The inset shows the sensitivity change as measured by T_i (normalized to first test dose measurement) as a function of measurement cycle. Note that heated quartz typically displays a greater sensitivity change during SAR measurements compared to quartz extracted from sediment. Sediment (175405): D_i=44.4 Gy, D_T=5.9 Gy. Fired brick (173701): D_i=3.6 Gy, D_T= 1.0 Gy.

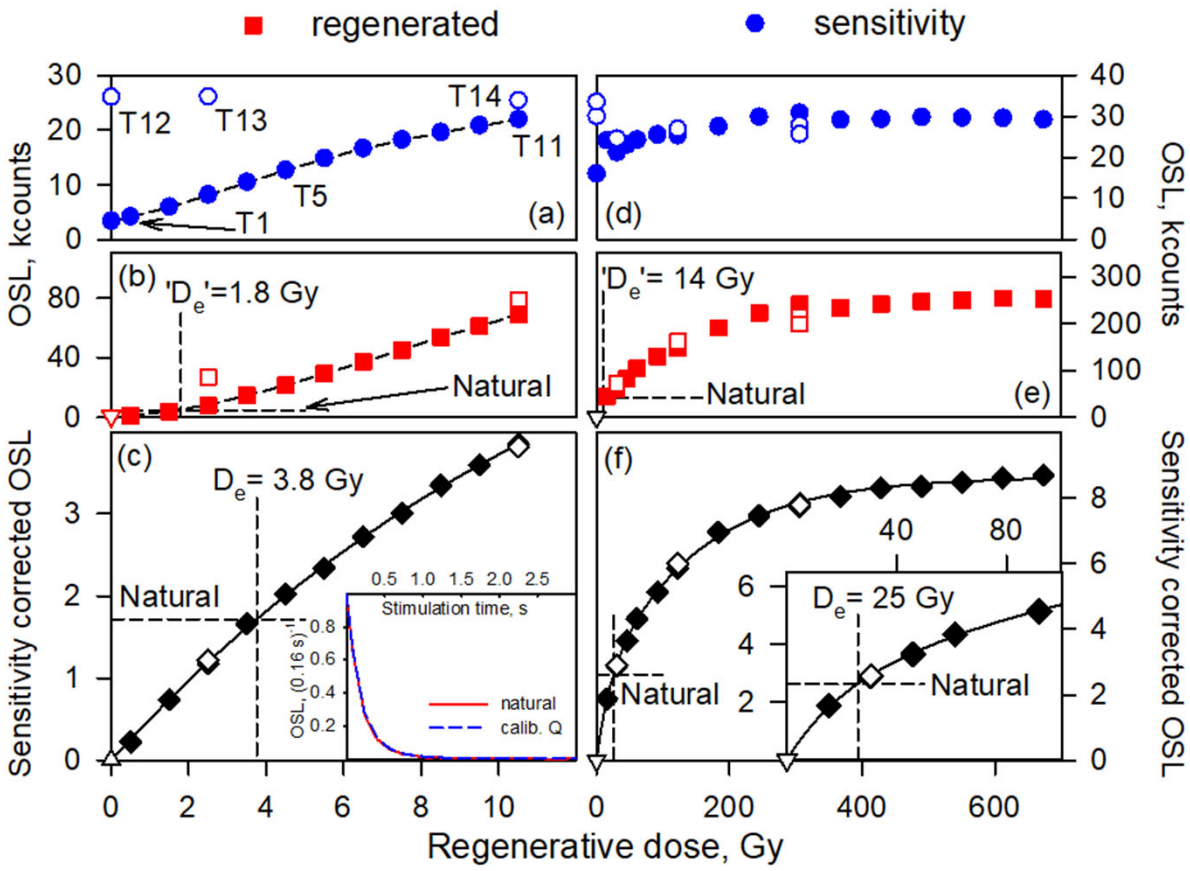

Figure 4. (a) T_i and (b) L_i plotted against dose for an aliquot of heated brick quartz; some T_i are labelled to indicate measurement order. (c) Sensitivity corrected (L_i/T_i) growth curve obtained by dividing data from (b) by data from (a); inset, stimulation curves for natural signal and calibration quartz [36]. (d) - (f) same as (a)-(c) but for quartz extracted from sediment. Open triangles show the response to D=0 Gy. Other open symbols indicate repeated dose measurements. Note that without sensitivity correction (b, e) the repeated values of L are inconsistent with earlier measurements at the same dose; correcting for sensitivity change by diving by T_i corrects this (c, f). The interpolated doses ('D_e' in b,e and D_e in c,f) and growth curve shapes are also significantly different for the uncorrected and sensitivity corrected data. Samples are the same as used in Figure 3.

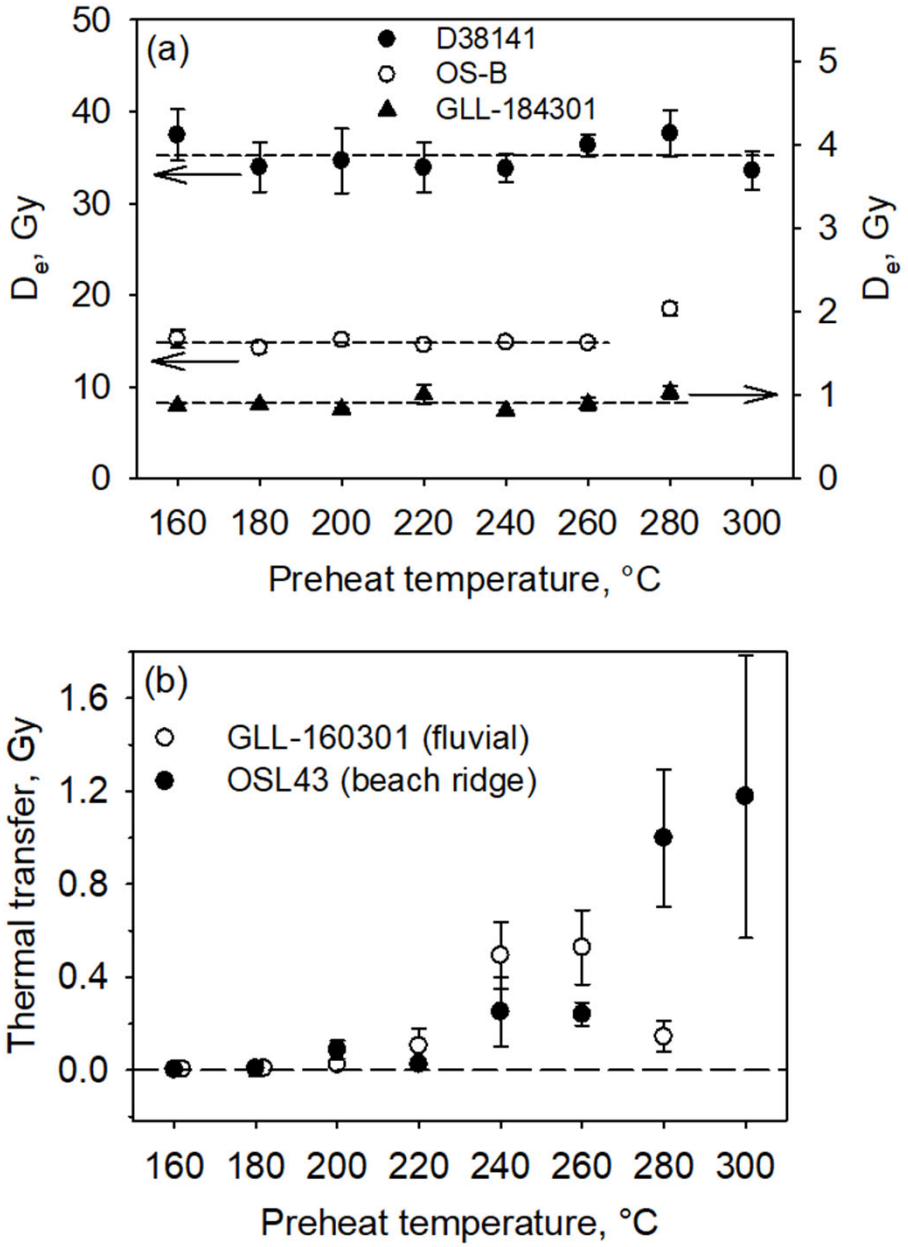

Figure 5. (a) Preheat plateaus for sand-sized quartz extracted from loess (D38141 [60], coversand (OS-B; [61]) and heated sediment from a charcoal kiln (GLL-184301; [259]). For all three samples the D_e is independent of preheat temperature over a wide temperature interval (dashed line). (b) Thermal transfer plateaus for sand-sized quartz extracted from a fluvial sand (GLL-160301; [260]) and a beach ridge (OSL43; [261]). Quartz aliquots were bleached at room temperature twice using blue light stimulation to remove the natural OSL signal before measurement of the thermally transferred dose. The effect of thermal transfer becomes visible for preheats ≥200°C.

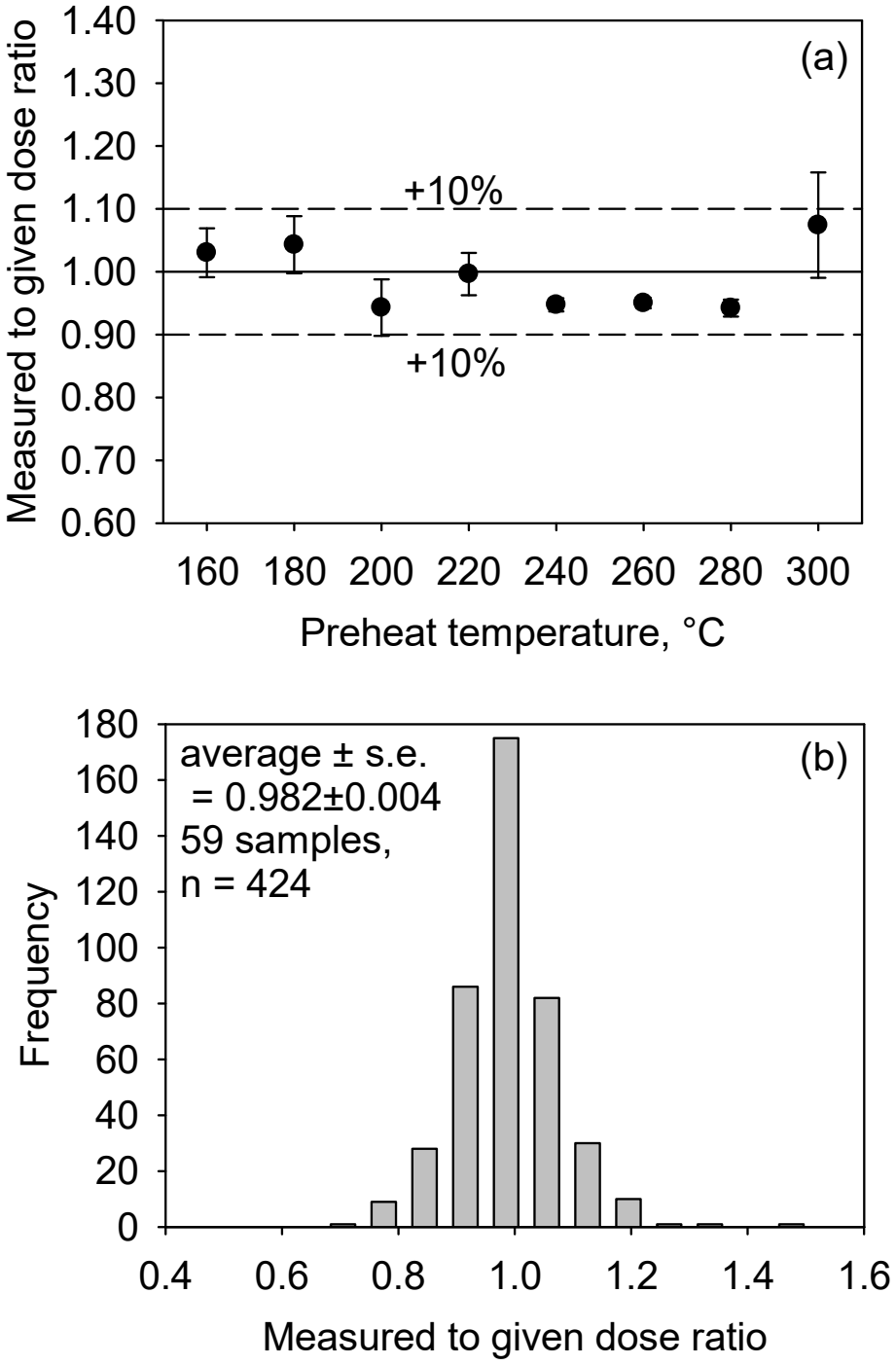

Figure 6. (a) Dose recovery plateau for sand-sized quartz extracted from Chinese loess. The measured to given dose ratio is insensitive to preheat temperature over a wide temperature range. (b) Histogram of dose recovery results measured with a preheat temperature of 260°C. Adapted from [64].

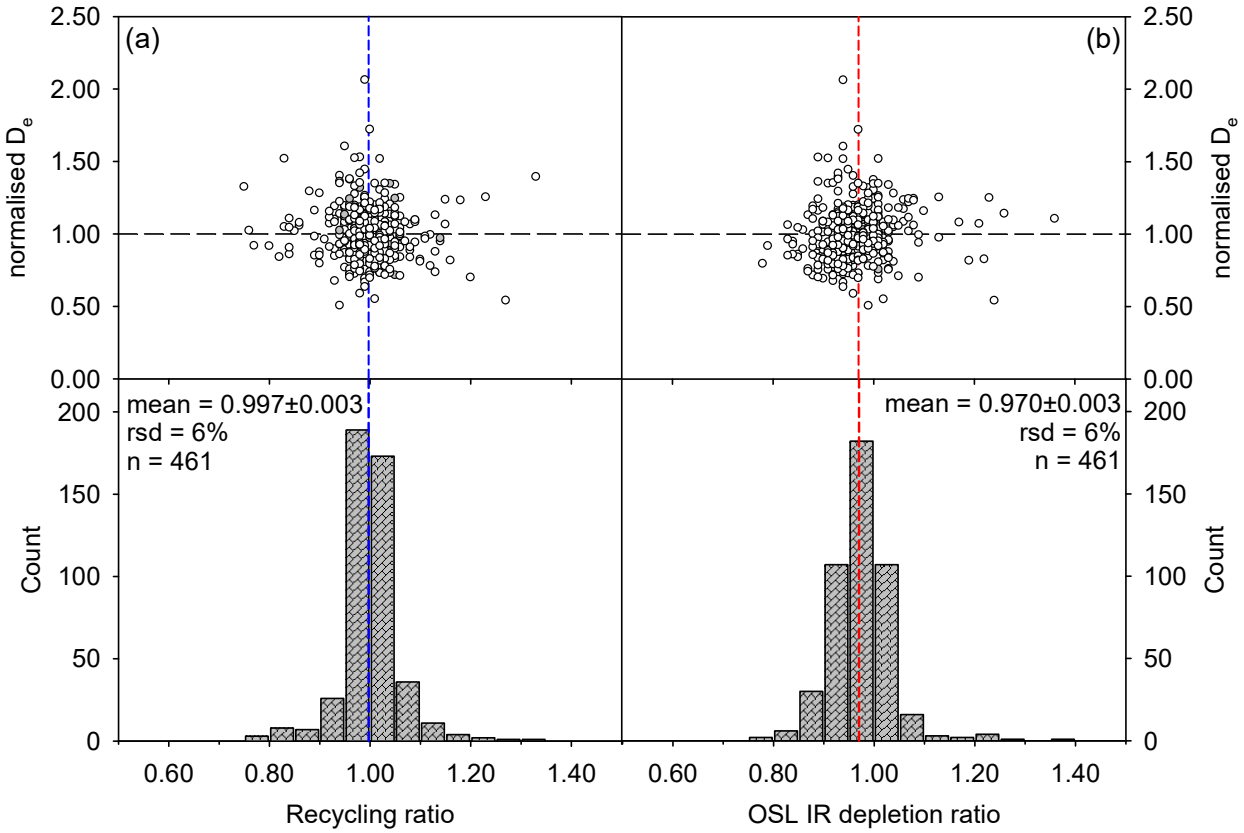

Figure 7. Relationship between large aliquot (containing many hundreds of grains) D_e and recycling ratio (a) or OSL IR depletion ratio (b) for 90-180 µm quartz extracted from Chinese loess. Upper figures show the individual aliquot D_e values (normalized to the average D_e of each sample) as a function of recycling ratio and OSL IR depletion ratio. Lower figures show the recycling and OSL IR depletion ratios as histograms with mean ratios plotted as blue and red dashed lines, respectively. From the upper figures it can be seen that there is no relationship between the measured D_e and the recycling or OSL IR depletion ratio; rejection of aliquots based on recycling or OSL IR depletion ratios does not improve these sample D_e. Figure adapted from [60].

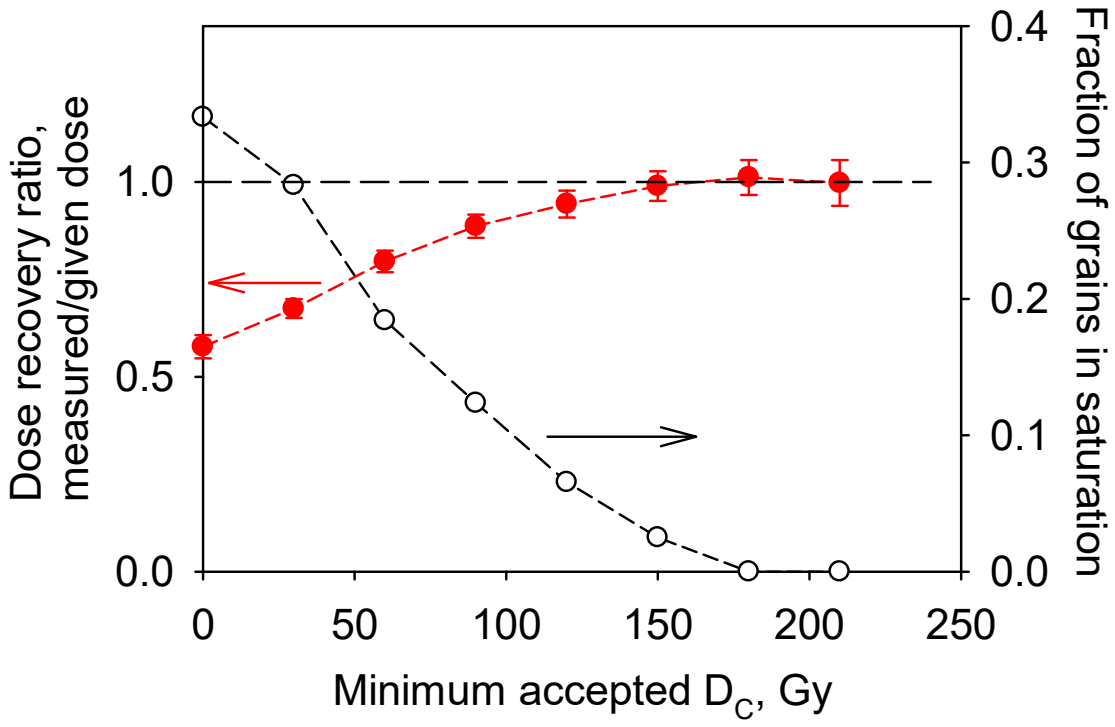

Figure 8. Effect of D_C filtering on grains with different D_C [237]. The dose recovery data (red data, given dose 170 Gy) shows the effect on the dose recovery ratio of only accepting results from aliquots with increasingly larger D_c values. These data suggest that only those grains with $D_C > 125$ Gy give accurate results (red data). Even with this minimum D_C, ~3% of the accepted grains still give doses in measured doses in saturation (black data).

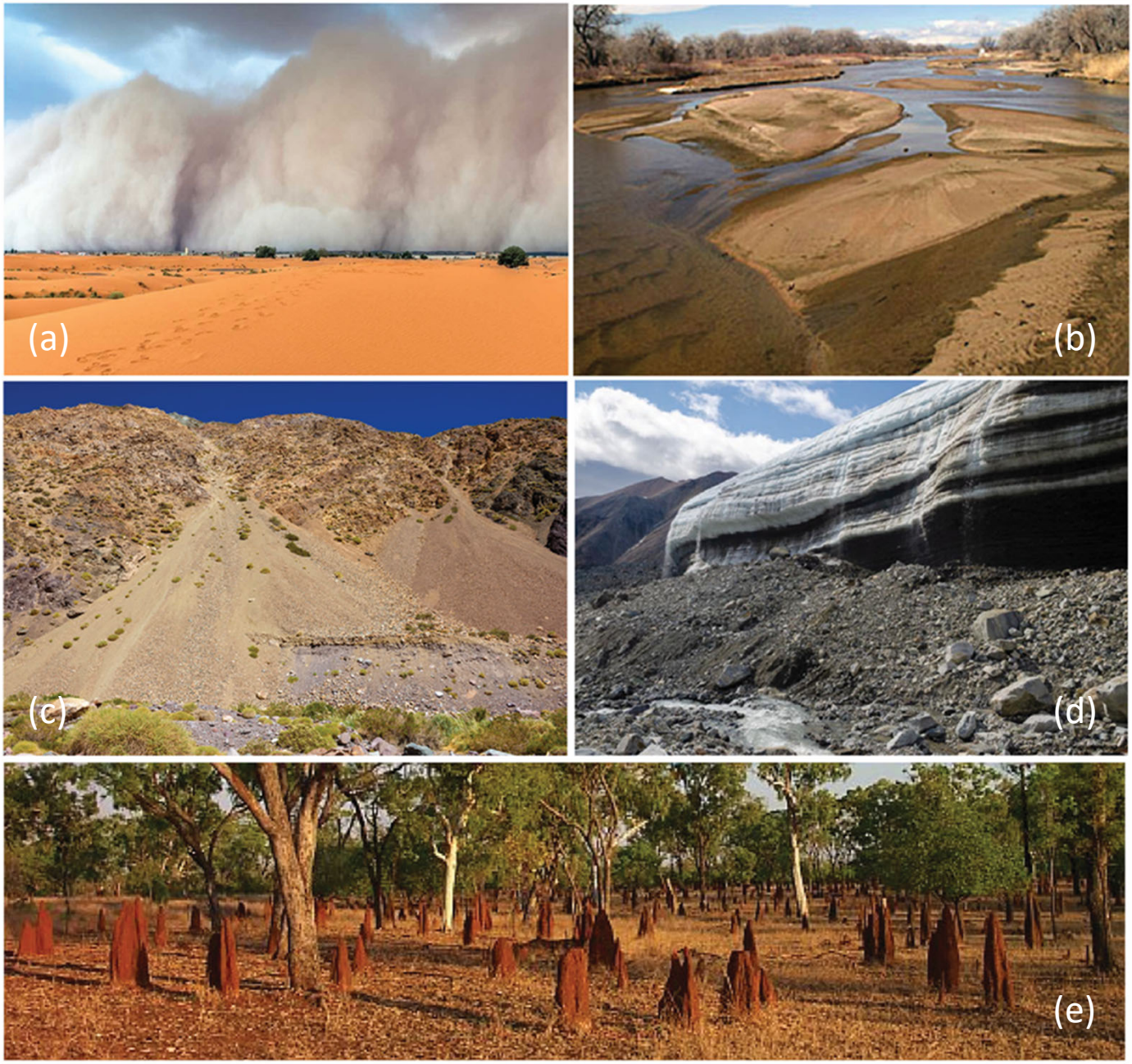

Figure 9. Opportunities for bleaching of the OSL signal in different environments. (a) aeolian transport during dust storms (Pavliha-istockphoto.com). (b) fluvial transport (Marek Uliasz - race.fit2paddle.com). (c) gravity-driven debris fans (unknown) (d) sediment transported by ice (Michael Hambrey - Glaciers online)(e) bioturbation - termite mounds (ourterritory.com).

Murray et al. Fig. 10a

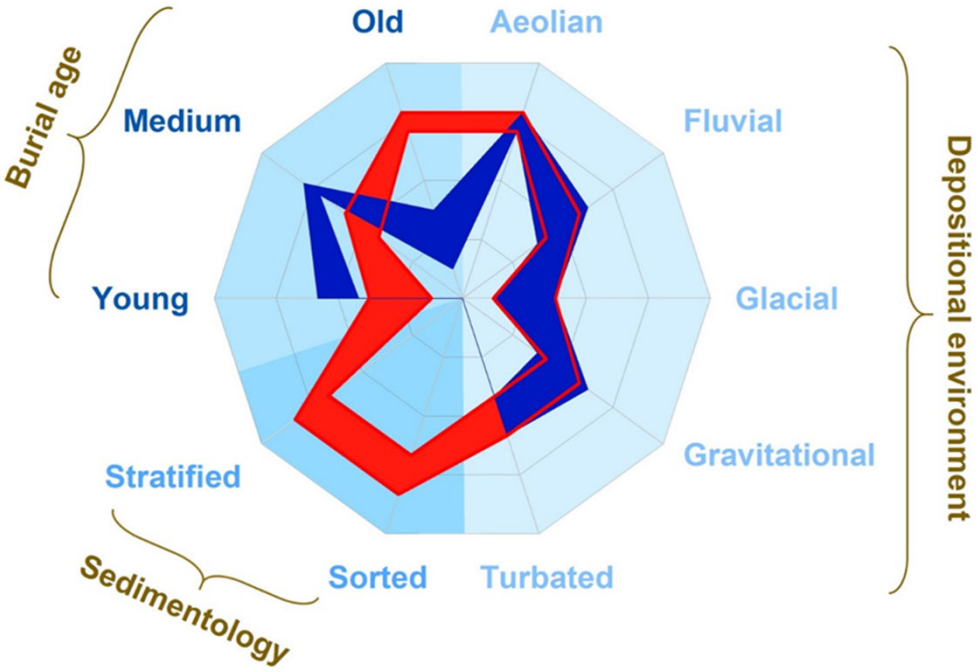

Figure 10a. The likely complexities in D_e determination arising from luminescence characteristics (dark blue band) and bleaching (red band), expressed qualitatively in terms of field observables and expected age (see Section 3 for details). These observables and estimates are shown on the 10 radial axes, grouped according to Depositional environment and implied transport mechanism (very light blue), Sedimentology (light blue) and the expected Burial age of the samples (median blue). "Young" refers to quartz grains with expected D_e values of less than ~10 Gy, "Old" to quartz grains with D_e values of larger than ~130 Gy. Each axis is scaled from most complex (centre of the figure) to least complex (outer edge of figure). The likely variability of each feature is shown by the band width on a particular axis. There is no reason to expect a correlation between luminescence characteristics and sorting/stratification, and so there is no dark blue band in that portion of the figure.

For example, the figure shows that aeolian sediments are likely to show low complexity, because they tend to be well bleached and have good luminescence characteristics, both with low variability. In contrast, glacial sediments are likely to show high complexity, because they tend to be poorly bleached and have poor luminescence characteristics although the variability in this conclusion is considerable. Bleaching becomes progressively less important (and less variable) as the Burial age increases, and so the complexity arising from this parameter decreases with age, whereas complexity from luminescence characteristics is at a maximum for oldest sediments (mainly because of saturation effects), and a minimum for medium age material, where signals are strong, and the saturation effects are small.

Murray et al. Fig. 10b

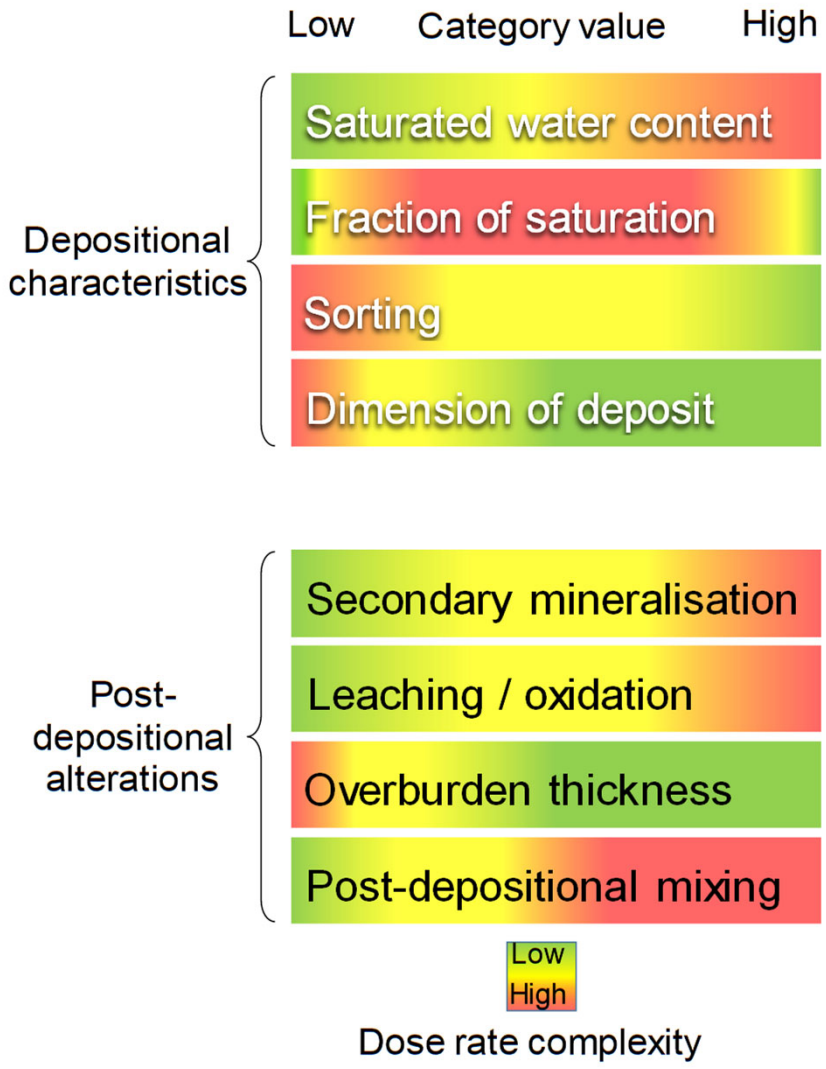

Figure 10b. Bar chart showing the relative influences of different sedimentary characteristics on dose rate complexity. Each bar depicts an observable sedimentary characteristic (y-axis) that can be evaluated at the time of OSL sample collection or during sample preparation (white labels – present at the time of deposition; black labels – post-depositional alteration). Each bar is gradationally coloured according to the degree of beta, gamma and cosmic dose rate complexity (in both space and time) expected for a given category value (x-axis).

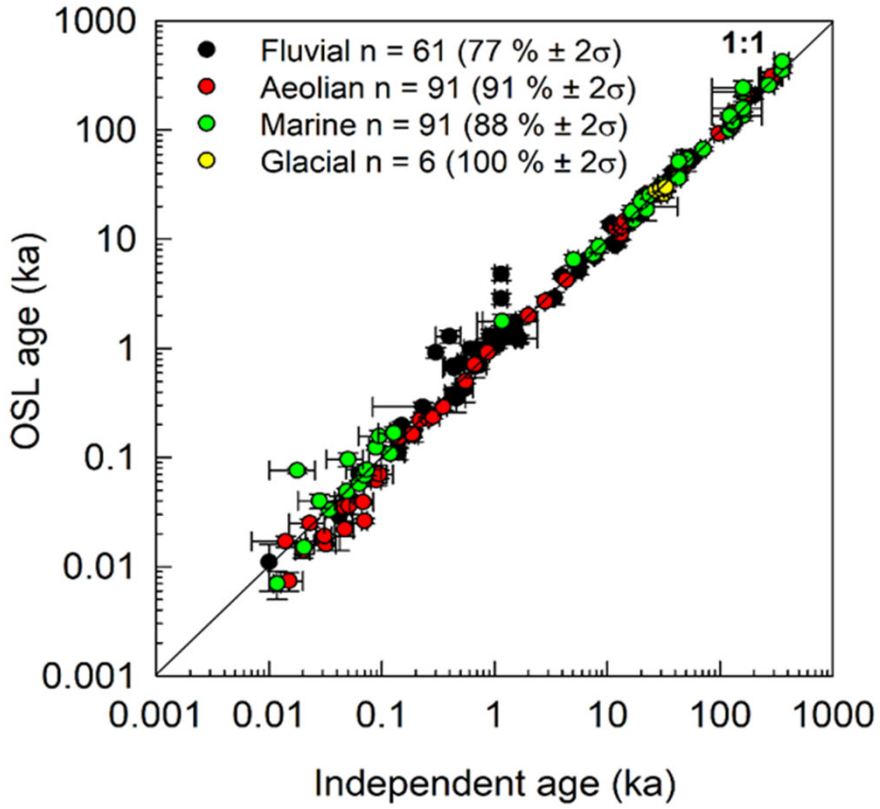

Figure 11. [77], [262], [80]: Comparison of quartz OSL ages with independent age control (n = number of samples, followed by the % of samples within ± 2 σ of the line of unit slope).

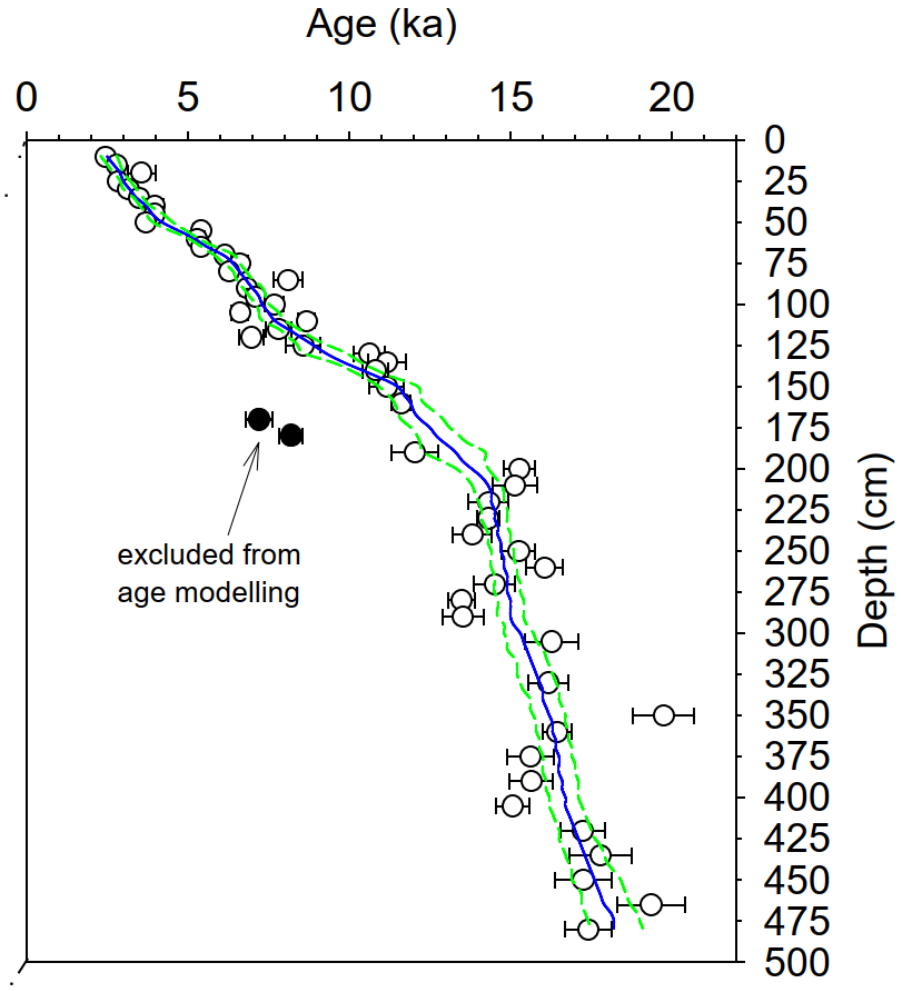

Figure 12. Large aliquot 63-90 um quartz OSL ages plotted as a function of depth for a section of Chinese loess encompassing last glacial loess and Holocene soil. Uncertainties are random only. A Bayesian model (with 1σ error band) is also shown illustrating how higher precision can be achieved. Ages excluded from modelling are from samples deliberately sampled in crotovina. Figure modified from SI in [60].